BULGARIAN
ACADEMY
OF SCIENCE
1869

Bulgarian Academy of Sciences

INSTITUTE OF ASTRONOMY
NATIONAL ASTRONOMICAL OBSERVATORY

Institute of Astronomy and National Astronomical Observatory

# Solar Transients From The Sun to Earth Coronal Bright Fronts, Radio Bursts, and Energetic Protons

Autoreferat of PhD dissertation
4.1 Physics, Specialization: Heliophysics

**Mohamed ElSayed Nedal AbulAinain Mohamed**

Supervisor: Assoc. Prof. Kamen Asenov Kozarev
Sofia March 25, 2024

# Acknowledgments

Pursuing a doctoral degree during a global pandemic has been a challenging yet incredible and rewarding journey of personal growth and intellectual stimulation. This dissertation would not have been possible without the guidance and support of many incredible people around me.

First and foremost, I am deeply grateful to my advisor, Dr. Kamen Kozarev. Thank you for giving me the opportunity to work on such an interesting and exciting project (SPREADFAST: Solar Particle Radiation Environment Analysis and Forecasting—Acceleration and Scattering Transport). Thank you for granting me the flexibility to work and the freedom to explore and experiment with new ideas. Your insightful feedback, unwavering encouragement, and dedication to my success have been invaluable throughout this process. I am incredibly grateful for your patience during moments of doubt and your enthusiasm that reignited my passion when I needed it most, as well as your ability to help me refine my thoughts and ideas. I am truly fortunate to have had you as my advisor.

I extend my heartfelt gratitude to my colleagues in the Sun and Solar System Department at the Institute of Astronomy and National Astronomical Observatory, Bulgarian Academy of Sciences: Dr. Rositsa Miteva, Dr. Oleg Stepanyuk, and Dr. Momchil Dechev. Thank you for the stimulating discussions, the collaborative spirit, and for generously sharing your expertise. Your valuable advice, feedback, and support have greatly enriched my experience. I am also grateful to Nestor Arsenov and Yordan Darakchiev for the insightful discussions on deep learning models, which have been valuable in shaping my understanding.

A special thank you goes to Dr. Pietro Zucca and Dr. Peijin Zhang for introducing me to the fascinating world of radio observations from the Low-Frequency Array (LOFAR) and guiding me through the intricacies of working with the data and relevant software. Thank you for the cherished moments we shared during my visits to the Netherlands and other places; those experiences have left an indelible imprint.

Furthermore, I am grateful for the financial support provided by the MOSAIICS project (Modeling and Observational Integrated Investigations of Coronal Solar Eruptions) and the STELLAR project (Scientific and Technological Excellence by Leveraging LOFAR Advancements in Radio Astronomy). This funding has been a tremendous blessing, allowing me to focus wholeheartedly on my research without financial constraints, and has significantly contributed to the successful completion of this dissertation.

My deepest appreciation goes to my family. Thank you for your unwavering love, belief in me, and constant prayers and encouragement throughout this long journey. You have been my source of strength and motivation. To my dear Bulgarian, Egyptian, and Arab friends, thank you for the countless moments of laughter, the much-needed distractions, and for reminding me of the vibrant world beyond academia. Your support and companionship, especially during my initial period in Bulgaria, have rendered this experience all the more enjoyable.

Finally, I would like to acknowledge and express my heartfelt gratitude to all those who have directly or indirectly contributed to this work. The collective efforts of all contributors, no matter how big or small, have played a crucial role in bringing me to this point and the successful completion of this dissertation.

Those four years were the most beautiful time of my life and I will always cherish them. Thank you all from the bottom of my heart.

# Solar Transients From The Sun to Earth
## Coronal Bright Fronts, Radio Bursts, and Energetic Protons

**Mohamed ElSayed Nedal AbulAinain Mohamed**

Institute of Astronomy and National Astronomical Observatory
Bulgarian Academy of Sciences
Sun and Solar System Department

Supervisor: Assoc. Prof. Kamen A. Kozarev

# Abstract

This interdisciplinary thesis advances our understanding of solar transients by investigating the early dynamics of Coronal Bright Fronts (CBFs), diagnosing solar type III radio bursts, and forecasting Solar Energetic Proton (SEP) integral fluxes. Integrating these studies, we reveal the relationships among these phenomena and their implications for space weather forecasting and hazard mitigation. Our analysis of 26 CBFs, using the Solar Particle Radiation Environment Analysis and Forecasting–Acceleration and Scattering Transport (SPREAdFAST) framework and data from the Atmospheric Imaging Assembly (AIA) and the Large Angle and Spectrometric Coronagraph (LASCO) instruments, unveils temporal evolution, plasma properties, and compressional characteristics. The second study, employing the Low-Frequency Array (LOFAR) and Parker Solar Probe (PSP), characterizes 9 type III radio bursts in the combined dynamic spectrum and 16 in the LOFAR spectrum alone. Potential Field Source Surface (PFSS) and magnetohydrodynamic (MHD) models offer insights into plasma conditions and magnetic fields, advancing our understanding of type III radio bursts triggered by accelerated electrons associated with CBFs and solar flares. Addressing forecasting, a bi-directional Long short-term memory (BiLSTM) neural network using OMNIWeb data from 1976 to 2019 predicts SEP fluxes, emphasizing the hazardous influence of energetic particles on Earth and technology. This work provides a unified framework, highlighting the interconnected nature of solar transients and their collective impact on space weather.

# Contents

# List of Tables

# List of Figures

# Definitions and Acronyms

Here, I provide definitions for key domain-specific terms and measurement concepts used consistently throughout the thesis. Additionally, relevant terminology will be introduced within the corresponding chapters. Below is a compilation of the essential technical terms and acronyms featured in this work:

CME – Coronal Mass Ejection
ICME – Interplanetary Coronal Mass Ejection
SF – Solar Flare
CIR – Corotating Interaction Region
IMF – Interplanetary Magnetic Field
GS – Geomagnetic Storm
Dst – Disturbance storm time
AU – Astronomical Unit
MPA – Measurement Position Angle
SEPs – Solar Energetic Particles/Protons
ESP – Energetic Storm Particle
EUV – Extreme Ultra-Violet
CBF – Coronal Bright Front
SRB – Solar Radio Burst
DH – Decameter-Hectometric
SOHO – Solar and Heliospheric Observatory
LASCO – Large Angle and Spectrometric Coronagraph
ERNE – Energetic and Relativistic Nuclei and Electron
EIT – Extreme ultraviolet Imaging Telescope
TRACE – Transition Region and Coronal Explorer
ESA – European Space Agency
MHD – Magneto-Hydro-Dynamic
MAS – Magnetohydrodynamic Algorithm outside a Sphere
PSI – Predictive Science Inc.
PFSS – Potential Field Source Surface
AIA – Atmospheric Imaging Assembly
SDO – Solar Dynamic Observatory
EUVI – Extreme Ultraviolet Imager
STEREO – Solar Terrestrial Relations Observatory
LOFAR – Low-Frequency Array
PSP – Parker Solar Probe
GOES – Geostationary Operational Environmental Satellite
SN – Sunspot Number
SC – Solar Cycle
sfu – solar flux units
pfu – proton flux units
L1 – First Lagrange point
SPDF – Space Physics Data Facility
SILSO – Sunspot Index and Long-term Solar Observations
NOAA – National Oceanic and Atmospheric Administration
NASA – National Aeronautics and Space Administration
GSFC – Goddard Space Flight Center

SPREAdFAST – Solar Particle Radiation Environment Analysis and Forecasting–Acceleration and Scattering Transport
CASHeW – Coronal Analysis of SHocks and Waves
DSA – Diffusive Shock Acceleration
SDA – Shock Drift Acceleration
S2M – Synthetic Shock Model
EPREM – Energetic Particle Radiation Environment Module
DEM – Differential Emission Measure
FLCT – Fourier Local Correlation Tracking
CM – Centers of Mass
GC – Geometric Center
GCS – Graduated Cylindrical Shell
NN – Neural Network
ML – Machine Learning
DL – Deep Learning
CNN – Convolutional Neural Network
GAN – Generative Adversarial Networks
RNN – Recurrent Neural Network
BiLSTM – Bi-directional Long short-term Memory
Adam – Adaptive moment estimation
MIMO – Multi-Input Multiple Output
MSE – Mean Squared Error
MAE – Mean Absolute Error
MSLE – Mean Squared Logarithmic Error
TP – True Positive
TN – True Negative
FP – False Positive
FN – False Negative
POD – Probability of Detection
POFD – Probability of False Detection
FAR – False Alarm Rate
CSI – Critical Success Index
TSS – True Skill Statistic
HSS – Heidke Skill Score

# Chapter 1

# Introduction

## 1.1 Background and Motivation

The Sun, a typical star at the center of our solar system, displays various forms of activity across different scales. This includes energetic eruptive events like solar flares and Coronal Mass Ejections (CMEs), driven by the release of magnetic energy stored in complex magnetic structures in the solar atmosphere (Moore et al. 2001; Priest & Forbes 2007; Zhang et al. 2012; Amari et al. 2014). These events release electromagnetic radiation and energetic particles (Schwenn 2006; Pulkkinen 2007), affecting *space weather* (Schrijver & Siscoe 2010a; Eastwood et al. 2017) (Fig. 1.1). They cause disturbances in near-Earth and planetary environments, impacting communication, satellites, power grids, aviation, and space missions (Lanzerotti 2001; Schwenn 2006; Pulkkinen 2007; Lilensten et al. 2014).

Understanding these solar phenomena and their impacts is crucial globally. Research aims to uncover the underlying physical processes through observations, theory, and modeling, while also developing predictive capabilities for space weather. This field, known as *heliophysics* (Schrijver & Siscoe 2010b), encompasses studying solar, heliospheric, and geospace plasma processes, their impacts on technology and space assets, and strategies for prevention and mitigation (Schrijver et al. 2015; Schrijver 2015). Initiatives like NASA's Living With a Star program and the National Science Foundation's Space Weather activities drive scientific understanding and predictive capabilities (Brewer et al. 2002).

This thesis focuses on investigating key aspects of solar eruptive activity and its impacts within the realm of heliophysics and space weather. Specific topics include studying the propagation of coronal disturbances triggered by CMEs and flares, the characteristics of solar type III radio bursts, and forecasting Solar Energetic Particle (SEP) events, which pose significant space radiation hazards.

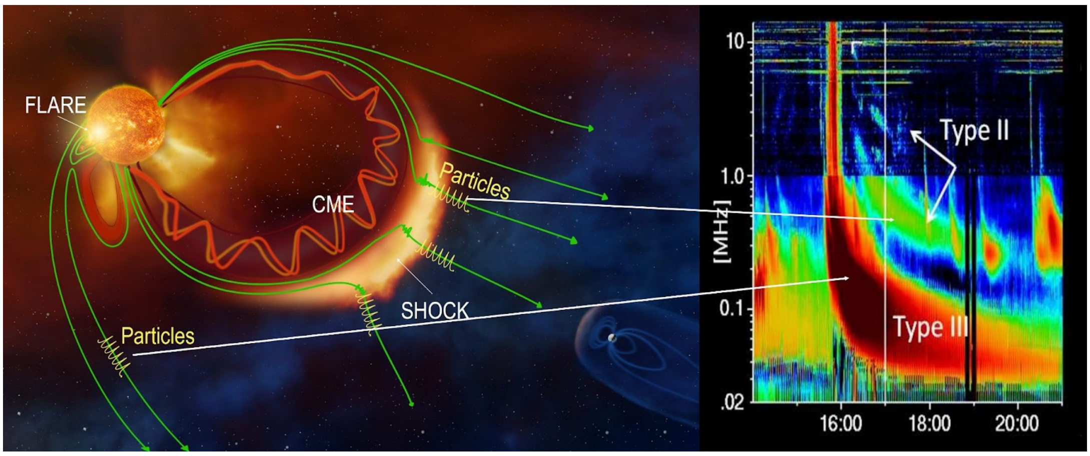


Figure 1.1: On the left side, a graphical illustration, adapted from ESA/A. Baker, CC BY-SA 3.0 IGO, depicts different eruptive phenomena, while on the right side, there is a representation of spacecraft data (specifically Wind/Waves data from Gopalswamy et al. (2019)) showcasing a radio dynamic spectra, emphasizing distinct spectral categories of SRBs on November 9, 2000. Type-II bursts are correlated with the shock front of a CME, whereas Type-IIIs are connected with the acceleration of SEPs. Image courtesy[1]

The thesis investigates the origins and propagation mechanisms of transient phenomena resulting from solar eruptions. It employs observational data, analytical theory, modeling, and data science techniques. Despite decades of study using space mission observations, gaps persist in understanding their underlying physics and space weather impacts. The thesis aims to provide new insights within the framework of heliophysics research. Each research topic is explored in dedicated chapters, discussing background, significance, observational challenges, knowledge gaps, and relevant literature. More details can be found in the thesis.

### 1.1.1 Coronal Waves

Coronal waves, also known as Coronal Bright Fronts (CBFs) or EUV waves, are large-scale arc-shaped disturbances observed propagating across the solar corona following the eruption of CMEs and solar flares (Thompson et al. 1998; Nindos et al. 2008; Vršnak & Cliver 2008; Magdalenić et al. 2010a; Veronig et al. 2010; Warmuth 2015). These waves, visible in EUV, white-light coronal emission, and radio wavelengths, can span distances of up to several hundred Mm and travel at speeds ranging between 100-1000 $km\,s^{-1}$, faster than the local characteristic speed in the corona, eventually transforming into shock waves (Pick et al. 2006; Thompson & Myers 2009; Nitta et al. 2013; Liu & Ofman 2014). They consist of piled-up plasma with higher density, making them appear brighter in white-light images.

Discovered through observations obtained with the Extreme ultraviolet Imaging Telescope (EIT) instrument on the Solar and Heliospheric Observatory (SOHO) that was launched in 1995, coronal waves appear as bright propagating fronts in 19.5 nm wavelength imaging of Fe XII emission lines formed at approximately 1.5 MK plasma (Thompson et al. 1998). Subsequent studies using SOHO/EIT and the Transition Region and Coronal Explorer (TRACE) found correlations between coronal waves and CMEs, suggesting they are fast-mode magnetohydrodynamic (MHD) waves driven by CME lateral expansions (Biesecker et al. 2002).

Since 2010, the initiation and evolution of coronal waves have been observed with unprecedented resolution by the Atmospheric Imaging Assembly (AIA) on the Solar Dynamics Observatory (SDO), using multiple EUV passbands sensitive to a wide temperature range (Lemen et al. 2012; Nitta et al. 2013). Observing and studying coronal shock waves remotely is typically done through EUV observations using space-based instruments like AIA onboard the SDO spacecraft. Alternatively, shock waves can be indirectly observed through the detection of type II radio bursts, commonly associated with shock waves in the solar corona (Vršnak & Cliver 2008).

The AIA instrument, with its exceptional spatial and temporal resolution, has provided significant insights into the dynamics of the low solar corona over the past decade (Patsourakos et al. 2010; Ma et al. 2011; Kozarev et al. 2011). By observing the solar disk in bands 193 and 211 $\AA$, it distinguishes compressive waves in the lower corona, offering valuable information about the kinematics and geometric structure of CBFs. Observations off the solar limb are preferred to study the evolution of the wave's leading front accurately, mitigating projection effects that may introduce ambiguities (Kozarev et al. 2015).

CMEs typically consist of three parts (Fig. 1.2): the CME Front, CME Cavity, and CME Core (Vourlidas et al. 2013). CBFs form in front of the expanding front of CMEs. In situ observations of shock waves classify them into quasi-parallel, quasi-perpendicular, sub-critical, and super-critical shocks based on the angle between the wavefront normal vector and the upstream magnetic field lines (Tsurutani 1985). Coronal waves display diverse morphology and kinematics, ranging from circular fronts to narrow jets or expanding dome-like structures (Veronig et al. 2010). However, fundamental questions persist regarding their physical nature and drivers (Chen 2016; Vršnak & Cliver 2008; Warmuth 2015), including whether they are true wave disturbances or pseudo-wave fronts (Wills-Davey et al. 2007; Vršnak & Cliver 2008; Delannée & Aulanier 1999; Chen et al. 2002).

Extensive observational and modeling studies have been conducted to evaluate these paradigms, but a consensus remains elusive (Patsourakos & Vourlidas 2012; Long et al. 2017). Addressing these outstanding questions is crucial, as coronal waves are being incorporated into models as primary agents producing SEP events and geomagnetic storms following CMEs (Rouillard et al. 2012; Park et al. 2013). The present thesis undertakes an extensive statistical analysis of coronal EUV wave events observed by SDO to provide new insights into their kinematical properties and relationship to CMEs and plasma properties in the corona. It focuses on analyzing their large-scale evolution as a function of distance and direction from the source region, aiming to uncover systematic trends in their propagation kinematics and exploring relationships between different pairs of kinematical parameters compared to previous works.

[1] `https://www.dias.ie/cosmicphysics/astrophysics/astro-surround/`

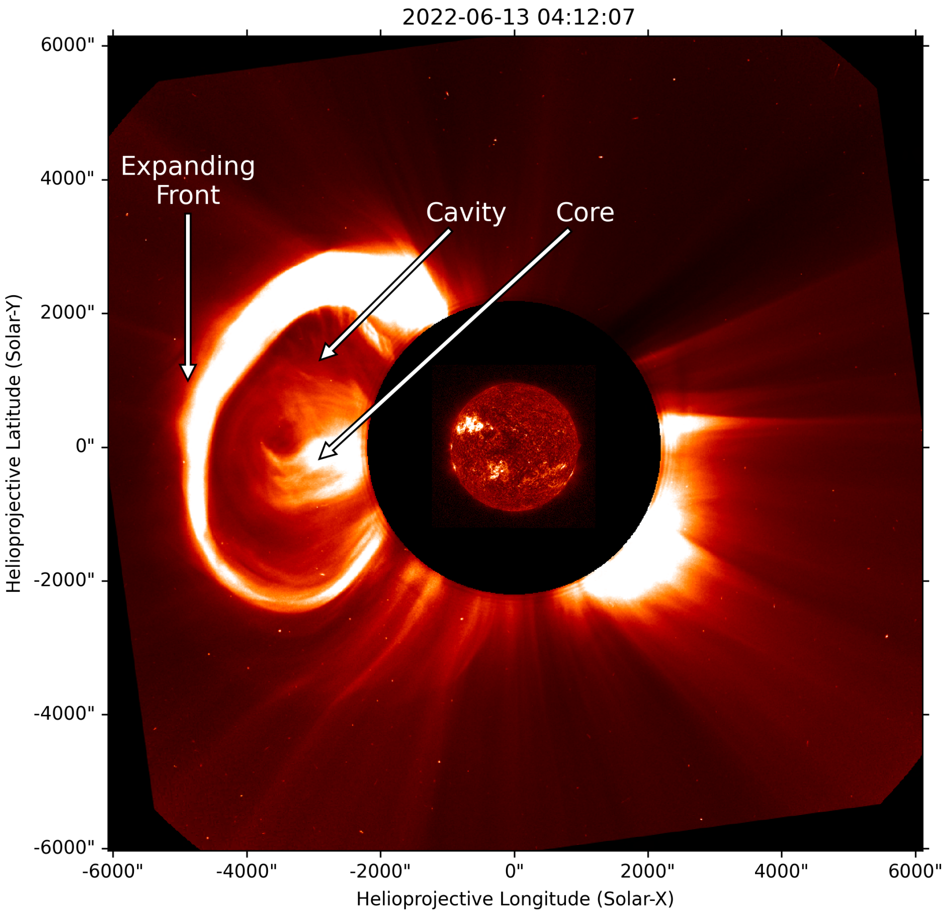


Figure 1.2: Composite image from the AIA and LASCO telescopes on the NASA-GSFC SDO and NASA/ESA SOHO spacecrafts shows a large CME being ejected to the east and its typical structure.

These results have important implications for incorporating coronal waves into predictive models of CMEs and SEP events for future space weather forecasting.

### 1.1.2 Solar Radio Bursts

Solar radio emissions, including solar radio bursts, are extensively studied due to their association with solar activity and potential impacts on Earth's atmosphere and technology. Type III bursts, originating from transient energetic electron beams injected into the corona, serve as remote diagnostics for studying energetic electrons and plasma dynamics (Ergun et al. 1998; Pick et al. 2006; Reid 2020). These bursts, linked to plasma density, offer insights into processes driving solar active phenomena like CMEs and flares (Reid & Ratcliffe 2014; Kontar et al. 2017). They provide valuable information on electron acceleration and transport, shedding light on the dynamic interaction between non-thermal electron distributions and ambient plasma (Melrose 1980).

Pioneering observations in the 1940s led to the classification and subsequent spectrographic studies of solar radio bursts, uncovering emission mechanisms and particle diagnostics (Wild et al. 1963; Suzuki & Dulk 1985). Magnetic reconnection models provided theoretical explanations for particle acceleration generating these bursts (Holman et al. 2011). Radio imaging spectroscopy enables tracking of radio sources on the Sun, offering insights into energetic particle transport from the Sun to Earth (Krucker et al. 2011; Klassen et al. 2003a,b). Different burst types are observed and classified based on their spectral characteristics (Fig. 1.3) (Wild et al. 1963), with this thesis focusing on a detailed analysis of solar type III radio bursts.

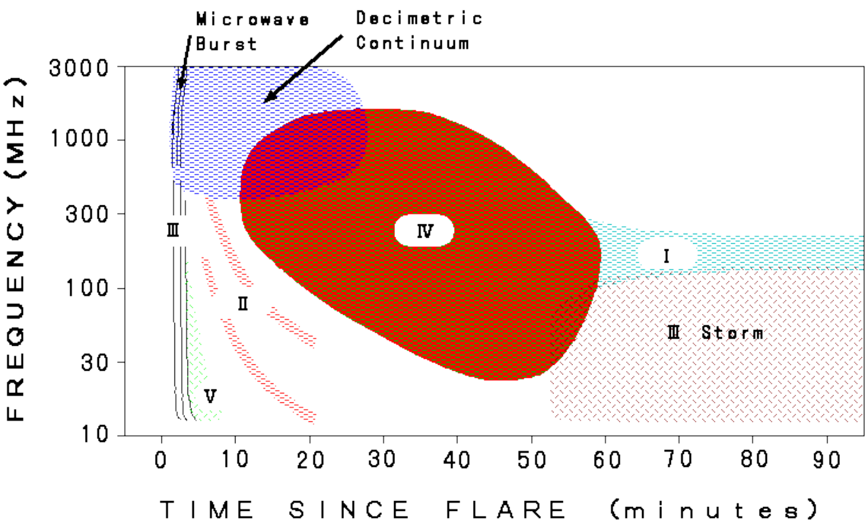


Figure 1.3: Diagram illustrating the classification of solar radio bursts. Image courtesy[2]

Type III bursts manifest as intense enhancements of radio flux with rapid frequency drifts, observable across a broad frequency spectrum from GHz to kHz (Wild & McCready 1950; Lecacheux et al. 1989; Bonnin et al. 2008). They arise from energetic electron beams ejected during magnetic reconnection, with the rapid drift corresponding to the beams' propagation from the Sun's lower corona outward along open magnetic field lines (Cane et al. 2002; MacDowall et al. 2003). Investigating their source locations, plasma environments, and beam kinematics is vital for understanding coronal particle acceleration and transport relevant to SEP forecasting models.

Despite over 50 years of study, gaps persist in understanding the exciter beams and emission mechanisms of type III bursts, including detailed electron acceleration sites, beam configurations, burst onset drivers, and the role of density fluctuations in beam propagation (Reid & Kontar 2018b,a; Li & Cairns 2012). Recent work combining imaging and spectral data with modeling aims to constrain radio burst exciters in detail (Chen et al. 2013; Kontar et al. 2017), yet challenges remain in reconciling models with observations and predicting radio diagnostics. Coordinated observations and modeling efforts can advance knowledge in these areas, aiding predictions of energetic electron properties based on radio diagnostics. This thesis undertakes a detailed investigation of a solar type III burst, deriving electron beam trajectories, coronal densities, and emission sources, providing insights into the corona plasma environment and energetic electron transport relevant to SEP forecasting applications.

### 1.1.3 Solar Energetic Protons Forecasting

Solar energetic protons (SEPs) are high-energy particles originating from solar flares and CMEs, characterized by their high energy levels (up to the GeV/nucleon range) and potential to cause radiation damage (Aschwanden 2002; Lin 2005; Reames 2013). Their fluence and energy spectrum depend on various factors, including solar activity strength and interplanetary conditions (Kahler et al. 1984, 1987; Debrunner et al. 1988; Miteva et al. 2013; Trottet et al. 2015; Dierckxsens et al. 2015; Le & Zhang 2017; Gopalswamy et al. 2017). SEPs exhibit a strong association with the solar cycle, peaking during its maximum phase (Reames 2013), although the exact relationship remains complex and not fully understood (Nymmik 2007; Ramstad et al. 2018).

Figure 1.4 illustrates the impact of SEPs during the *Halloween storm* of 2003, a significant solar event. SEPs play a crucial role in adverse space weather, posing radiation hazards to humans and equipment in space (Reames 1999). SEP events consist primarily of protons accelerated by CME-driven shock waves, with gradual events involving protons above $\sim 10$ MeV and impulsive events dominated by electrons and ions like $^3$He (Reames 2013; Nitta et al. 2015).

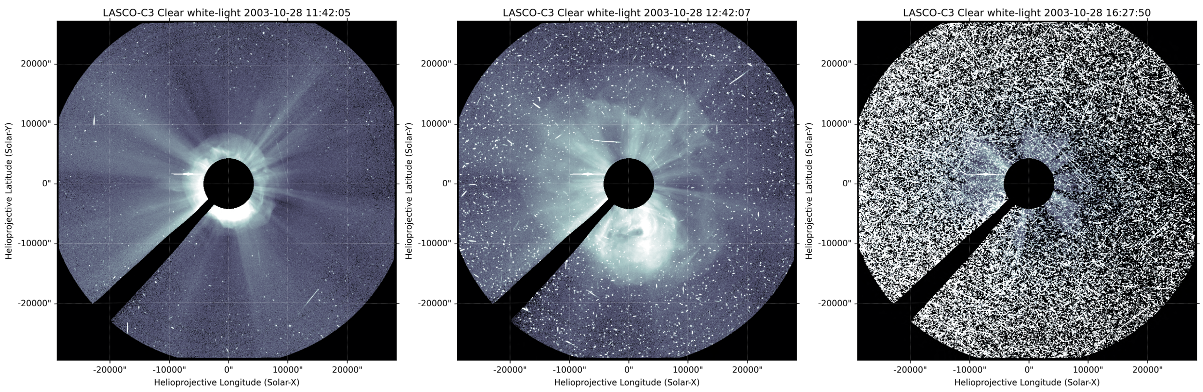


Figure 1.4: Coronagraph image captured by the SOHO/LASCO C3 instrument during a Halo-CME event. The speckled appearance of the corona results from signal contamination due to particles generated when SEPs interact with the SOHO telescope.

SEP forecasting models face challenges due to the complex physics involved, motivating the exploration of data-driven approaches using machine learning (Kahler et al. 2007; Laitinen & Dalla 2017). Deep learning techniques offer promising avenues for improved predictions, capturing complex relationships between parameters (Florios et al. 2018; Camporeale 2019). This thesis aims to develop deep Neural Network models for predicting SEP intensity profiles, leveraging historical data to enhance forecasting capabilities.

## 1.2 Objectives and Scope

This PhD thesis explores various solar phenomena, including CBFs, type III radio bursts, and SEP events, aiming to deepen our understanding of solar corona physics and its relation to eruptions and energetic particle radiation.

For CBFs, the research analyzes 26 historical events observed by the AIA instrument on SDO from 2010 to 2017, examining their properties and kinematics in relation to the coronal plasma environment. Techniques like base-difference images and geometric models are employed to derive measurements, alongside exploring shock properties within the CBFs.

The study of type III radio bursts focuses on unraveling their generation mechanisms, identifying their sources in the solar corona, and investigating relationships with magnetic field structures and plasma environment. It analyzes specific bursts observed on April 3, 2019, using data from LOFAR and PSP instruments, comparing observations with existing models and exploring potential burst sources.

[2]Types of solar radio bursts: `http://solar.physics.montana.edu/takeda/radio_burst/srb.html`

In SEP forecasting, the aim is to develop a BiLSTM neural network model capable of predicting daily SEP integral flux over a three-day window for energy ranges >10 MeV, >30 MeV, and >60 MeV. The model's performance is evaluated against established forecasting models using historical SEP data from the past four solar cycles, assessing accuracy and effectiveness through various metrics and correlation analysis.

By addressing these aspects of solar activity, this research advances our understanding of solar dynamics and enhances our ability to predict space weather events impacting Earth.

## 1.3 Outlines

This dissertation examines CBFs, solar radio bursts, and SEP events. It analyzes the kinematics of CBFs in the solar corona, investigating 26 CBFs associated with SEP events observed between 2010 and 2017. The study employs the SPREAdFAST framework to understand CBF kinematics and plasma parameters, aiding space weather forecasting and SEP event studies (Chapter 2). Additionally, it presents a method for identifying and tracking CME-driven shock waves using wavelet transform and image filtering, with applications in deep-learning solar datasets.

Another study in Chapter 2 explores the correlation between geomagnetic storm intensity and solar and interplanetary phenomena, emphasizing the importance of considering CME speed and magnetic structure orientation for accurate storm prediction. Chapter 3 focuses on type III radio bursts, analyzing an event on April 3, 2019, and characterizing 16 bursts using multi-wavelength data and models, revealing insights about plasma conditions along burst trajectories.

Chapter 4 investigates SEP events, modeling their acceleration and transport during coronal shock events through the SPREAdFAST framework, and developing SEP forecasting models using a BiLSTM neural network. The effectiveness of these models is validated through testing and benchmarking against existing ones. Finally, Chapter 5 summarizes the dissertation's key findings.

# Chapter 2

# Remote Observations

## Early-stages and Later-stages of Eruption

This chapter covers three main topics related to EUV waves and CMEs. Firstly, it focuses on the kinematics of CBFs in both the lower and middle/outer coronas, along with an examination of coronal plasma conditions during these eruptions. Additionally, it discusses my contributions to testing and debugging the *Wavetrack* Python library, developed by Stepanyuk et al. (2022), for detecting and tracking solar features using wavelet transforms and filtering techniques. Lastly, it examines the research led by Miteva et al. (2023) regarding the connection between reconstructed 3D CME models and geomagnetic storm intensity, emphasizing the importance of accurate 3D modeling for space weather forecasting. The chapter will present the results of each topic individually, followed by a combined discussion and concluding remarks.

## 2.1 Introduction

CMEs are prominent indicators of solar activity, observable through various wavelengths including white light, UV, and radio (Vourlidas et al. 2003; Zhang & Dere 2006; Bein et al. 2011; Bastian et al. 2001; Veronig et al. 2010). Early CME phases are effectively observed in Extreme Ultraviolet (EUV) light, facilitated by instruments like AIA aboard SDO (Lemen et al. 2011; Pesnell et al. 2012). CMEs can induce shock waves in the solar corona, visible as EUV waves or CBFs (Thompson et al. 1998; Long et al. 2011).

CBFs are disturbances propagating over the solar disk and limb, often faster than local characteristic speeds, driven primarily by CMEs or solar flares (Thompson et al. 1998; Veronig et al. 2010; Vršnak & Cliver 2008; Magdalenić et al. 2010b; Nindos et al. 2011). They appear as dome-shaped structures in radio and white-light observations, composed of denser plasma and thus appearing brighter in images (Pick et al. 2006; Nindos et al. 2008; Thompson & Myers 2009).

Studies have clarified CBF characteristics both on the solar disk and off the limb, confirming their wave-like nature (Nitta et al. 2013; Long et al. 2011; Olmedo et al. 2012). Observations from instruments like LASCO onboard SOHO have extended shock wave investigations beyond 2.5 $R_\odot$ (Domingo et al. 1995; Vourlidas et al. 2003). While EUV observations link CMEs and EUV waves, understanding shock waves in EUV remains incomplete (Patsourakos & Vourlidas 2009; Kozarev et al. 2011). Emission measure modeling using AIA's EUV channels provides insights into temperature and density changes in the wavefront's sheath (Kozarev et al. 2011). Multi-wavelength observations from SOHO/LASCO and SDO/AIA instruments have revealed valuable information about CBF properties near the Sun (Warmuth 2015). Factors such as nearby active regions or coronal holes can distort CBF morphology, and a connection between CBFs and chromospheric disturbances known as Moreton waves has been established (Ofman & Thompson 2002; Mann et al. 2003; Piantschitsch et al. 2018; Thompson et al. 1999).

In this study, I analyzed 26 CBF events up to $\sim 17\,R_\odot$ using observations and modeling tools from the Solar Particle Radiation Environment Analysis and Forecasting–Acceleration and Scattering Transport (SPREAdFAST) framework (Kozarev et al. 2022). The study aims to characterize CBF kinematics and estimate ambient plasma properties to understand the relationships between shock and plasma parameters.

Table 2.1: List of the CBF events with their associated flares and CMEs.

| ID | Event Date | Flare Start (UT) | Flare Max (UT) | Flare Class | EUV Wave Start (UT) | EUV Wave End (UT) | Source X (") | Source Y (") | CME on | $V_{CME}$ | AW |
|---|---|---|---|---|---|---|---|---|---|---|---|
| 0 | 2010/06/12 | 0:30 | 0:57 | 20 | 0:55 | 1:19 | 633 | 390 | 1:32 | 486 | 119 |
| 1 | 2010/08/14 | 9:38 | 10:05 | 4.4 | 9:30 | 10:08 | 697 | -26 | 10:12 | 1205 | 360 |
| 2 | 2010/12/31 | 4:18 | 4:25 | 1.3 | 4:15 | 5:01 | 799 | 246 | 5:00 | 363 | 45 |
| 3 | 2011/01/28 | 0:44 | 1:03 | 13 | 0:45 | 1:59 | 949 | 218 | 1:26 | 606 | 119 |
| 4 | 2011/03/07 | 19:43 | 20:12 | 37 | 19:31 | 22:59 | 614 | 553 | 20:00 | 2125 | 360 |
| 5 | 2011/05/11 | 2:23 | 2:43 | 0.81 | 2:20 | 2:35 | 785 | 399 | 2:48 | 745 | 225 |
| 6 | 2011/08/04 | 3:41 | 3:57 | 93 | 3:43 | 4:20 | 546 | 200 | 4:12 | 1315 | 360 |
| 7 | 2011/08/08 | 18:00 | 18:10 | 35 | 17:45 | 18:43 | 812 | 215 | 18:12 | 1343 | 237 |
| 8 | 2012/03/07 | 1:05 | 1:14 | 130 | 0:00 | 0:40 | -475 | 397 | 1:30 | 1825 | 360 |
| 9 | 2012/03/13 | 17:12 | 17:41 | 79 | 17:03 | 17:44 | 804 | 352 | 17:36 | 1884 | 360 |
| 10 | 2012/07/23 | u | u | u | 2:09 | 2:48 | 912 | -243 | 2:36 | 2003 | 360 |
| 11 | 2013/04/21 | u | u | u | 6:35 | 7:35 | 937 | 181 | 7:24 | 919 | 360 |
| 12 | 2013/05/13 | 15:48 | 16:05 | 280 | 15:44 | 16:20 | -927 | 186 | 16:08 | 1850 | 360 |
| 13 | 2013/05/15 | 1:25 | 1:48 | 120 | 1:06 | 1:50 | -852 | 199 | 1:48 | 1366 | 360 |
| 14 | 2013/05/22 | 13:08 | 13:32 | 50 | 12:33 | 13:20 | 875 | 238 | 13:26 | 1466 | 360 |
| 15 | 2013/06/21 | 2:30 | 3:14 | 29 | 2:31 | 3:21 | -869 | -268 | 3:12 | 1900 | 207 |
| 16 | 2013/10/25 | 7:53 | 8:01 | 170 | 7:53 | 8:29 | -914 | -158 | 8:12 | 587 | 360 |
| 17 | 2013/12/12 | 3:11 | 3:36 | 0.22 | 3:03 | 3:33 | 750 | -450 | 3:36 | 1002 | 276 |
| 18 | 2013/12/28 | 17:53 | 18:02 | 9.3 | 17:10 | 18:00 | 942 | -252 | 17:36 | 1118 | 360 |
| 19 | 2014/07/08 | 16:06 | 16:20 | 65 | 16:06 | 16:51 | -767 | 163 | 16:36 | 773 | 360 |
| 20 | 2014/12/05 | 5:28 | 5:37 | 2.1 | 5:42 | 6:21 | 872 | -366 | 6:24 | 534 | 172 |
| 21 | 2015/05/12 | 2:15 | 3:02 | 2.6 | 2:18 | 2:49 | 960 | -192 | 2:48 | 772 | 250 |
| 22 | 2015/09/20 | 17:32 | 18:03 | 21 | 17:28 | 18:11 | 660 | -429 | 18:12 | 1239 | 360 |
| 23 | 2015/10/29 | u | u | u | 2:13 | 2:52 | 951 | -167 | 2:36 | 530 | 202 |
| 24 | 2015/11/09 | 12:49 | 13:12 | 39 | 12:51 | 13:27 | -626 | -229 | 13:25 | 1041 | 273 |
| 25 | 2017/04/01 | 21:35 | 21:48 | 44 | 21:31 | 22:19 | 761 | 308 | 22:12 | 516 | 115 |

## 2.2 EUV Observations

We conducted a study utilizing data from the SOHO/ERNE instrument, focusing on proton events with energies between 17-22 MeV, spanning from 2010 to 2017. Initially, 216 events were identified, but after stringent selection criteria were applied, 133 events were excluded due to various factors such as the absence of EUV wave associations, CMEs, or flares. This left us with a final set of 26 events for analysis. The selected events (Table 2.1), previously discussed in (Kozarev et al. 2022), were further examined using imagery from the AIA instrument's EUV channel 193 $\AA$. These images, captured at a 24-second cadence, provided the primary input for our analysis within the SPREAdFAST framework.

Detailed information about the selected events, including their start/end times, associated flares, and source locations on the solar disk, was obtained from the Heliophysics Events Knowledge (HEK) database. Notably, the mean latitude and longitude of the CBFs were calculated, along with their distribution across the solar hemispheres and quadrants. CBFs, observed as faint quasi-spherical sheaths, were primarily visible in the 193 $\AA$ channel. To analyze their evolution, sequences of base-difference images were generated for each event, allowing us to track their propagation over time (Vourlidas et al. 2003; Ontiveros & Vourlidas 2009; Kozarev et al. 2011; Ma et al. 2011).

The mean latitude and mean longitude of the CBFs were calculated as 56.35 and 378.04 arcsec, respectively. Additionally, the mean latitudes of CBFs in the northern and southern solar hemispheres were found to be 283.00 and -252.73 arcsec, respectively. As for the mean longitudes, they were -775.71 and 803.11 arcsec on the eastern and western sides, respectively.

To analyze the kinematics of CBFs, the Coronal Analysis of SHocks and Waves framework (Kozarev et al. 2017, CASHeW) was employed. This semi-automated technique involved extracting annular regions from AIA images and mapping them onto polar projections (Fig. 2.1). By tracking intensity changes along radial and lateral directions, we could measure the kinematics of the CBFs.

Furthermore, plasma parameters and modeling were performed using information retrieved from the HEK database and Nariaki Nitta's catalog of coronal waves (Nitta et al. 2013). The SPREAdFAST framework facilitated calculations of kinematics, inference of shock parameters, and determination of plasma properties for each event.

To accurately determine the positions of CBFs over time, we employed several algorithms, including Savitzky-Golay filtering (Savitzky & Golay 1964) for data smoothening and local minima/maxima ordering for identifying wave positions. Additionally, we manually specified starting and ending times for each CBF event and determined their corresponding heights above the solar limb.

By analyzing intensity values, we defined the positions of CBFs at each time step, considering the front

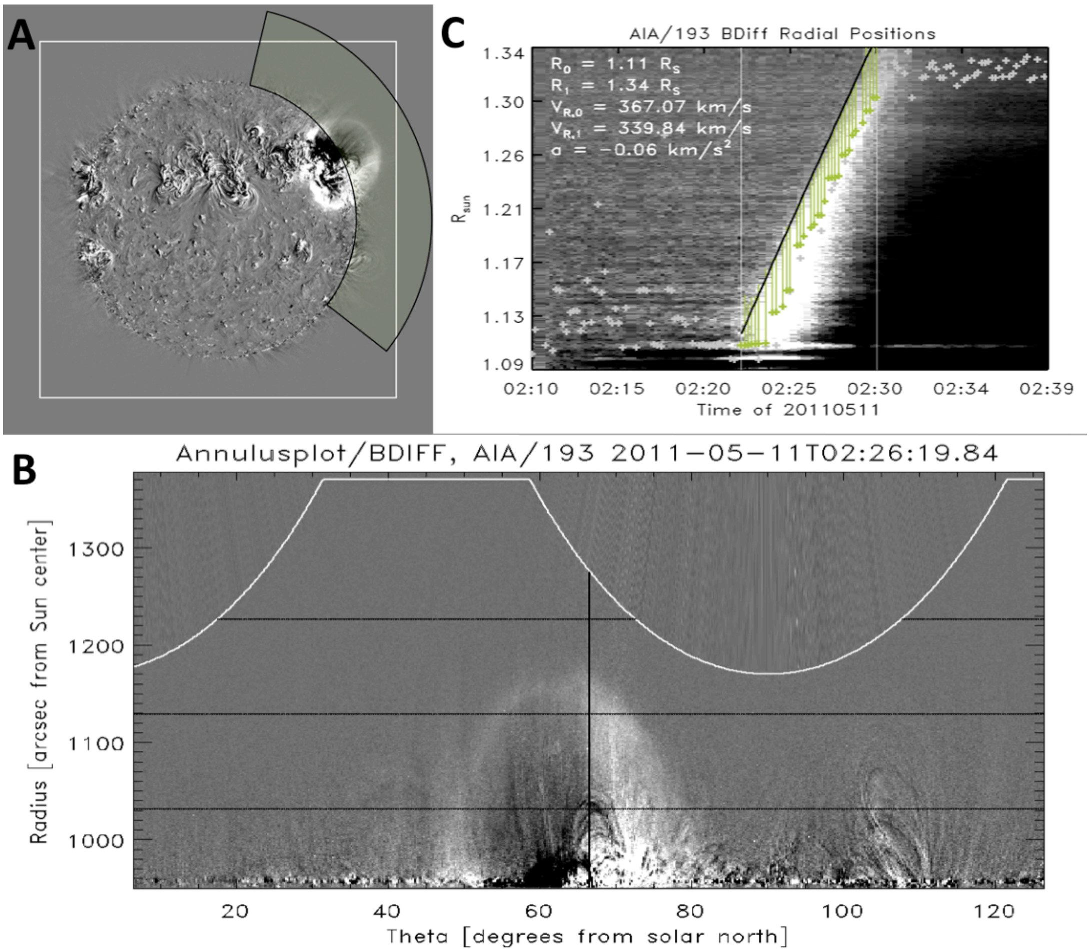


Figure 2.1: Illustration for the annulus method used to extract kinematic data from AIA images. (A) shows the full Sun disk with the relevant region highlighted for analysis (green sector). The white box outlines the AIA FOV. (B) displays the extracted annular region mapped onto polar coordinates, with the actual data extent marked by the white curve. Black lines indicate the directions used for measuring radial and lateral motions. (C) shows a stacked plot of intensity along the radial direction, with green markers highlighting intensity peaks and their corresponding distances from the CBF wavefront. The white lines represent the time interval during which the CBF is tracked within the AIA FOV. This figure is curated from (Kozarev et al. 2017).

and back of the wave to be at 20% of the peak intensity. Furthermore, we applied mathematical techniques such as Levenberg-Marquardt least squares minimization (Markwardt 2009) and bootstrapping optimization (Efron 1979) to fit fourth-order polynomials to the wave positions, enabling measurements of speeds, accelerations, intensities, and thicknesses in both radial and lateral directions.

Finally, measurements of CBF heights and lateral positions were obtained relative to the solar disk and wavefront direction, respectively, providing comprehensive insights into the dynamics of these solar phenomena. For further reference, the HEK database[1], Nariaki Nitta's catalog of coronal waves[2], and the LASCO CME Catalog[3] were utilized, along with detailed summary plots available in the online SPREAdFAST catalog[4].

## 2.3 Data Analysis and Methods

The Solar Particle Radiation Environment Analysis and Forecasting—Acceleration and Scattering Transport (SPREAdFAST) system, developed by Kozarev et al. (2022) and referred to as SPREAdFAST throughout this discussion, operates as a physics-based prototype for forecasting SEP events within the heliosphere. Built upon the CASHeW framework, SPREAdFAST integrates data-driven models to forecast various aspects of SEP events, including arrival times, maximum intensities, and fluxes at different locations in the inner heliosphere. These predictions play a vital role in space weather forecasting, contributing to the protection of assets owned by the European Space Agency (ESA) and aiding satellite operators in making informed decisions to mitigate the impacts of space weather on electronics and human activities in space (Kozarev et al. 2022).

The SPREAdFAST catalog offers summary plots of J-maps and kinematic data for each SEP event, as highlighted by Kozarev et al. (2022). Additionally, to ensure consistency in lateral kinematic measurements, an averaging technique is applied to data from both lateral left and right flanks, as described by the same authors. Further analysis involves the application of a Savitzky-Golay fit, as outlined in previous work by Kozarev et al. (2019), and the utilization of analytical models for CME kinematics by Gallagher et al. (2003) and Byrne et al. (2013) to extrapolate smoothed radial positions up to $\sim 17\,R_\odot$.

Moving forward, the development of synthetic shock models (S2M) forms the next phase of the study, as mentioned by Kozarev et al. (2022). These models, operating at a 24-second cadence, are constructed based on extrapolated radial and lateral kinematic results and incorporate major and minor axes of spheroids representing compressive waves. The shock surface is delineated from the onset of the CBF until its nose reaches 10 $R_\odot$ and then extended up to 30 $R_\odot$ utilizing results from the Magnetohydrodynamic Algorithm outside a Sphere (MAS) synoptic coronal model.

The methodology for estimating shock density jump is detailed by Kozarev et al. (2017), involving the calculation of differential emission measure (DEM) during and before the event at each shock crossing and timestep. This approach, informed by Cheung et al. (2015), provides insights into the variation in density across shock structures. Notably, while the density jump within the AIA FOV typically remains below 1.2, regions beyond observational limits are assigned a value of 1.2, assuming the presence of weak shocks.

To facilitate analysis, the synthetic shock model is segmented into distinct regions–the cap representing the shock nose, Zone 1, and Zone 2 representing the shock flanks–as explained by Kozarev et al. (2022). This segmentation aids in the examination of plasma parameter distributions across different sectors of the shock surface, as depicted in Figure 2.2.

## 2.4 CBF Kinematics and Geometric Modeling: Case Study May 11, 2011

In this section, I analyze a case study event in the low corona region and investigate plasma parameters along shock-crossing magnetic field lines in the AIA FOV.

[1]HEK Database: www.lmsal.com/isolsearch
[2]Nariaki Nitta's Catalog: https://lmsal.com/nitta/movies/AIA_Waves/index.html
[3]LASCO CME Catalog: https://cdaw.gsfc.nasa.gov/CME_list/
[4]SPREAdFAST Catalog: https://spreadfast.astro.bas.bg/catalog/

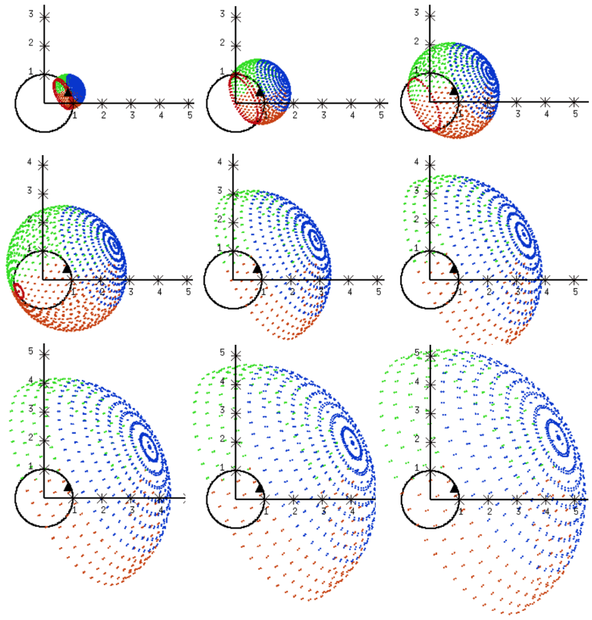

Figure 2.2: Synthetic shock model divided into three segments; the cap zone in blue and the flank zones are in red and green.

### 2.4.1 Event Context

The eruption occurred on May 11, 2011, at around 02:20 UT (Fig. 2.3), originating from an active region in the northwestern sector (N18W52). It involved a massive shock wave propelled by a fast partial-halo CME, with a linear speed of 745 $km\,s^{-1}$, a $2^{nd}$-order speed at $20\,R_{\odot}$ of 776 $km\,s^{-1}$, and an acceleration of 3.3 m $s^{-2}$. The eruption was accompanied by a weak B8.1 solar flare and an eruptive filament observed by the SDO/AIA instrument.

Additionally, a type II radio burst was associated with the eruption, observed by the Learmonth spectrogram. Proton fluxes near 1 AU showed an increase, and an SEP event was detected at Earth with onset time of 03:39 UT and a $J_p$ of 0.0133 protons/(cm$^2$ s sr MeV) in the energy channel 17-22 MeV (Miteva et al. 2016, 2017). $J_p$ is the peak proton intensity after subtracting the pre-event level.

### 2.4.2 Low Corona Part

To investigate the kinematics of the CBF event, I employed the CASHeW module within the SPREAdFAST framework. The shock wave's asymmetrical evolution is detailed, along with its morphological changes over time. The average speeds and accelerations for the radial and lateral directions are provided (Fig. 2.4), along with a comparison of wave thickness between flanks. The shock surface is divided into segments for further analysis (Fig. 2.2). Table 2.2 provides a summary of the statistical results, and the results for the three segments are summarized in Table 2.3.

Moreover, shock-crossing magnetic field lines during this event were investigated in (Kozarev et al. 2022), with key plasma parameters analyzed up to $10\,R_{\odot}$. The aspect ratio of the coronal wave's geometry is discussed, along with changes in shock-field angle and magnetic field amplitude over time and radial distance.

### 2.4.3 Middle/Outer Corona Part

Complementary measurements from the SOHO/LASCO instrument[5] expand the analysis of EUV waves' kinematics in the middle/outer corona. The height-time profile of the CME leading edge associated with the coronal wave is examined, employing fitting models of Gallagher et al. (2003) and Byrne et al. (2013) to analyze the data (Fig. 2.5). Insights into the wave's acceleration and speed variation over time and distance from the Sun are provided (Fig. 2.6).

[5]LASCO CME Catalog: `https://cdaw.gsfc.nasa.gov/CME_list/`

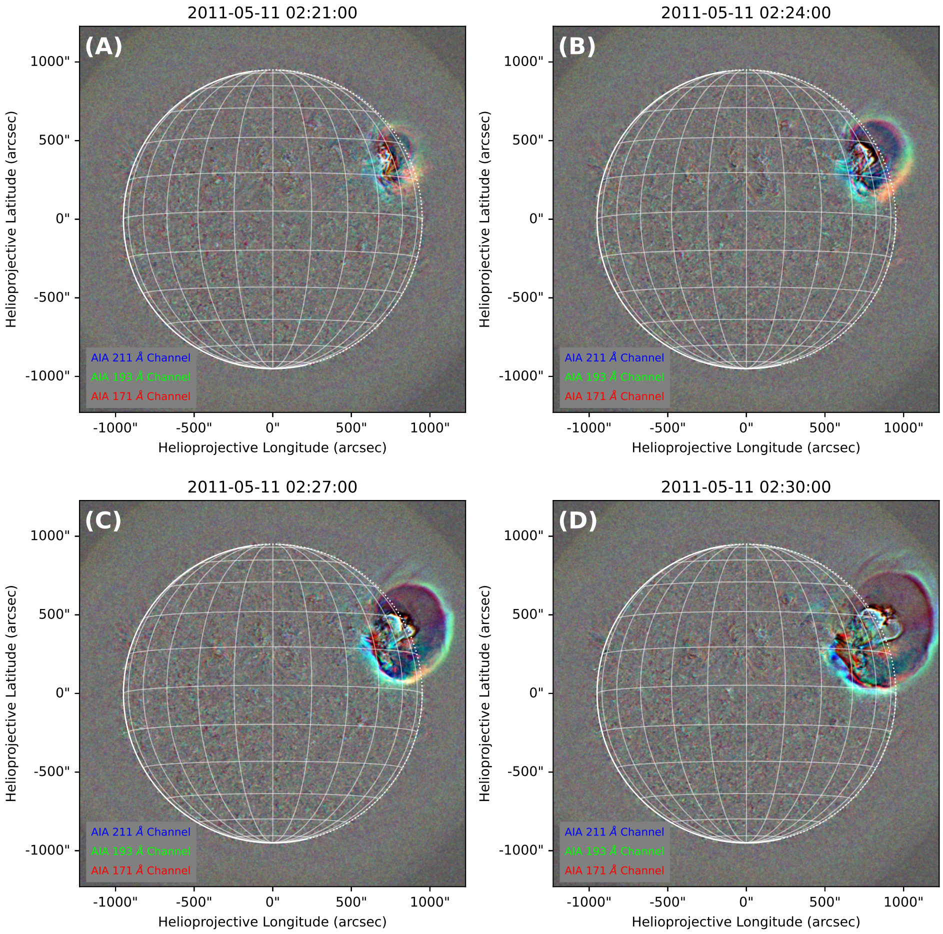


Figure 2.3: AIA running-difference images capture a coronal wave evolving over 9 minutes near the Sun's western limb, exhibiting markedly changing intensity and structure as observed in 171, 193, and 211 Å.

Table 2.2: Mean values and their standard deviation of the wave parameters in the radial direction and the lateral direction for the left and right flanks, at the front, peak, and back sides of the wave for the event occurred on May 11, 2011, in the SDO/AIA FOV.

| Parameter | Direction | Front | Peak | Back |
|---|---|---|---|---|
| | Lat. Left | 218.46 ± 9.04 | 297.46 ± 5.45 | 293.94 ± 9.04 |
| $< speed >$ $km\, s^{-1}$ | Radial | 427.46 ± 51.85 | 433.11 ± 82.86 | 400.81 ± 83.78 |
| | Lat. Right | 494.69 ± 0.00 | 509.25 ± 1.02 | 498.97 ± 9.21 |
| | Lat. Left | -414.62 ± 227.23 | -401.46 ± 164.62 | -385.77 ± 227.23 |
| $< accel. >$ m s$^{-2}$ | Radial | 147.41 ± 1009.19 | 758.97 ± 1287.65 | 485.38 ± 1365.80 |
| | Lat. Right | -415.04 ± 0.00 | -209.81 ± 22.32 | -266.68 ± 250.80 |
| | Lat. Left | 250.60 ± 5.90 | | |
| $< intensity >$ DN | Radial | 403.34 ± 143.30 | | |
| | Lat. Right | 489.04 ± 2.86 | | |
| | Lat. Left | 0.07 ± 0.00 | | |
| $< thickness > R_\odot$ | Radial | 0.04 ± 0.01 | | |
| | Lat. Right | 0.09 ± 0.00 | | |

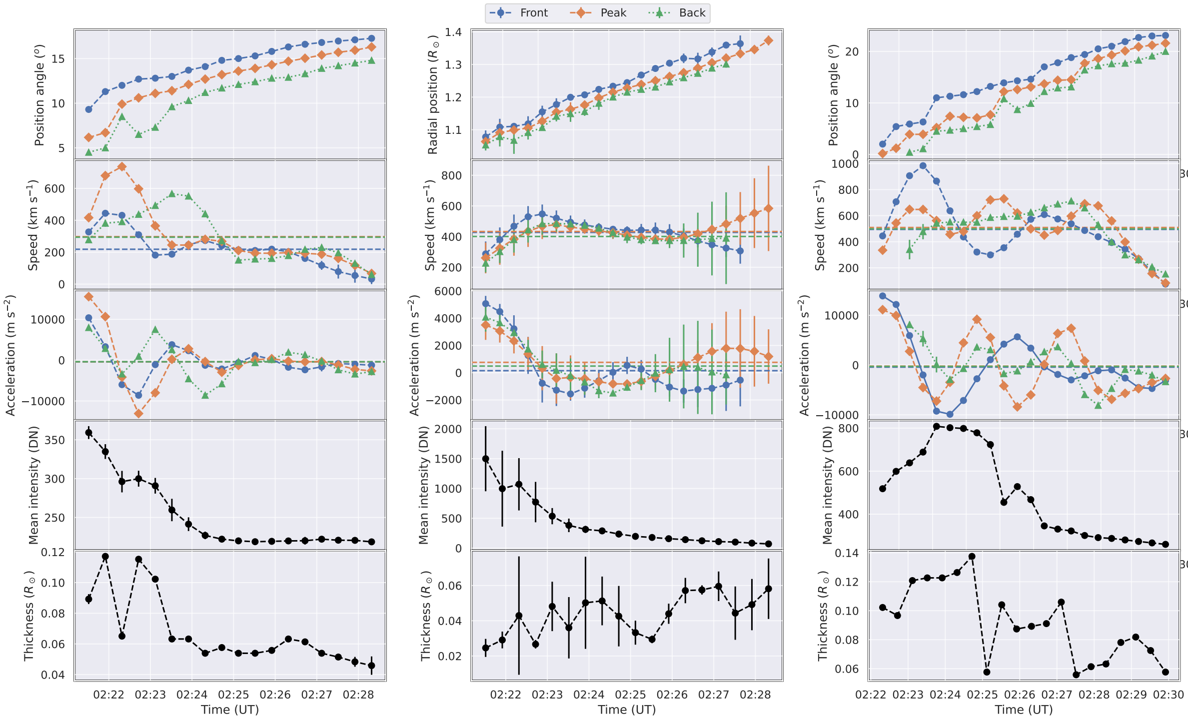


Figure 2.4: Time-series kinematics of the CBF parameters for the front, peak, and back positions in the AIA FOV, with measurement uncertainties shown as small bars over the data points. The horizontal lines in the speed and acceleration panels denote the mean speeds and accelerations for the wave front, peak, and back with respective colors. The left and right columns represent the lateral kinematic measurements in the left and right flanks of the wave, respectively. The middle column represent the kinematic measurements in the radial direction.

Table 2.3: Mean, median, and standard deviation of the shock parameters output, from the interaction of the S2M spheroid with the MAS MHD model results, for the shock's cap and flanks and for the whole shock surface, for the event on May 11, 2011.

| Segment | Parameter | Statistics | | |
|---|---|---|---|---|
| | | Mean | Median | Stdv |
| All | $V_{SHOCK}$ $km\,s^{-1}$ | 577.77 | 578.39 | 72.79 |
| | $\theta_{BN}$ $^o$ | 70.06 | 0.63 | 44.83 |
| | $B_{MAG}$ G | 0.046 | 0.038 | 0.070 |
| | Density Jump | 1.193 | 1.188 | 0.185 |
| Cap | $V_{SHOCK}$ $km\,s^{-1}$ | 555.18 | 550.86 | 42.46 |
| | $\theta_{BN}$ $^o$ | 19.37 | 3.61 | 25.51 |
| | $B_{MAG}$ G | 0.046 | 0.036 | 0.070 |
| | Density Jump | 1.193 | 1.188 | 0.015 |
| Zone 1 | $V_{SHOCK}$ $km\,s^{-1}$ | 613.69 | 609.32 | 59.42 |
| | $\theta_{BN}$ $^o$ | 6.46 | 0.21 | 50.92 |
| | $B_{MAG}$ G | 0.045 | 0.045 | 0.066 |
| | Density Jump | 1.190 | 1.187 | 0.008 |
| Zone 2 | $V_{SHOCK}$ $km\,s^{-1}$ | 631.37 | 614.23 | 73.07 |
| | $\theta_{BN}$ $^o$ | 0.10 | 0.51 | 10.61 |
| | $B_{MAG}$ G | 0.046 | 0.029 | 0.071 |
| | Density Jump | 1.194 | 1.188 | 0.016 |

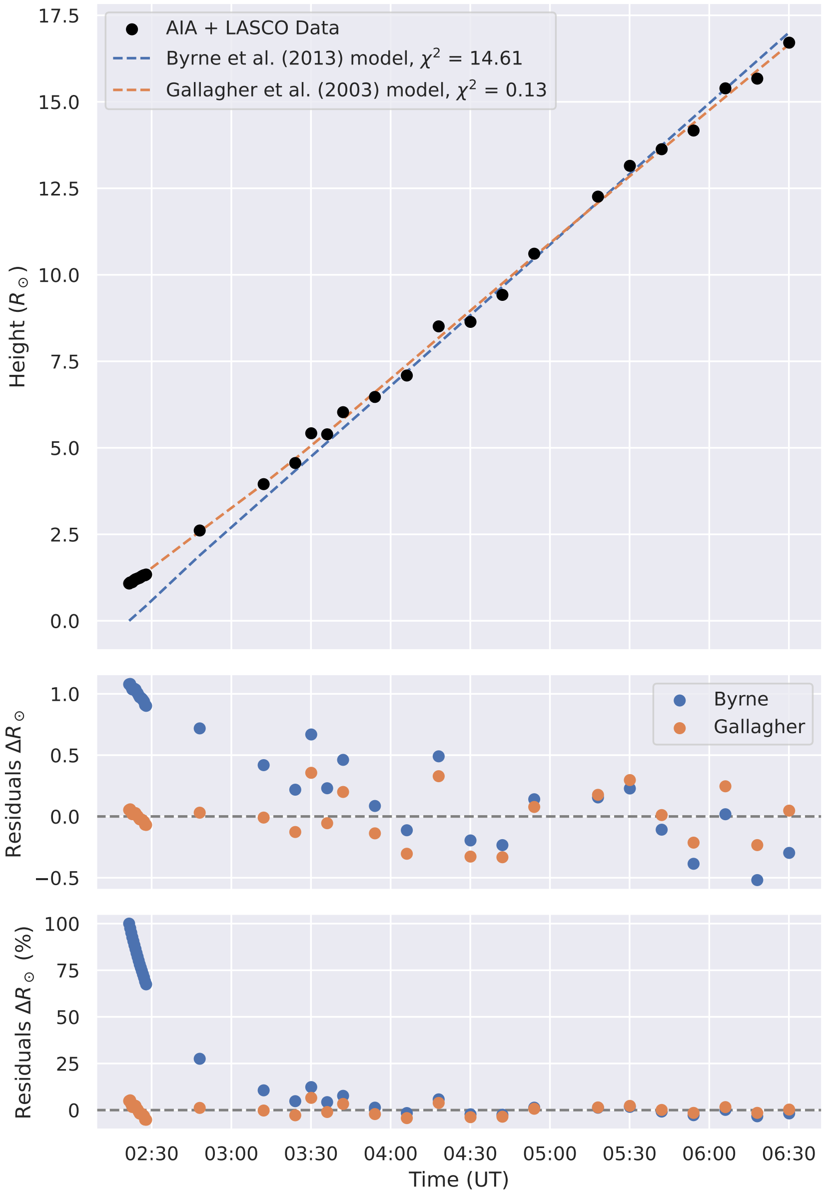


Figure 2.5: Top panel – Height-time profile compiled from AIA and LASCO measurements for the event occurred on May 11, 2011, fitted with two CME kinematics models from the photosphere up to 17 $R_\odot$ . Middle panel – Difference between the fitting and the real observations. Bottom panel – Relative residuals in %.

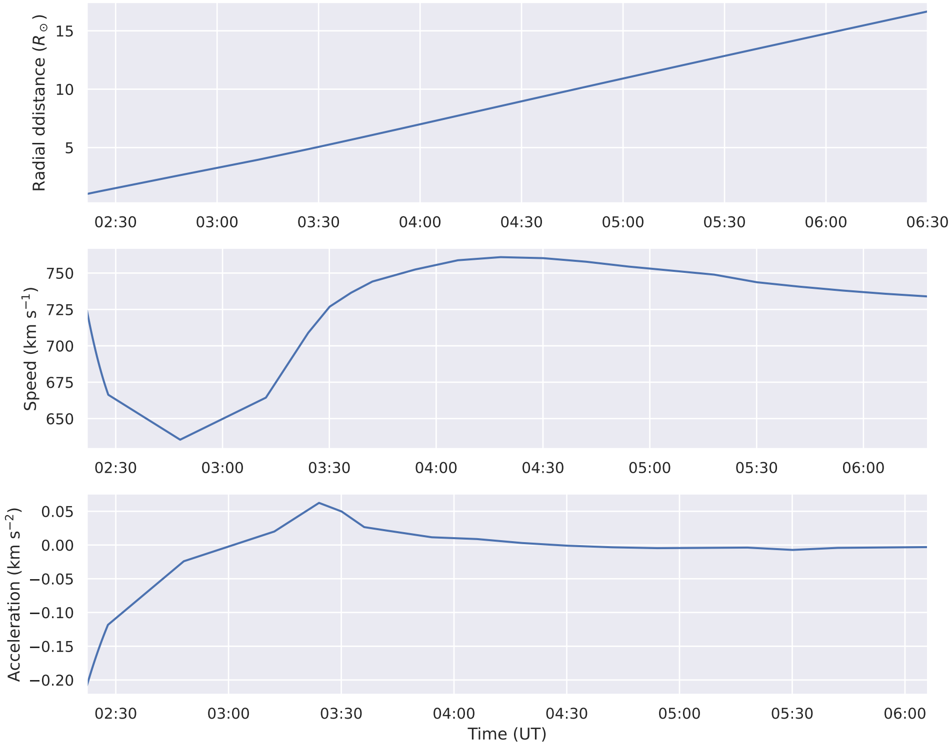


Figure 2.6: Extrapolated radial kinematics for the event occurred on May 11, 2011, based on the ballistic model of Gallagher et al. (2003) up to 17 $R_\odot$ .

## 2.5 Statistical Study

I conduct a thorough statistical analysis of coronal wave events observed in the AIA and LASCO FOVs, focusing on kinematic characteristics and plasma parameters.

Table 2.4 summarizes statistical parameters related to shock characteristics, such as wave speed, intensity, and thickness in the AIA FOV. Analysis reveals higher speeds, accelerations, lower mean intensities, and thickness in the radial direction compared to the lateral direction, suggesting early elongation of waves near the Sun.

Figure 2.7 illustrates EUV waves' kinematics evolution in the AIA FOV, showing parameter distributions as a function of distance for shock speed, acceleration, wave intensity, and thickness in radial and lateral directions. Speed and intensity decline with distance due to momentum loss and decreasing plasma densities. All dynamic spectra for individual events are accessible on the SPREAdFAST catalog webpage[6].

Table 2.4: Statistics of the EUV wave kinematics in the SDO/AIA FOV for the 26 events. LL and LR refer to the lateral left and right flanks, respectively. Rad refer to the radial front direction.

| | | Speed ( $km\,s^{-1}$ ) | | | Accel. (km s$^{-2}$) | | | Intensity (DN) | | | Thickness ( $R_\odot$ ) | | |
|---|---|---|---|---|---|---|---|---|---|---|---|---|---|
| | Aspect ratio | LL | Rad | LR | LL | Rad | LR | LL | Rad | LR | LL | Rad | LR |
| Max | 2.00 | 1574.81 | 2053.73 | 983.58 | 28.19 | 81.01 | 13.89 | 1348.87 | 2431.95 | 1498.45 | 9.600 | 0.185 | 6.100 |
| Min | 0.84 | 2.11 | 40.30 | 2.30 | -35.24 | -81.01 | -9.89 | 0.53 | 0.17 | 150.30 | 0.027 | 0.018 | 0.022 |
| Mean | 1.87 | 316.17 | 413.60 | 264.50 | -0.15 | 0.98 | 0.13 | 438.99 | 681.46 | 442.46 | 0.715 | 0.059 | 0.231 |
| Median | 2.00 | 284.77 | 349.32 | 216.32 | 0.03 | 0.37 | 0.11 | 337.96 | 425.23 | 389.06 | 0.102 | 0.055 | 0.076 |
| Stdv. | 0.33 | 261.01 | 336.11 | 191.13 | 5.53 | 11.08 | 2.05 | 292.26 | 592.78 | 227.10 | 1.721 | 0.030 | 0.776 |

Histograms in Figure 2.8 depict correlations between shock-field angle "*THBN*", coronal magnetic field "*BMAG*", plasma density "*DENSITY*" Alfven speed "*VA*", shock speed, and shock density jump "*SHOCKJUMP*". Moderate positive correlations exist between magnetic field and density, and between magnetic field and Alfven speed, suggesting common underlying physical processes. A negative correlation between magnetic field and shock density jump implies stronger magnetic fields associate with

[6]SPREAdFAST Catalog: `https://spreadfast.astro.bas.bg/catalog/`

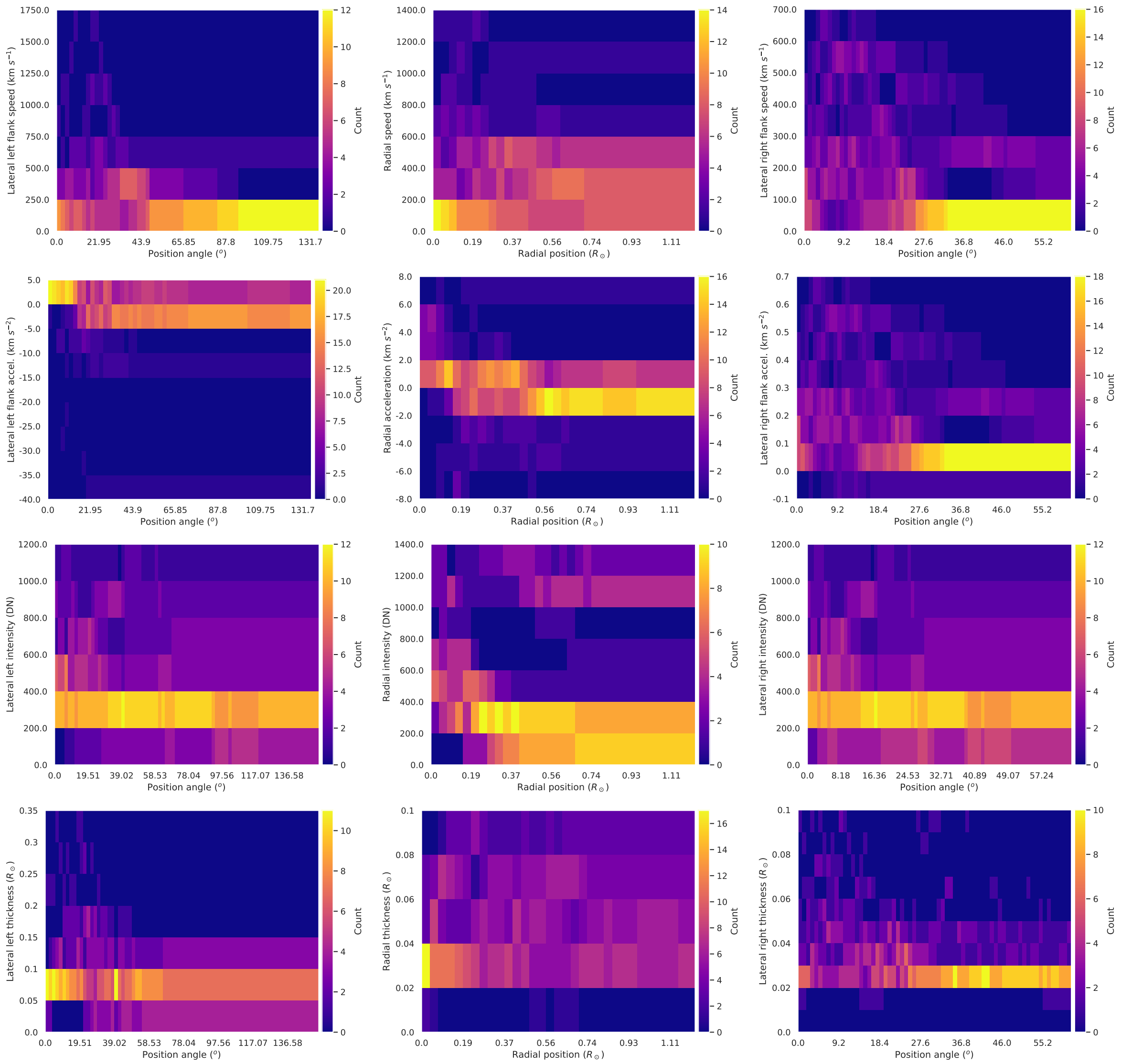

Figure 2.7: Dynamic spectra of the EUV waves kinematics in the AIA FOV. The panels from the top to the bottom are the wave speeds, acceleration, mean intensity, and thickness. The left column is for the lateral left flank, the central column is for the radial direction, and the right column is for the lateral right flank.

smaller density jumps across shock surfaces, possibly due to magnetic field pressure resisting plasma compression or faster Alfven waves mitigating density jumps. Further exploration is warranted to establish definitive connections and parameterize shock density jumps.

## 2.6 *Wavetrack*: Automated Recognition and Tracking of Solar Eruptions

### 2.6.1 Overview

The principal drivers of SEPs are acknowledged to be CME-driven shocks within the corona and interplanetary space. This acceleration primarily occurs through the diffusive shock acceleration (DSA) and shock drift acceleration (SDA) processes (Reames 2021). Efforts have focused on characterizing SEP acceleration under ideal conditions (Vainio & Laitinen 2008; Sokolov et al. 2009; Kozarev et al. 2013), with recent models incorporating observational data (Vourlidas et al. 2012; Kwon et al. 2014; Kozarev et al. 2015, 2019).

Understanding SEP acceleration requires comprehensive knowledge of CME-shock interactions with three-dimensional coronal fields (Rouillard et al. 2016). Modeling DSA necessitates deducing shock front shapes from observations, considering the impact of the local magnetic field-shock angle (Guo & Giacalone 2013). EUV imaging, facilitated by instruments like STEREO (Wuelser et al. 2004) and SDO/AIA (Lemen et al. 2012), enables shock characterization, supporting time-dependent modeling of SEP acceleration (Kozarev & Schwadron 2016; Kozarev et al. 2017, 2019). Solar feature detection, including EUV waves, employs automated techniques (Aschwanden 2010; Pérez-Suárez et al. 2011), with challenges in wave recognition and tracking (Podladchikova & Berghmans 2005; Verbeeck et al. 2014; Long et al. 2014; Ireland et al. 2019).

Wavetrack, a Python library, addresses these challenges by offering flexible solar feature detection and tracking (Stepanyuk et al. 2022). It integrates wavelet transforms and filtering, enabling multiscale data representation (Starck & Murtagh 2002) and Á trous wavelet transform (Akansu 1991; Holschneider et al. 1989), essential for tasks like CME tracking.

Various techniques contribute to solar image analysis, including wavelet transform, image filtering, feature detection algorithms, machine learning, and solar feature tracking.

- **Wavelet Transform**: The Á trous wavelet transform facilitates multi-scale data representation, aiding feature extraction in solar image analysis.
- **Image Filtering**: Various techniques enhance specific features within solar images, aiding in phenomena detection.
- **Feature Detection Algorithms**: Automated algorithms improve solar feature identification efficiency across different observations.
- **Machine Learning**: Integration of machine learning techniques such as Convolutional Neural Networks (CNNs) and Generative Adversarial Networks (GANs) enriches solar image analysis capabilities.
- **Solar Feature Tracking**: Tracking algorithms monitor feature evolution over time, crucial for understanding solar processes.

Observations from SDO/AIA, particularly in 193 and 211 $\mathring{A}$ wavelengths, are instrumental in studying solar dynamic features, facilitating CBF analysis and tracking.

### 2.6.2 Image Filtering Techniques

Image filtering techniques, including thresholding, wavelet decomposition, and segmentation, were central to the method. Initial thresholding narrowed the dynamic range of base difference images, focusing on the object of interest.

Following thresholding, the base difference images underwent Á trous wavelet decomposition into multiple scales. Each wavelet coefficient was then thresholded relative to the statistical distribution of pixel intensities at each decomposition level. Segmentation produced object masks for each time step, which were subsequently multiplied by the original data to reveal intensity variations within the object.

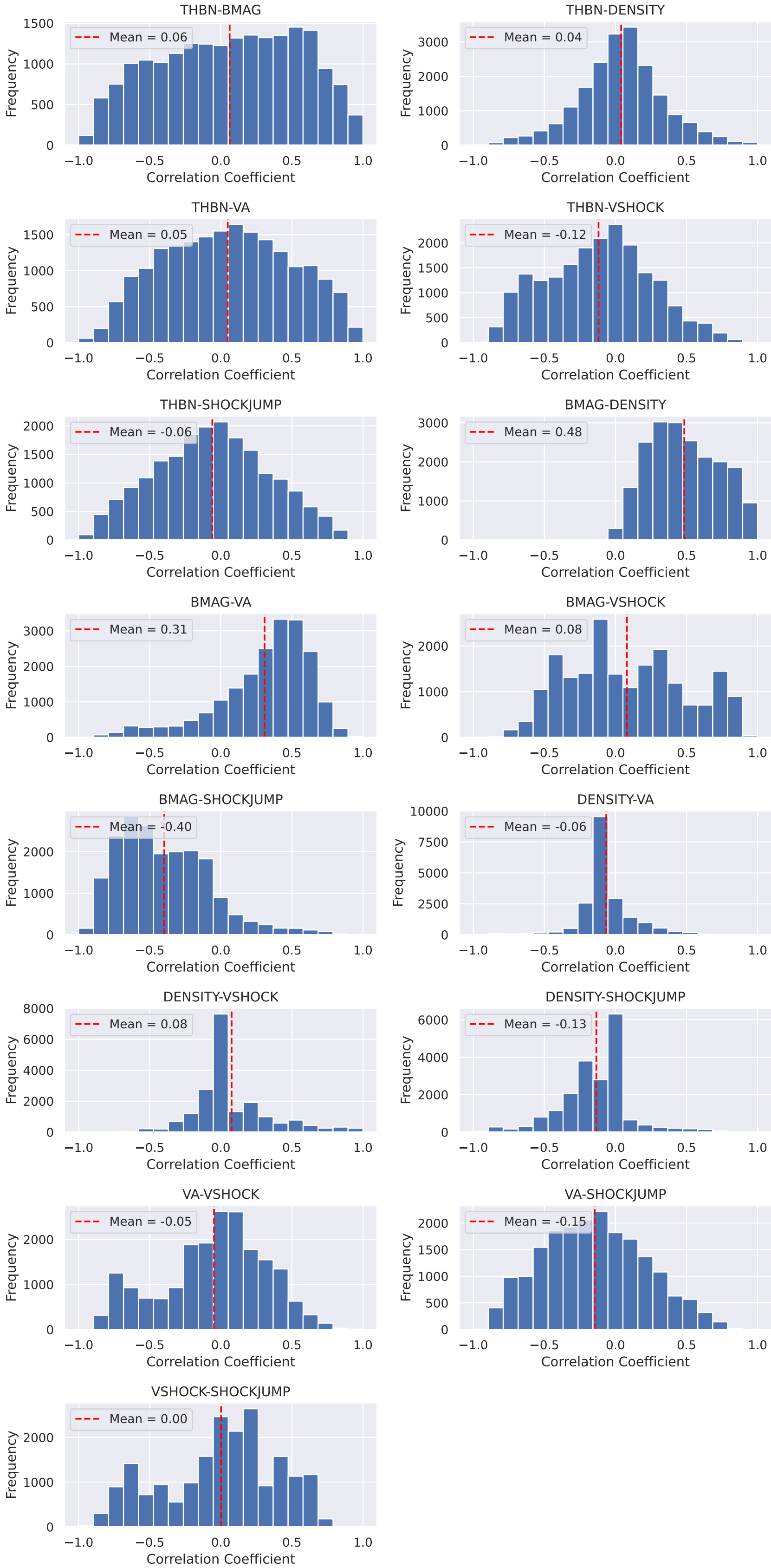


Figure 2.8: Histograms of along-field-lines model plasma parameters in the solar corona for all the 26 events. The vertical dashed red lines are the mean values.

Tailored approaches were employed due to variations in statistical distributions of pixel intensities between base and running difference images. Base difference images focused on specific segments containing the object of interest, such as a CBF, while running difference images, used for eruption initiation identification, were dependent on specific features and objects observed.

The Á trous wavelet transform, providing a multi-scale data representation, significantly contributed to solar image recognition and tracking. This hierarchical decomposition facilitated the extraction of specific objects and their masks from imaging observations, aiding in their tracking and temporal analysis. It enhanced the visibility of faint features like EUV waves, offering a versatile framework applicable to various solar phenomena across different wavelengths, thus serving as a valuable tool for analyzing CME shock waves and filaments.

The study introduced the Wavetrack package, an automated tool for detecting and tracking dynamic coronal features in solar observations. By utilizing wavelet decomposition, feature enhancement, filtering, and object recomposition, Wavetrack identified and tracked features such as CBFs and eruptive filaments. This Python framework, adaptable to both on-disk and off-limb features, facilitates tracking of features evolving over time.

### 2.6.3 Wavetrack for Coronal Wave and Filament Tracking

Wavetrack employed wavelet decomposition, feature enhancement, and filtering for tracking coronal waves. The method enhanced faint features like EUV waves using the Á trous wavelet decomposition. Automated feature recognition, including intensity thresholding and segmentation, isolated coronal wave features, generating time-dependent pixel masks for both on-disk and off-limb features.

For filament tracking, Wavetrack utilized wavelet decomposition, feature recognition, object mask generation, and image recomposition. The method identified different scales of features and enhanced them for tracking. Object masks isolated filament features at each time step, and image recomposition produced final feature maps. Image choice, such as inverted AIA 193 $\mathring{A}$ images, depended on source data and filament velocity.

### 2.6.4 Fourier Local Correlation Tracking (FLCT) Model

The study employed the FLCT model to determine solar feature velocities, utilizing the FLCT method. FLCT analyzed consecutive solar images and tracked feature motion over time using object masks from Wavetrack. The output provided detailed maps of instantaneous velocity, aiding in understanding solar feature expansion and evolution.

The study integrated advanced image processing techniques, including wavelet transform, filtering, feature detection algorithms, and machine learning, for comprehensive solar observation analysis. Wavetrack emerged as a versatile tool, particularly valuable for dynamic coronal feature tracking, offering significant insights into solar dynamics.

### 2.6.5 Results

The study showcases the versatility of the Wavetrack package through several examples:

1. **May 11, 2011 event**: Wavetrack algorithm tracked an erupting filament and its associated coronal bright front (CBF), revealing their relationship using AIA 193 $\mathring{A}$ observations.

2. **September 29, 2013 event**: Wavetrack monitored a large-scale filament eruption, consistently tracking features on the solar disk and corona.

3. **December 12, 2013 event**: Wavetrack analyzed driven and non-driven regions of a CBF, revealing its relation to eruptive features.

4. **June 07, 2011 event**: Wavetrack observed significant radial speed variations and stable angle changes during a compressive front event.

Focusing on the May 11, 2011 event accompanied by a CBF, the methodology was applied to three events observed by AIA (Kozarev et al. 2015, 2017). Wavetrack adeptly tracked CBF evolution both on the solar disk and off the limb, maintaining performance despite pixel distribution and intensity differences. The application facilitated detailed study of CBF shapes and intensity distributions, separate

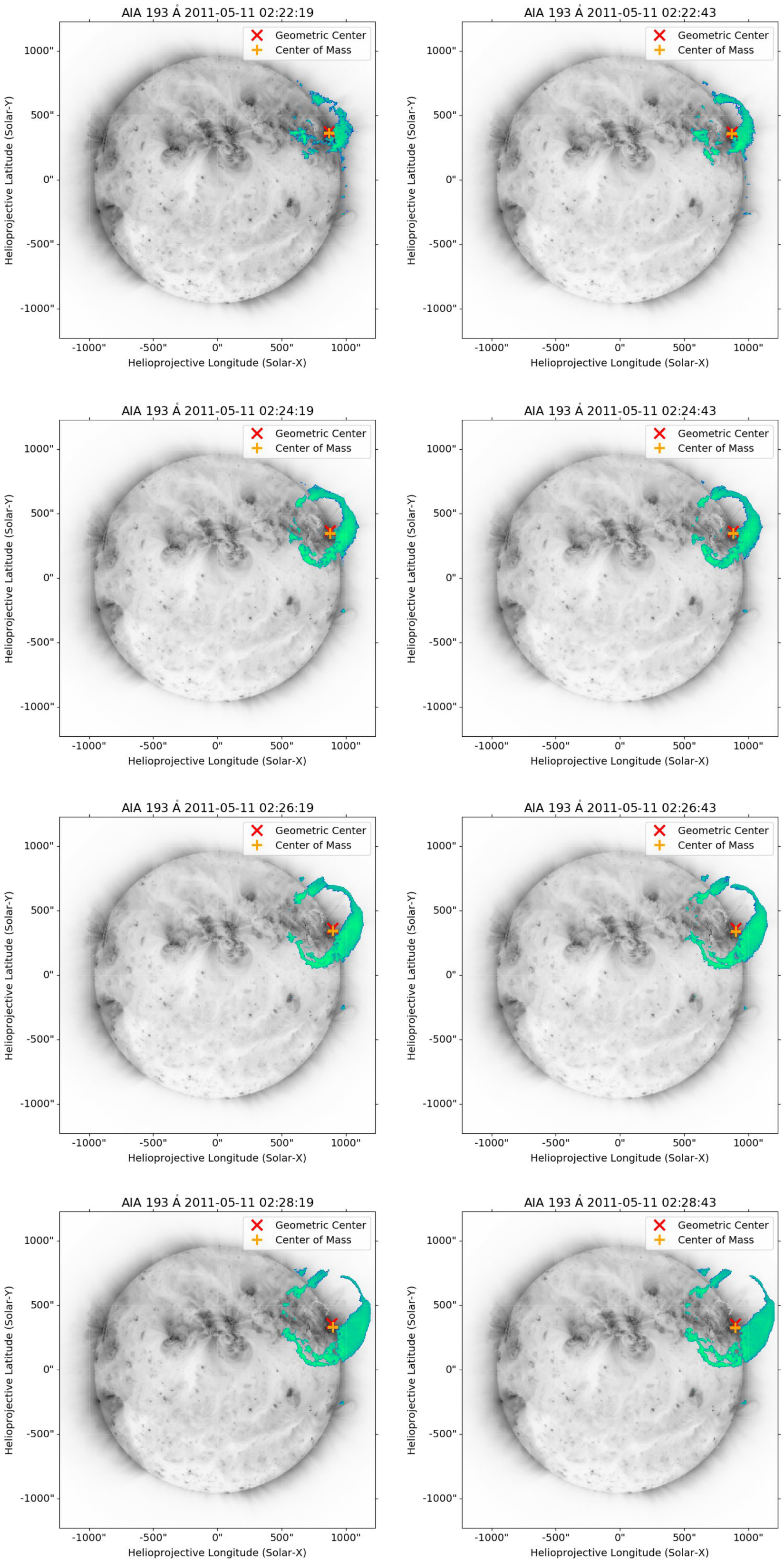


Figure 2.9: Wavetrack images of a May 11, 2011 eruption, with CBF mask applied. Four image pairs shown, separated by 2 minutes, to track CBF over time. Credit goes to Stepanyuk et al. (2022).

from the broader corona. Wavetrack effectively segmented CBF objects under different activity states, highlighting its capability to track multiple separate parts of the same feature.

Wavetrack was used to isolate and study CBF and filament kinematics using the FLCT method. Figure 2.9 shows FLCT results of the May 11, 2011 event, revealing uneven expansion of the CBF from the central source. The combined approach elucidated dynamic behavior not discernible from intensity observations alone. Figure 2.10 displays the direction and speed of each CBF region. It reveals uneven expansion, with the thinnest part, strongly driven by the erupting filament, moving fastest. This nuanced insight, inaccessible through intensity observations alone, highlights the value of our combined Wavetrack and FLCT approach in understanding coronal feature dynamics. Figure 2.11 depicts thorough analysis of CBF centers of mass (CM) and geometric centers (GC), illustrating their positional and speed variations over time. These findings provide valuable insights into CBF dynamics during the specified event.

## 2.7 Geomagnetic Storms: CME Speed De-Projection vs. In Situ Analysis

This study, led by Miteva et al. (2023), examines the relationship between geomagnetic storm (GS) intensity and solar/interplanetary phenomena. Using the *PyThea* framework, we reconstruct 3D geometry of geo-effective CMEs and compare on-sky and de-projected speed values, employing spheroid, ellipsoid, and graduated cylindrical shell (GCS) models. We investigate parameters of GS-associated phenomena, finding that fast CME speeds combined with specific magnetic structure orientations are indicative of GS strength. Accurate estimations of geometry, direction, and de-projected speeds are crucial for GS forecasting in space weather prediction schemes.

### 2.7.1 Overview

Solar eruptive events such as CMEs and solar flares (SFs) influence space weather, with electromagnetic radiation preceding energetic particles and CME plasma clouds (Fletcher et al. 2011; Webb & Howard 2012; Klein & Dalla 2017; Temmer 2021; Malandraki & Crosby 2018; Gopalswamy 2022). Geomagnetic storms (GSs) occur due to interactions between solar wind plasma and Earth's magnetosphere, facilitated by magnetic reconnection during events like CME impacts (Dungey 1961; Akasofu 1981; Echer & Gonzalez 2022; Gonzalez et al. 1994; Saiz et al. 2013; Lakhina & Tsurutani 2016). Fast CMEs cause intense GSs, affecting technology and inducing disruptions in near-Earth space (Tsurutani et al. 1997; Zhang et al. 2007; Wu & Lepping 2016; Borovsky & Denton 2006; Pulkkinen 2007).

However, single spacecraft observations limit accurate CME speed estimations due to projection effects (Paouris et al. 2021; Kouloumvakos et al. 2022). Previous studies found no clear correlation between GS intensity and solar flare/CME parameters (Samwel & Miteva 2023), highlighting the need for reliable early warnings based on solar or near-Sun measurements. Accurate prediction of CME impact on Earth requires understanding their directionality and geometry, crucial for maximizing forecast lead time (Kay & Gopalswamy 2018; Vourlidas et al. 2003; Jackson et al. 2010).

Improving reconstruction techniques to correct projection effects enhances CME propagation understanding and forecasting (Thernisien et al. 2009; Mierla et al. 2010; Wood et al. 2010; Thernisien 2011). Existing CME propagation models exhibit discrepancies between 2D and 3D speeds and widths (Odstrcil et al. 2004; Xie et al. 2004; Vršnak et al. 2013; Pomoell & Poedts 2018; Jang et al. 2016; Verbeke et al. 2022). This study focuses on deducing CME directionality and near-Sun speeds using the PyThea framework (Kouloumvakos et al. 2022), analyzing geo-effective cycle 24 CMEs and their correlations with GS intensity and interplanetary parameters.

The event selection process identified 25 significant GSs within Solar Cycle 24 (SC24) and associated them with potential IP and/or solar phenomena. This involved temporal associations with IP and ICME events, CMEs, and solar flares. Various databases and catalogs were utilized for this analysis (Gonzalez et al. 1994; Gopalswamy et al. 2022b; Qiu et al. 2022; Besliu-Ionescu et al. 2022; Abe et al. 2023; Zhang et al. 2007; González et al. 2007; Gopalswamy et al. 2008; Echer et al. 2013; Manu et al. 2022).

Utilized databases and catalogs include the GS database Kyoto[7], SF database (GOES)[8], CME catalog

[7] `https://wdc.kugi.kyoto-u.ac.jp/dstdir/index.html`
[8] `http://ftp.swpc.noaa.gov/pub/warehouse/`

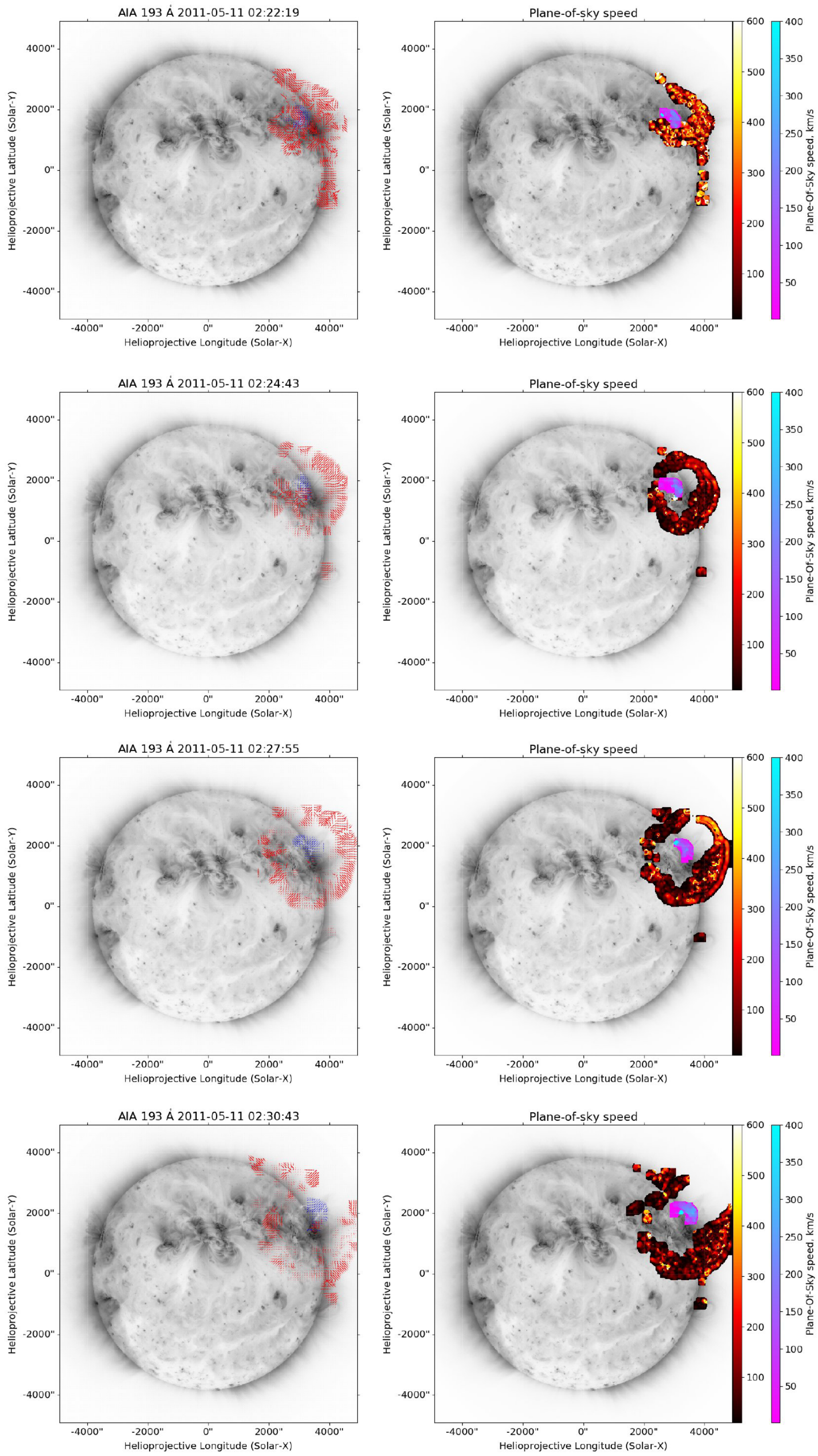


Figure 2.10: FLCT model output for four image pairs from Fig. 3. Left: the plane-of-sky velocity vectors. Right: plane-of-sky speed. Credit goes to Stepanyuk et al. (2022).

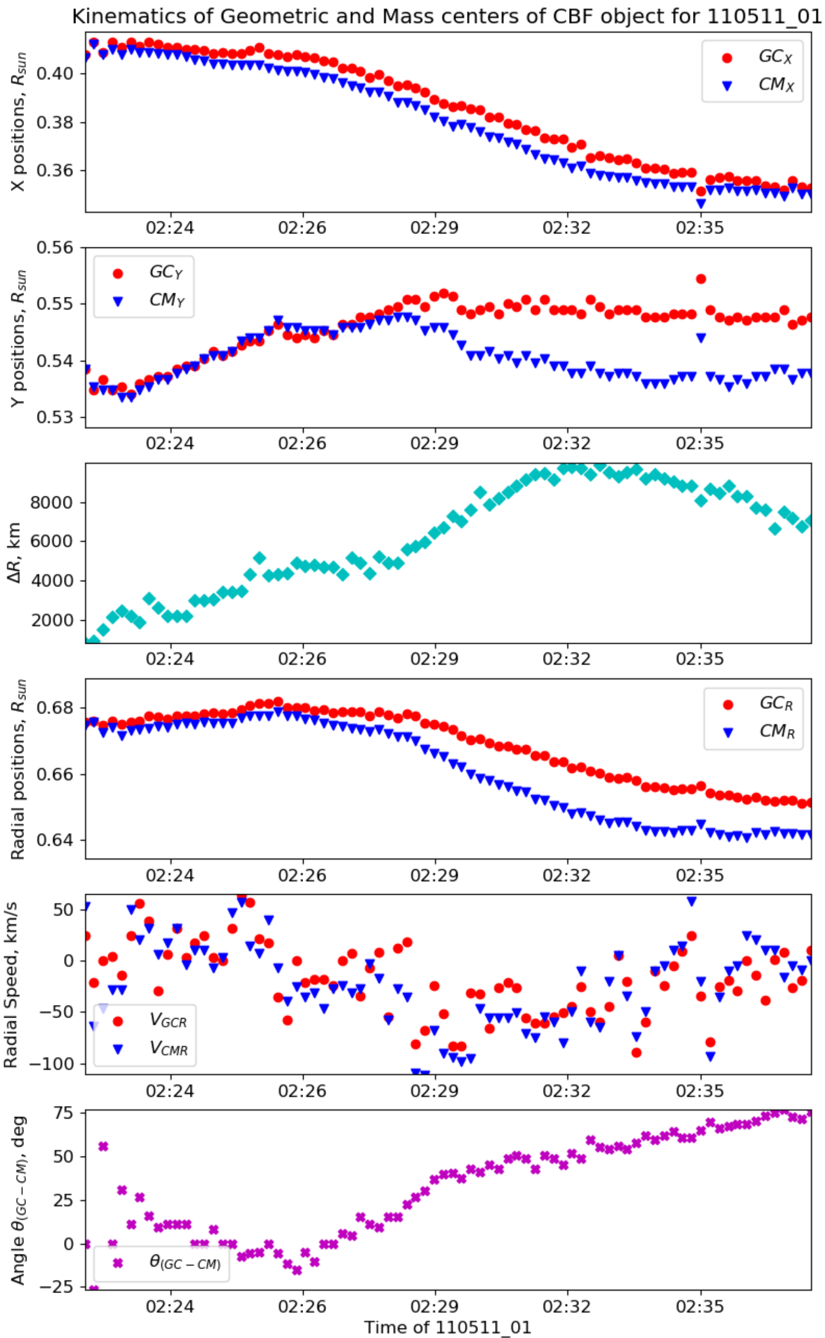


Figure 2.11: Analysis of the center of mass and geometric centers' motion during the May 11, 2011 event. The different rows present the X-, Y-, and R- positions for both GC and CM, the distance between GC and CM in *km*, and the angle between these two points over time. Credit goes to Stepanyuk et al. (2022).

(SOHO-LASCO)[9], ICME Wind and ACE databases[10],[11], and IP shock database (Wind)[12],[13]. These resources were accessed for relevant data retrieval and analysis (Selvakumaran et al. 2016).

### 2.7.2 PyThea 3D De-Projection Tool

This investigation employs the PyThea online tool for 3D reconstruction of CMEs and shock waves (Kouloumvakos et al. 2022), utilizing spheroid, ellipsoid, and GCS models. Two independent observers conduct fitting procedures. Figure 2.12 illustrates fits for event E03, revealing observer bias in structure alignment with the model, potentially leading to CME width overestimation. However, despite this bias, overall results for event E03, including directivity and speed, remain minimally impacted, though discrepancies may arise among different observers.

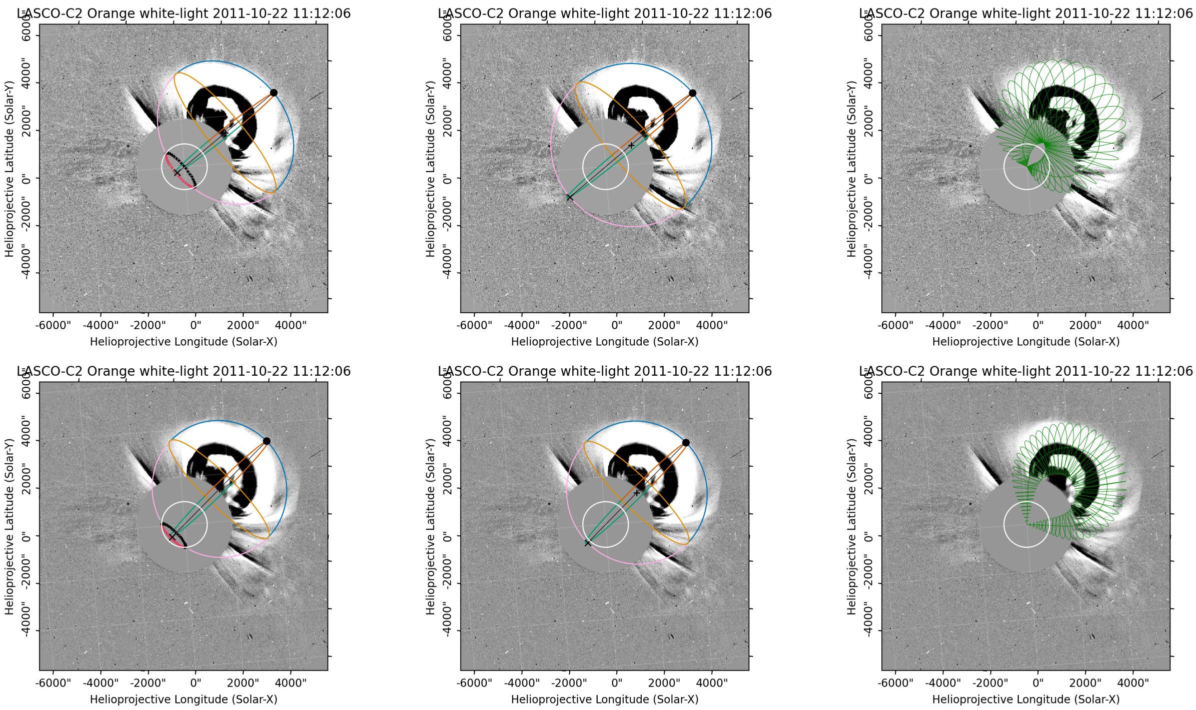


Figure 2.12: 3D reconstructions of a CME (E03) using the spheroid, ellipsoid, and GCS model from the PyThea tool performed by observers 1 and 2 (top and bottom row, respectively). Credit goes to Miteva et al. (2023).

In five cases (E05, E11, E17, E18, E22), attempts to identify SFs or CMEs were unsuccessful, while in six additional cases, SF specifications were unattainable. Events with uncertain CME origins were excluded from subsequent 3D analyses. For example, the unique orientation of a double CME in case E07 rendered its de-projection unfeasible, leading to its exclusion. Similarly, in seven cases (E12, E14–E16, E19, E23, E25), data retrieval issues from both spacecraft led to their omission from 3D analyses.

The study focuses on deriving de-projected CME speeds based on fits at two distinct time steps. Initial CME longitude and latitude are manually specified for each model, utilizing provided SF locations. Final CME directivity is considered relatively crude, derived from qualitative information extracted from available animations[14]. This approach ensures a rigorous basis for evaluating de-projected CME speeds.

[9]LASCO CME Catalog: `https://cdaw.gsfc.nasa.gov/CME_list/`
[10]`https://wind.nasa.gov/ICME_catalog/ICME_catalog_viewer.php`
[11]`https://izw1.caltech.edu/ACE/ASC/DATA/level3/icmetable2.htm`
[12]`http://www.ipshocks.fi/database`
[13]`https://lweb.cfa.harvard.edu/shocks/wi_data/`
[14]`http://helioweather.net/archive/`

### 2.7.3 Results

**Projection Effects**

Approximately 10 CMEs were analyzed by two designated observers in our research team, including myself, utilizing all three models in the PyThea framework. The fitting process involved two time steps to derive velocity parameters based on height–time estimations. Both observers conducted the 3D de-projection procedure iteratively for each event, resulting in averaged CME speeds presented in Table 2.5, rounded to the nearest tenth. Discrepancies between fitting instances were treated as errors, ranging from 10 $km\,s^{-1}$ to twice the estimated speed. Figure 2.13 illustrates the correlation between 3D speeds and estimated errors, showing significant variability, particularly with the GCS model, but a discernible positive trend between error magnitude and CME speed.

Subjectivity and varied experience levels among observers influenced the visual fitting process, leading to differences in evaluated speeds, both within individual observers using the same model and across different models for a single observer. Variations in operating system software also contributed to result discrepancies. Events E04, E08, and E21 were incomplete due to PyThea computing issues or substantial uncertainty in CME structure assessment.

Our findings highlight the inherent subjectivity in procedures relying on personal judgment for fit quality, detailed further in (Verbeke et al. 2022). Averaged CME speeds, meticulously outlined in Table 2.5, will serve as the basis for subsequent correlation studies.

Table 2.5: CME Speeds ( $km\,s^{-1}$ ) for Observers 1 and 2. Credit goes to Miteva et al. (2023).

| # | **Spheroid** | | **Ellipsoid** | | **GCS** | |
|---|---|---|---|---|---|---|
| | **obs1** | **obs2** | **obs1** | **obs2** | **obs1** | **obs2** |
| E01 | $2170 \pm 870$ | $1800 \pm 270$ | $2130 \pm 200$ | $1710 \pm 450$ | $1590 \pm 100$ | $1760 \pm 10$ |
| E02 | $1780 \pm 140$ | $1350 \pm 50$ | $1880 \pm 580$ | $1310 \pm 90$ | $1780 \pm 260$ | $1630 \pm 130$ |
| E03 | $770 \pm 40$ | $740 \pm 10$ | $640 \pm 180$ | $740 \pm 180$ | $1020 \pm 170$ | $700 \pm 270$ |
| E04 | - | $2150 \pm 140$ | - | $2460 \pm 70$ | - | $2530 \pm 630$ |
| E06 | $1410 \pm 420$ | $710 \pm 70$ | $1870 \pm 50$ | $1700 \pm 300$ | $1680 \pm 870$ | $1560 \pm 470$ |
| E08 | $350 \pm 90$ | - | $360 \pm 150$ | - | $350 \pm 70$ | - |
| E09 | $690 \pm 280$ | $630 \pm 150$ | $550 \pm 170$ | $590 \pm 60$ | $670 \pm 610$ | $710 \pm 220$ |
| E10 | $840 \pm 380$ | $610 \pm 1040$ | $1120 \pm 360$ | $960 \pm 90$ | $1160 \pm 650$ | $1310 \pm 80$ |
| E13 | $320 \pm 90$ | $350 \pm 50$ | $620 \pm 140$ | $750 \pm 160$ | $780 \pm 80$ | $1310 \pm 700$ |
| E20 | $830 \pm 190$ | $800 \pm 600$ | $790 \pm 90$ | $570 \pm 20$ | $1240 \pm 280$ | $1130 \pm 230$ |
| E21 | $620 \pm 230$ | - | $440 \pm 40$ | - | $280 \pm 180$ | - |
| E24 | $750 \pm 270$ | $1310 \pm 220$ | $880 \pm 350$ | $2020 \pm 960$ | $950 \pm 120$ | $1560 \pm 540$ |

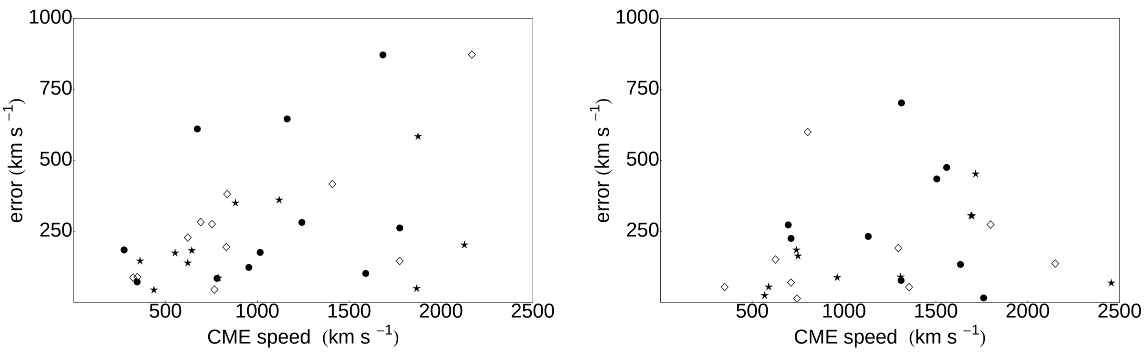


Figure 2.13: Scatter plot illustrates the comparison of 3D de-projected CME speeds derived from the spheroid model (depicted as diamonds), the ellipsoid model (represented by stars), and the GCS model (indicated as dots) versus the measurement errors for observers 1 (left) and 2 (right). Credit goes to Miteva et al. (2023).

### Correlation between GSs, Coronal, and Near-Sun Parameters

Figure 2.14 shows a scatter plot illustrating the relationship between the modulus of the GS Dst index and CME speed. Averaged results of three model fits (*3D-mean*) are compared with 2D SOHO-LASCO CME speeds in Table 2.6, alongside error estimates from 3D de-projections. Despite some overlap, the largest error value among observers (as outlined in Table 2.5) is highlighted for clarity.

Analysis reveals no discernible trend between the Dst index and CME speed, regardless of considering 3D de-projections or 2D CME speeds. Data constraints prevented 3D speed de-projections for the most robust GSs, skewing speed distribution and impacting findings. Despite the modest sample size (10 to 20 event pairs), Pearson correlations assess fit quality. Coefficients in Table 2.6 range from negligible (e.g., 0.04 for 2D LASCO speeds) to moderate (highest: 0.55 with GCS model). Notably, no significant correlations are found between Dst index and other coronal parameters (e.g., SF class, location, CME AW), as comprehensively presented in the same table.

Table 2.6: Table displaying Pearson correlation coefficients among the GS Dst index, CME speed, and various solar parameters, with the respective sample sizes indicated in parentheses. Credit goes to Miteva et al. (2023).

| **CME source** | **Dst−speed** | **solar parameter** | **Dst−solar parameter** |
|---|---|---|---|
| LASCO | 0.04 (20) | SF class | −0.04 (14) |
| **3D - mean** | **0.49 (12)** | SF latitude | −0.16 (14) |
| 3D spheroid - mean | 0.34 (12) | SF longitude | 0.13 (14) |
| 3D spheroid - obs1 | 0.14 (11) | CME AW | 0.03 (20) |
| 3D spheroid - obs2 | 0.15 (10) | | |
| 3D ellipsoid - mean | 0.53 (12) | | |
| 3D ellipsoid - obs1 | 0.28 (11) | | |
| 3D ellipsoid - obs2 | 0.40 (10) | | |
| 3D GCS - mean | 0.55 (12) | | |
| 3D GCS - obs1 | 0.49 (11) | | |
| 3D GCS - obs2 | 0.27 (10) | | |

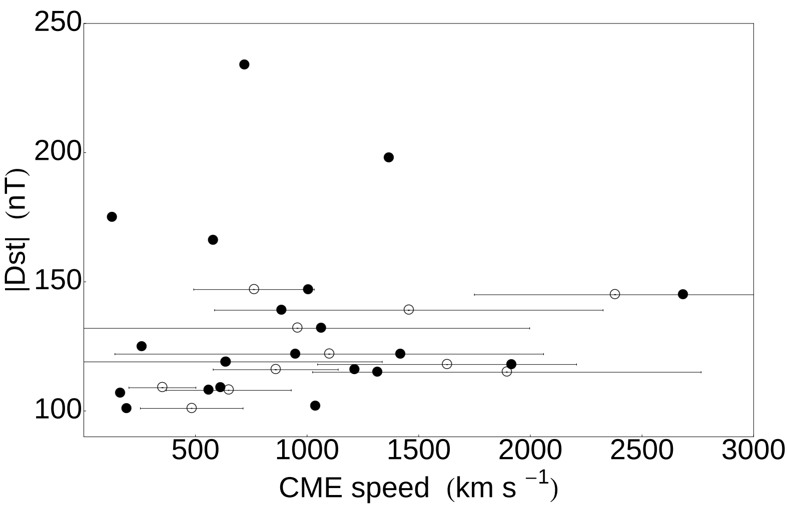


Figure 2.14: Scatter plot illustrating the relationship between the Dst index and CME speed, incorporating data from the SOHO/LASCO instrument (represented by filled circles) and 3D de-projections (depicted by empty circles). Credit goes to Miteva et al. (2023).

### Correlation between GSs and IP Parameters

We explore correlations between GSs and various parameters linked to pre-selected IP phenomena. Scatter plots illustrate relationships such as Dst index versus ICME speed and IP shock speed, Dst

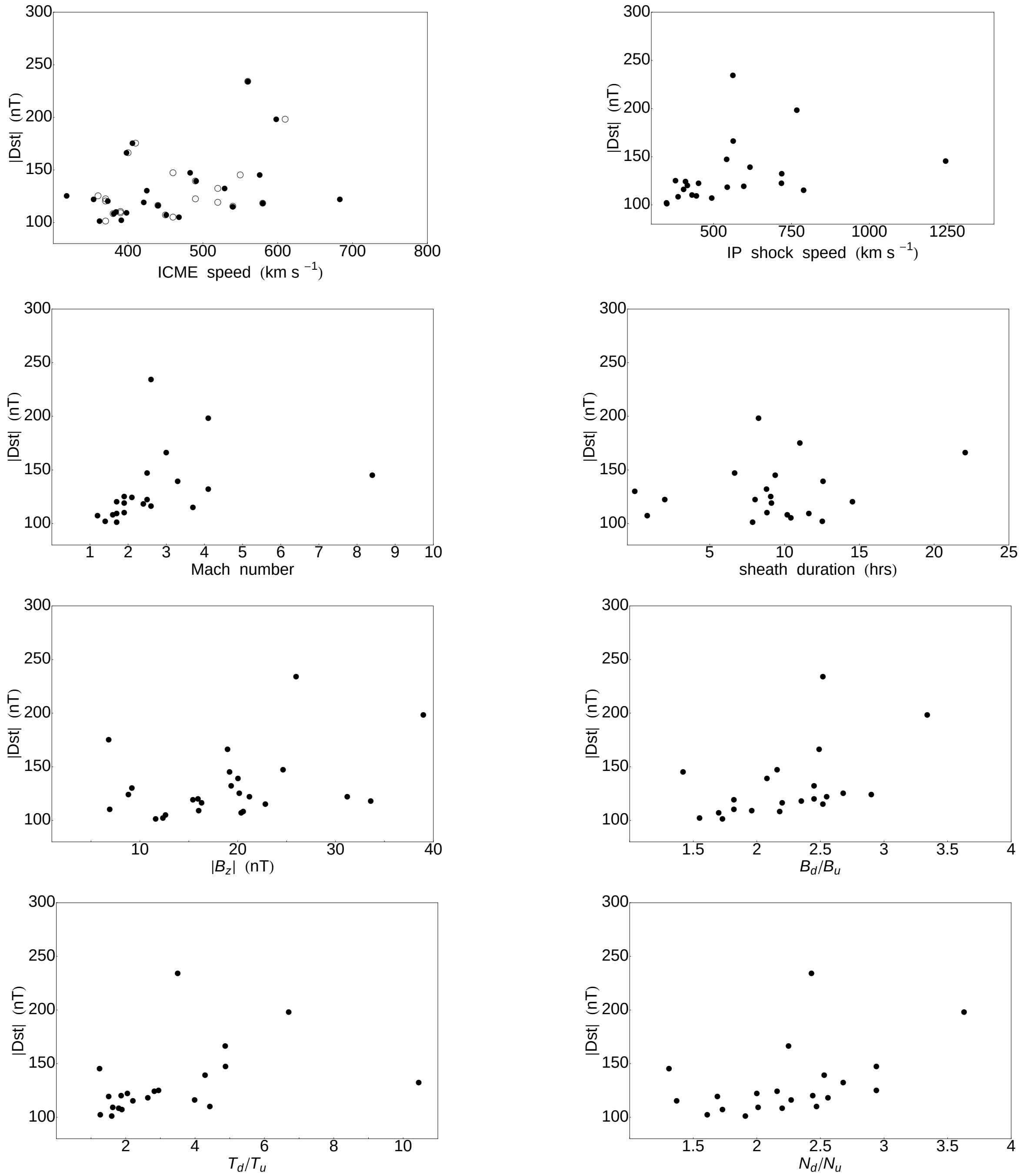


Figure 2.15: Comprehensive scatter plots illustrating the relationships between Dst index and various solar wind parameters, including Wind/ACE ICME speed, IP shock speed, Mach number, duration of sheath region, Bz, magnetic field jump, temperature jump, and density jump. Credit goes to Miteva et al. (2023).

Table 2.7: Tabular representation of Pearson correlation coefficients between the GS Dst index and various parameters of IP phenomena. The data is derived from Wind satellite measurements, unless otherwise stated, with the corresponding sample sizes indicated in parentheses. Credit goes to Miteva et al. (2023).

| **IP parameter** | **Dst−IP parameter** |
|---|---|
| ICME speed | 0.37 (24) |
| ICME speed (ACE) | 0.44 (22) |
| IP shock speed | 0.35 (22) |
| Mach number | 0.36 (21) |
| sheath duration | 0.22 (20) |
| $\|B_z\|$ | 0.37 (25) |
| $B_d/B_u$ | 0.48 (21) |
| $T_d/T_u$ | 0.40 (21) |
| $N_d/N_u$ | 0.46 (21) |
| $B$ | **−0.14 (20)** |
| $V$ | **0.19 (20)** |
| $\beta_u$ | **−0.14 (21)** |

versus Mach number and sheath duration, and Dst versus $|Bz|$ and $B_d/B_u$. Figure 2.15 and Table 2.7 detail these correlations.

For the limited sample used, we observe moderately positive trends between Dst index and plasma compression parameters at the shock interface, comparable to or slightly larger than correlations with ICME speeds. However, the trend with $|Bz|$ is weaker (0.37), contrasting with robust trends from prior studies. Correlations involving Dst and IP shock speed, Mach number, or sheath duration are relatively smaller.

Recent reports suggest strong correlations with electric and magnetic field components (Echer & Gonzalez 2022), although this exceeds our current analysis scope. Caution is warranted in interpreting results due to lack of uncertainty estimates for correlation coefficients. Additional parameters from ICME and IP shock catalogs show no robust correlations with Dst index, all correlation coefficients being smaller than 0.2.

**Forecasting GS Strength Based on Solar and IP Parameters**

We examine how magnetic obstacle type, orientation upon Earth arrival, and 3D reconstructed CME speeds collectively impact GS intensity, approximated by the Dst index.

The most potent GSs in our compilation exhibit distinctive magnetic structure parameters, including complexity, orientation, and speed at Earth. Exceptions include instances of fast speed flank hits or uncertain configurations, possibly influenced by fast solar wind streams or CIRs. Notably, IP structure associated with certain GSs has notably low speeds.

Interpretation considers information from both speed reconstructions and in situ measurements to enhance analysis robustness.

## 2.8 Discussion

The May 11, 2011 eruption showcased a variety of solar phenomena, including a fast partial-halo CME, a weak solar flare, an eruptive filament, and a type II radio burst. Analyzing the interplay of these events offers insights into solar and interplanetary dynamics.

### 2.8.1 CME Kinematics and Coronal Shock Wave Characteristics

The CME exhibited characteristics such as a linear speed of 745 $km\, s^{-1}$, an acceleration of 3.3 m s$^{-2}$, and an angular width of 225$^o$. The associated shock wave displayed complex kinematics, observed in both the low and middle/outer corona.

In the low corona, the shock wave's asymmetry and evolving geometry revealed dynamic behavior. Differences in thickness, speed, and acceleration between flanks suggested complex interactions with the coronal environment. Segmenting the shock surface highlighted variations in shock characteristics.

In the middle/outer corona, SOHO/LASCO measurements depicted the dynamic evolution of the EUV wave. Gallagher model fitting emphasized the importance of combining AIA and LASCO measurements. Fluctuations in acceleration and speed underscored the shock wave's complexity.

Statistical analysis revealed patterns in coronal wave events, with radial waves exhibiting distinct characteristics compared to lateral waves. Cumulative dynamic spectra illustrated trends in shock speed and intensity with distance.

Correlations between plasma parameters and shock characteristics were identified, laying the groundwork for further parameterizations in subsequent phases of the project.

### 2.8.2 Dynamic Coronal Features Analysis with Wavetrack

Stepanyuk et al. (2022) utilized Wavetrack to study eruptive solar events, focusing on the May 11, 2011 event associated with a significant CBF. Two additional events, on June 7, 2011, and December 12, 2013, were also examined, demonstrating Wavetrack's versatility in tracking various solar features.

Wavetrack efficiently delineated evolving CBFs across consecutive time steps, even with variations in pixel distributions and intensities. This enabled detailed exploration of time-dependent shapes and intensity distributions, distinct from the broader corona. Segmentation during the December 12, 2013 event highlighted Wavetrack's effectiveness in tracking multiple parts of the same feature.

To analyze CBF and filament kinematics, the FLCT method was employed. Results revealed the plane-of-sky direction and speed of different CBF regions during the May 11, 2011 event. The study showcased the complementary nature of Wavetrack and FLCT in elucidating dynamic behavior.

The study calculated plane-of-sky speeds of the erupting filament driver (Fig. 2.10), showing higher speeds directly below the region of highest speeds in the CBF. Geometric centers and centers of mass were determined, providing insights into the dynamics of the solar eruption event.

These findings offer insights into the dynamics and characteristics of the May 11, 2011 solar eruption event, particularly regarding the movement and speeds of key features like the CBF and erupting filament driver.

### 2.8.3 Subjectivity in CME Speed Determination

Our study on CMEs reveals significant variability due to subjectivity in fitting and de-projection procedures. Analysis of approximately 10 CMEs using PyThea framework models highlights observer disparities and technical limitations. Averaged CME speeds, documented in Table 2.5, show associated errors emphasizing the challenges and uncertainties in this process.

Despite subjectivity challenges, these averaged values form the basis for correlation studies. Correlating GSs with parameters like the Dst index and CME speeds reveals no discernible trend, with Pearson correlation coefficients indicating diverse relationships.

Scatter plots in Figure 2.15 and Table 2.7 show moderately positive correlations between the Dst index and plasma compression parameters at the shock interface. However, caution is warranted due to the absence of uncertainty estimates for correlation coefficients.

Further analysis of magnetic obstacle characteristics and 3D CME speeds sheds light on patterns influencing GS intensity. Nose-like orientation and complex or flux-rope structures characterize the most potent GSs. Limitations in single-point IP shock speed measurements underscore the need for comprehensive interpretation considering both speed reconstructions and in situ measurements.

## 2.9 Conclusions

I conducted a study characterizing 26 historical CME-driven CBFs in the low solar corona, observed with the AIA instrument onboard the SDO spacecraft. Utilizing the SPREAdFAST framework, we integrated physics-based and data-driven models to estimate coronal magnetic fields, shock wave dynamics, energetic particle acceleration, and SEP propagation. The analysis relied on AIA base-difference images to generate annulus plots and J-maps for kinematic measurements in radial and lateral directions.

Various time-dependent and distance-dependent kinematic parameters were computed, including shock speed, acceleration, intensity, and thickness. LASCO measurements up to $17R_{\odot}$ were incorporated to improve SEP spectra characterization. Kinematic measurements facilitated time-dependent 3D geometric models of wavefronts and informed plasma diagnostics through MHD and DEM models.

Shock kinematic measurements were used to fit geometric spheroid surface models for each time step, capturing shock characteristics accurately. Parametrized relationships between plasma parameters were explored to identify connections and interdependencies.

In Stepanyuk et al. (2022), we present Wavetrack, an innovative method for automated identification and monitoring of dynamic coronal phenomena. By employing wavelet decomposition, feature enhancement, and filtering, Wavetrack generates time-dependent masks for feature pixels, particularly adept at tracing faint, large-scale features like coronal bright fronts (CBFs) and EUV waves. Operable for on-disk and off-limb features, Wavetrack is implemented as a versatile Python framework.

Application to four events, focusing on CBFs in May 11 and June 07, 2011, and December 12, 2013, demonstrates Wavetrack's proficiency in tracking complete CBF pixel maps. Integrating with the FLCT method reveals the dynamic evolution of CBF regions and their correlation with eruptive filament drivers, highlighting compression effects and speed variations.

Wavetrack also tracks temporal changes in feature regions by computing time-dependent vectors between pixel geometric centers and centers of mass, providing valuable metrics for feature evolution. However, manual segmentation and parameter fine-tuning are currently required, with plans for future improvements to enhance versatility.

The methodology shows promise for broader application across solar dynamic features and datasets, with future research extending its use to filament evolution and coronagraph data analysis, refining our understanding of eruptive front variations across different observational contexts.

Our findings in Kozarev et al. (2022) and Stepanyuk et al. (2022) contribute to understanding shock kinematics and plasma parameters. Future investigations will focus on SEP acceleration near the Sun and transport of coronal and interplanetary particles, refining shock and coronal parameter characterization methods for enhanced accuracy and reliability.

In Miteva et al. (2023), we analyze geo-effective storms during solar cycle 24 to identify predictors for storm intensity. Our approach integrates solar, near-Sun, and interplanetary parameters, incorporating results from PyThea, a tool for CME speed de-projection. We find improvements in correlation coefficients for projected CME speed, although fast CMEs pose challenges due to reconstruction errors and structural complexity.

Fast halo CMEs exhibit significant deviations, affecting reconstruction quality and limiting forecasting potential for storm strength. In contrast, certain interplanetary parameters, particularly ICME and IP shock speeds, show moderate positive correlations with storm intensity. However, discrepancies in measurements and single-point observations raise concerns about predictive capability.

Among various parameters, the combination of speed and orientation of the magnetic obstacle appears influential, as seen qualitatively in the *helioweather* animations. While de-projected CME speeds enhance modeling accuracy, they do not directly impact storm intensity. Permanent stereoscopic observations, like the ESA Vigil mission, are crucial for improved 3D reconstructions of CME geometries and accurate speed estimations.

In conclusion, our study lays the groundwork for ongoing projects aimed at refining parameterizations and integrating synoptic MHD parameters into the *S3M* synoptic model, enhancing our understanding of solar dynamics and space weather forecasting.

Our findings highlight the importance of integrating advanced tracking methodologies like Wavetrack with kinematic analyses such as FLCT, providing deeper insights into the complexities of eruptive solar events. As we refine these methodologies, our understanding of solar phenomena will advance, contributing to Heliophysics.

Furthermore, our study emphasizes the complexity of studying CMEs and their impact on geomagnetic storms. Integrating observational data and model outputs offers a comprehensive perspective for further investigations into the dynamic interplay between solar and interplanetary phenomena in shaping space weather events.

# Chapter 3

# Solar Radio Observations

## Integrating Data for Coronal Diagnostics

In this chapter, I focus on multi-wavelength observations of solar type III radio bursts and modeling studies of plasma parameters and coronal magnetic fields to understand solar radio emission mechanisms during quiet times and coronal conditions influencing burst propagation. Initially, I introduce type III radio bursts and detail the data used, followed by output presentation and interpretation.

## 3.1 Introduction

Type III radio bursts result from energetic electron beams injected into the solar corona, propagating along IMF lines Ergun et al. (1998); Pick (2006); Reid (2020). These beams trigger plasma waves, transformed into radio emission at local plasma frequency or its harmonics Melrose (2017). They manifest as intense emissions drifting in frequency over seconds to minutes, detectable across a wide frequency range Wild & McCready (1950); Lecacheux et al. (1989); Bonnin et al. (2008), offering insight into solar active phenomena Reid & Ratcliffe (2014); Kontar et al. (2017).

Electron beams persist well beyond 1 AU, providing in situ insights into burst and ambient heliospheric conditions, including electron density, beam speed, and Langmuir wave detection Dulk et al. (1985); Boudjada et al. (2020); Gurnett & Anderson (1976, 1977); Reid & Ratcliffe (2014). Combining ground-based and space-borne observations is crucial for comprehensive analysis.

This work studies type III bursts on April 3, 2019, using data from LOFAR van Haarlem et al. (2013) and PSP Fox et al. (2016), integrating PFSS and MAS models Altschuler & Newkirk (1969); Schatten et al. (1969); Mikić et al. (1999). LOFAR imaging provides burst source localization, expanding knowledge of electron beam triggers and coronal conditions. Understanding these aspects is crucial for comprehending solar energetic particles, solar wind, and their effects on near-Earth space.

Previous studies have investigated type III burst mechanisms Chen et al. (2013); Bonnin et al. (2008); Reiner et al. (2009); Saint-Hilaire et al. (2012); Morosan & Gallagher (2017); Pulupa et al. (2020); Krupar et al. (2020); Cattell et al. (2021); Harra et al. (2021); Badman et al. (2022). Modern instruments like LOFAR and PSP offer enhanced sensitivity, yet challenges remain, including electron acceleration mechanisms and discrepancies between observations and models.

The chapter is structured as follows: Section 3.2 describes LOFAR and PSP observations of type III bursts; Section 3.3 explains data analysis and modeling techniques; Section 3.4 presents analysis results, investigating physical mechanisms and comparing with solar corona models; and Section 3.5 summarizes findings and discusses implications.

## 3.2 Observations

Several studies have investigated solar radio emissions during the PSP's second encounter in late 2019 Krupar et al. (2020); Pulupa et al. (2020); Cattell et al. (2021); Harra et al. (2021); Badman et al. (2022). This study focuses on type III radio bursts occurring on April 3, 2019, between approximately 12:10 and 12:50 UT, coinciding with active regions AR12737 and AR12738. AR12737, on the near side of the Sun, exhibited a $\beta$ magnetic configuration with eight sunspots Hale et al. (1919), while detailed observations of AR12738 were unattainable due to its far-side position.

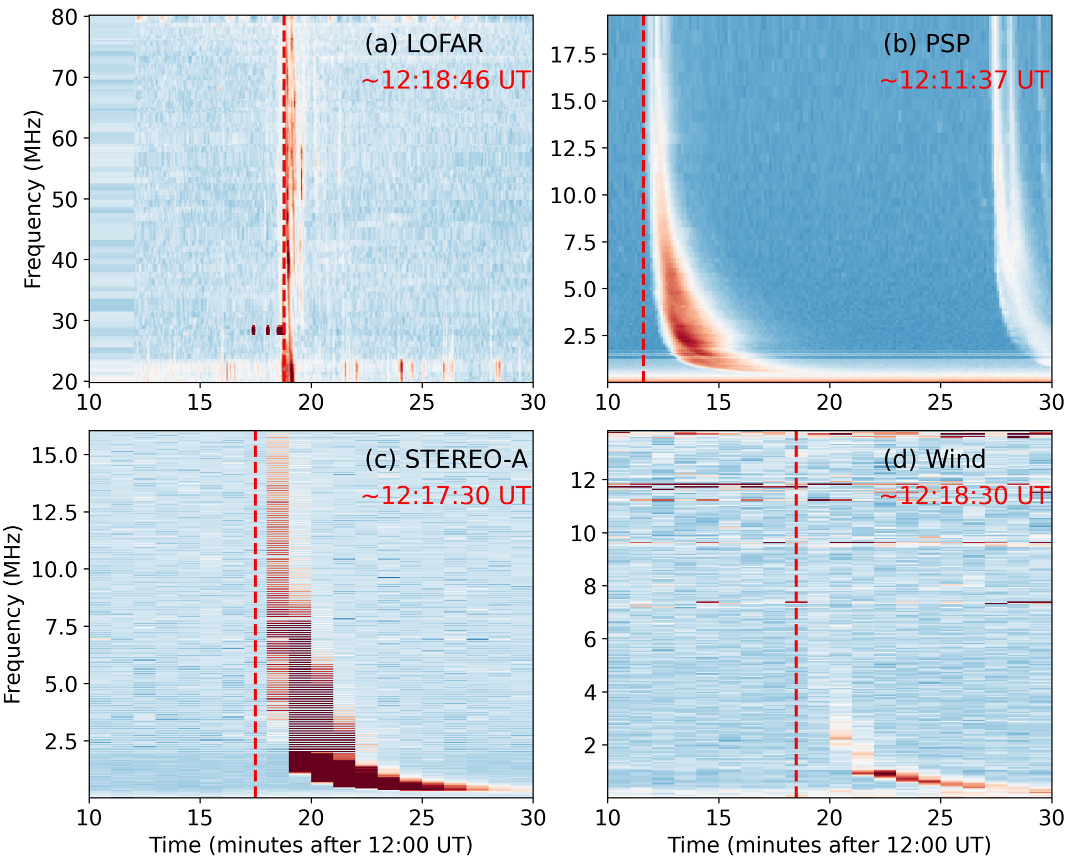


Figure 3.1: Radio dynamic spectra for a single burst obtained from multiple instruments. The top-left panel is from the LOFAR/LBA instrument, the top-right is from the PSP/FIELDS instrument, the bottom-left is from the STEREO/SWAVES instrument, and the bottom-right is from the Wind/WAVES. The vertical red dashed line denotes the start time of the burst.

Intense type III radio bursts were observed by four instruments (Wind/WAVES, PSP/FIELDS, STEREO-A/SWAVES, and LOFAR/LBA) during a regular survey. Figure 3.1 displays the first type III burst observed by these instruments, with the start time determined using the second derivative of the light curve at specific frequency channels. The relative orientations of the instruments with respect to Earth are shown in Figure 3.2, with PSP and STEREO spacecraft almost aligned with the Sun. The solar disk appeared quiet, with no X-ray or EUV transient emissions during the study period, confirmed by GOES-15/XRS and SDO/EVE observations. Despite this, the sensitive LOFAR telescope detected bursts close to noon, corroborated by PSP data.

Localized regions of relatively higher intensity, likely small-scale coronal brightening spots or campfires, were observed in EUVI and AIA images Young et al. (2018); Madjarska (2019); Berghmans et al. (2021). Subsequent subsections introduce the PSP and LOFAR instruments and their observations of the radio bursts.

### 3.2.1 PSP Observations

Parker Solar Probe (PSP) is a spacecraft launched in 2018 to study solar corona and solar wind (Fox et al. 2016). I utilized level-2 data from the FIELDS instrument suite (Bale et al. 2016; Pulupa et al. 2017), available in CDF format on the PSP FIELDS data products website[1]. Data values were converted from $V^2/Hz$ to $dB$ units using a threshold of $10^{-16}$ $V^2/Hz$ for radio burst detection (Pulupa et al. 2020). High- and Low-Frequency Receiver data were combined into a single dynamic spectrum covering 10.5 kHz to 19.2 MHz, with noise minimized through subtraction of mean intensity values.

[1] PSP FIELDS data products: `http://research.ssl.berkeley.edu/data/psp/data/sci/fields/`

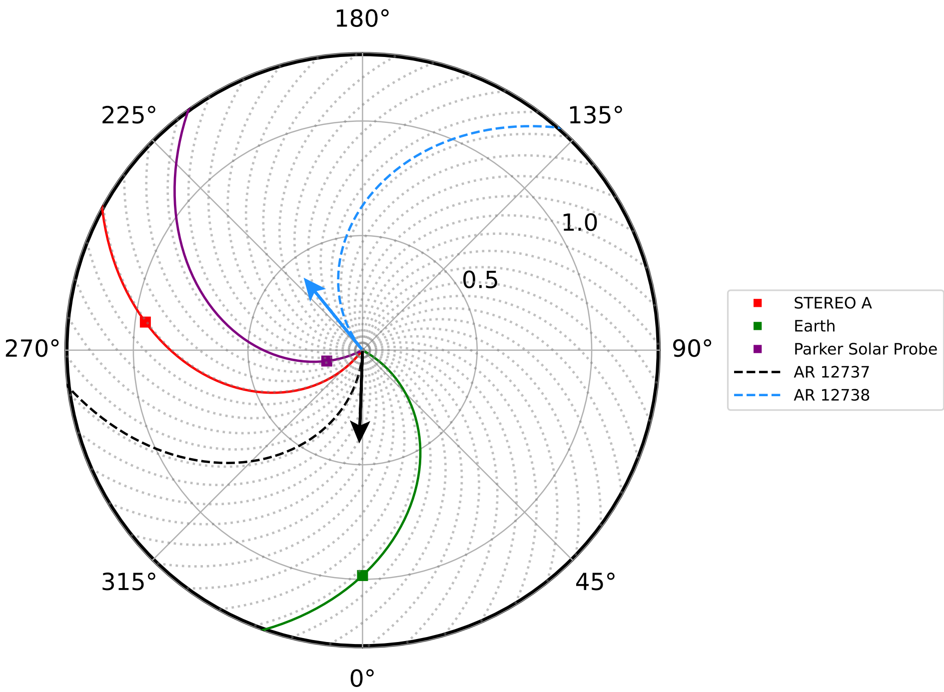


Figure 3.2: Top view of the spacecraft positions in the ecliptic plane at 12:15 UT on April 3, 2019, with the Sun-Earth line as the reference point for longitude. The Earth's location is representative of the positions of LOFAR, Wind/WAVES, and GOES-15/XRS instruments. The spacecraft were connected back to the Sun by a 400 km/s reference Parker Spiral. The black arrow represents the longitude of AR12737 and the blue arrow represents the longitude of the AR12738. The gray dotted lines are the background Parker spiral field lines. The black dashed spiral shows the field line connected to the AR12737, and the blue dashed spiral is connected to the AR12738. The figure is generated using the Solar MAgnetic Connection Haus (Solar-MACH) tool (Gieseler et al. 2023).

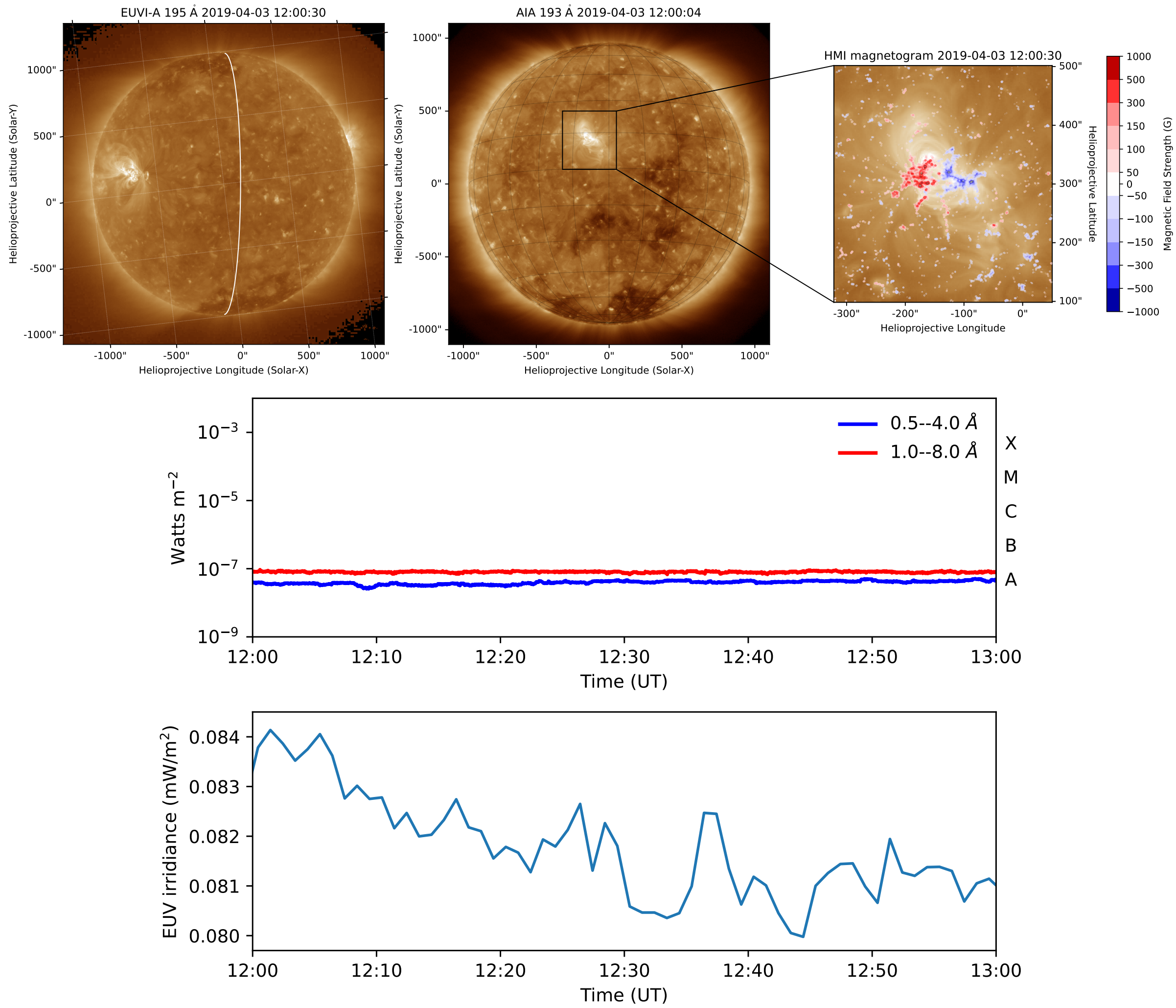


Figure 3.3: Exploring the X-ray and extreme ultraviolet (EUV) emissions from the Sun. The top panel showcases a cutout region of the SDO/AIA 193 Åimage of the solar disk along with the STEREO-A EUVI 195 Åpoint of view. The white curve is the limb of the solar disk as seen by AIA from the right side. The red and blue colors are the contours of the line-of-sight magnetogram from the SDO/HMI instrument. The levels are (50, 100, 150, 300, 500, 1000) Gauss. The middle panel shows the X-ray flux from the GOES-14 spacecraft shows minimum activity. The bottom panel shows the time series of the ESP Quad band from the SDO/EVE instrument, which shows the solar irradiance in the extreme ultraviolet (EUV) band.

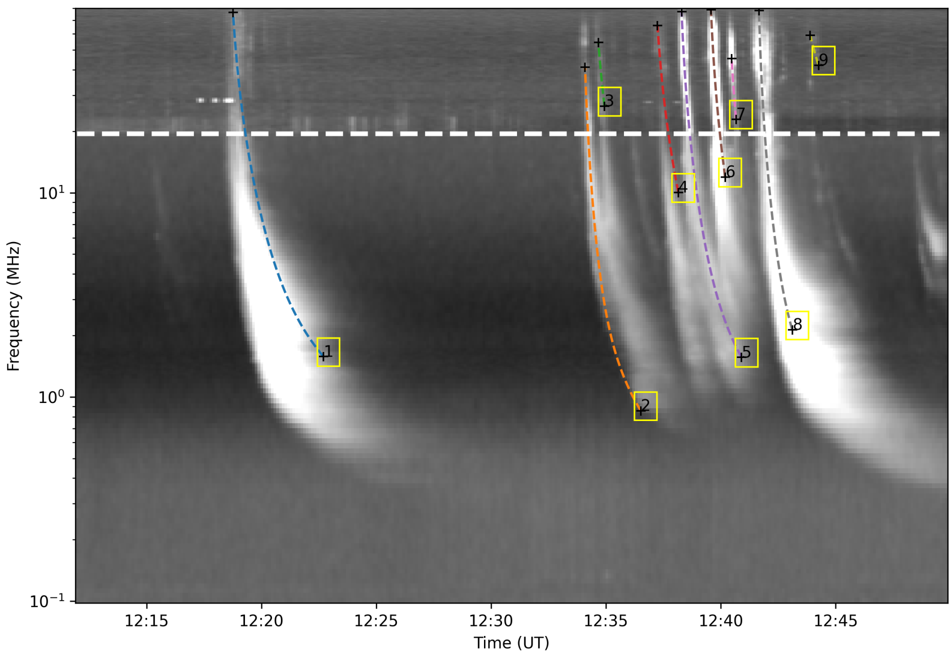


Figure 3.4: Automatic detection of type III radio bursts from the combined radio dynamic spectrum of LOFAR and PSP instruments. The dashed horizontal lines separates the LOFAR frequency range (top) and the PSP frequency range (bottom).

### 3.2.2 LOFAR Observations

The LOw Frequency ARray (LOFAR) telescope (van Haarlem et al. 2013) observes the Sun at frequencies between 10 and 240 MHz. Dynamic spectrum data from the Low-Band Antenna (LBA) were obtained from the LOFAR long-term archive[2]. Background subtraction and Gaussian smoothing were applied to clean the spectrum. PSP and LOFAR spectra were combined, considering the travel time difference of radio signals from the Sun to each instrument. LOFAR data were down-sampled to match PSP's 7-second cadence. The resulting combined spectrum is shown in Figure 3.4. LOFAR's LBA frequency ranges between 19.82 and 80.16 MHz, while PSP's cover 10.55 kHz to 19.17 MHz.

To automatically detect type III radio bursts in the combined dynamic spectrum, I applied the algorithm proposed by Zhang et al. (2018), which employs probabilistic Hough transformation to detect vertical bright edges within a specified deviation angle from the vertical direction.

## 3.3 Methods

### 3.3.1 Imaging of Radio Sources

I developed an automated pipeline to preprocess and calibrate LOFAR interferometric data for solar radio imaging (Zhang et al. 2022a). Burst detection was performed using the algorithm by Zhang et al. (2018) on combined LOFAR and PSP dynamic spectra (Fig. 3.4). The Parker electron-density model (Parker 1960) was employed to map bursts to radial distances, with least-squares fitting used to derive frequency drifts and electron beam speeds.

Subsequently, burst detection was repeated on LOFAR dynamic spectra alone (Fig. 3.5) to identify $(f, t)$ pairs for each burst. Snapshot frequencies were selected for interferometric imaging, calibrated using Tau-A observations. The WSClean algorithm (Offringa et al. 2014) was applied to obtain cleaned images of radio sources at the chosen frequencies.

Persistence imaging was employed to enhance image clarity and information content (Thompson & Young 2016). This method compares pixel values across a time-ordered series of images, retaining the brightest values to create a persistent display.

To determine type III source locations in 3D space, LOFAR observations were combined with modeling. Grids of footpoints were constructed on GONG magnetogram data around active regions AR12737

[2]LOFAR LTA: `https://lta.lofar.eu/`

Table 3.1: Characteristics of the type III bursts detected via the automatic algorithm from the combined spectrum.

| Burst ID | Start Time (UT) | End Time (UT) | Start Frequency (MHz) | End Frequency (MHz) | Frequency Drift (MHz $s^{-1}$) | Beam Speed (c) |
|---|---|---|---|---|---|---|
| 1 | 12:18:45 | 12:22:42 | 76.44 | 1.57 | 0.892 | 0.044 |
| 2 | 12:34:05 | 12:36:31 | 41.24 | 0.86 | 0.241 | 0.119 |
| 3 | 12:34:40 | 12:34:56 | 54.44 | 26.54 | 3.992 | 0.046 |
| 4 | 12:37:14 | 12:38:09 | 66.03 | 10.02 | 4.006 | 0.046 |
| 5 | 12:38:17 | 12:40:54 | 76.92 | 1.57 | 0.77 | 0.066 |
| 6 | 12:39:34 | 12:40:11 | 78.86 | 11.93 | 3.192 | 0.062 |
| 7 | 12:40:28 | 12:40:40 | 45.34 | 22.9 | 3.21 | 0.067 |
| 8 | 12:41:39 | 12:43:06 | 78.21 | 2.13 | 1.555 | 0.093 |
| 9 | 12:43:53 | 12:44:15 | 59.07 | 42.13 | 2.424 | 0.013 |

and AR12738. Pfsspy package (Stansby et al. 2020) traced coronal magnetic field lines, aiding in estimating source radii and 3D positions. Radial distances of sources from the Sun were determined assuming harmonic emission, considering Newkirk electron-density models (Newkirk 1961, 1967). Deprojection of type III sources was performed to estimate their 3D positions relative to Earth's line of sight (LOS) (Fig. 3.7). Axes translations between LOFAR images and 3D space were accounted for. Detailed explanations and equations are provided in Appendices A.1 and A.2.

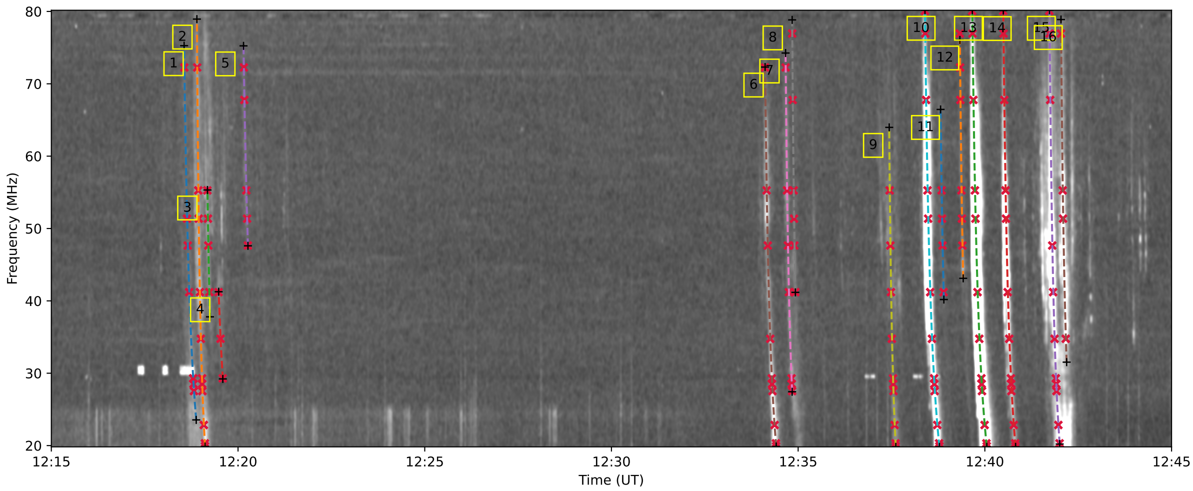


Figure 3.5: Automatic detection of type III bursts observed by LOFAR. The red symbols along the fit lines are the $(f, t)$ coordinates of the image snapshots shown in Figure 3.6.

### 3.3.2 Modeling

To analyze the coronal plasma environment during the events, I utilized standard coronal solutions from MHD simulations by Predictive Science Inc. (PSI) based on the MAS code (Mikić et al. 1999). The PSI MAS coronal solution for April 3, 2019, at 12:00 UT was obtained from the PSI data archive. Initially, I determined the angle between the burst's radial vector and the line of sight (LOS), as well as the complement angle representing the separation between the radial vector and the Earth's perspective. Using the complement angle, I derived the Carrington longitude to extract a longitudinal segment from the MAS datacube, treating it as if it were in the plane of the sky (POS). Longitudinal slices were extracted using the psipy python package. The FORWARD model, responsible for generating synthetic coronal maps, was then applied to the selected data slice. In Figure 3.8, the first radio contour of the sixth type III burst is overlaid on 2D maps of plasma parameters. These parameters include plasma density, temperature, magnetic field strength, plasma beta parameter, total plasma pressure, and Alfven speed. Estimates of local plasma conditions at the centroids' coordinates of type III sources for each frequency band are illustrated in Figure 3.9 for the sixth type III burst.

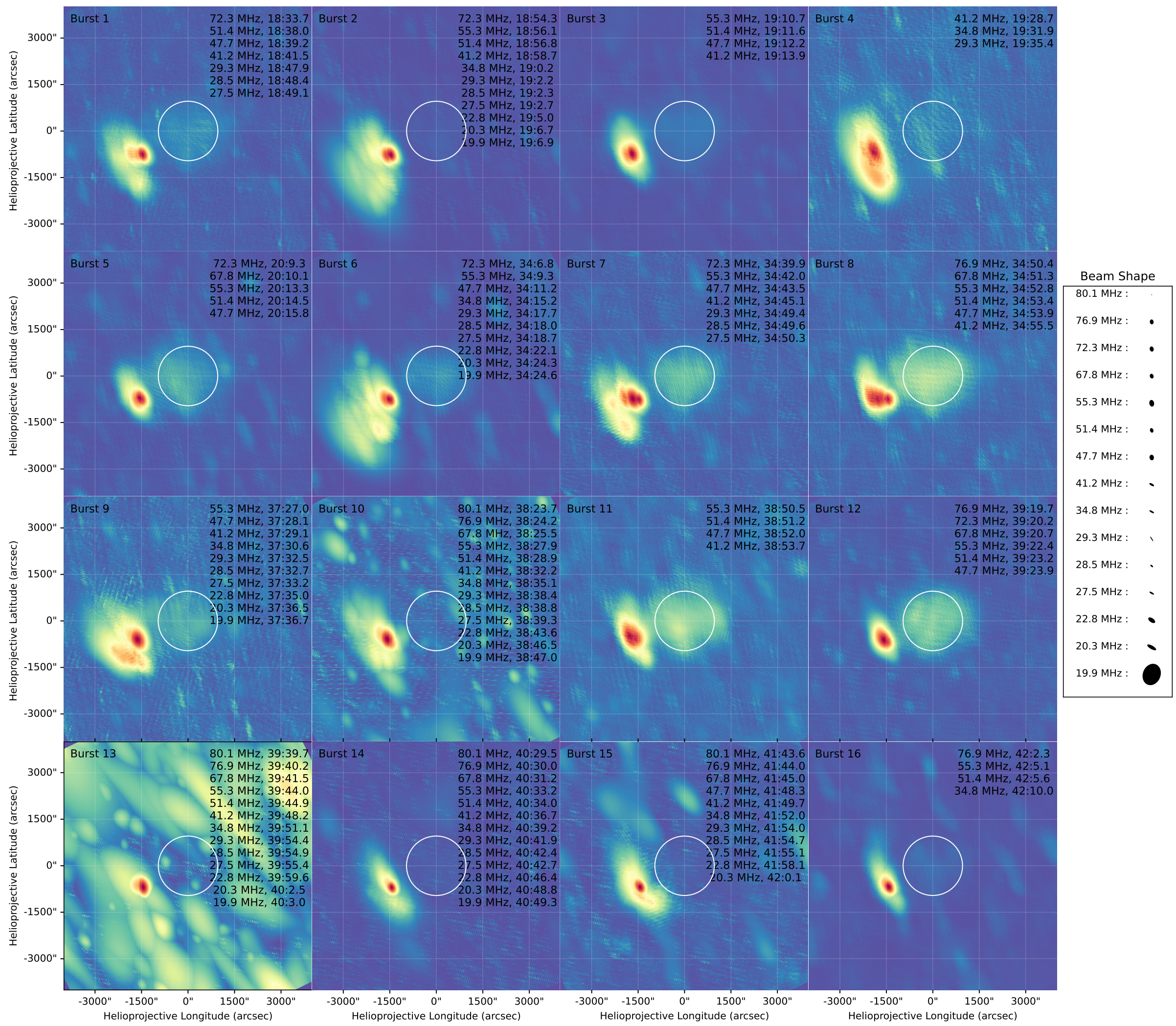

Figure 3.6: Persistence imaging for the 16 type III bursts detected in the LOFAR dynamic spectrum. The label shows the observation frequencies in MHz and times in (minutes:seconds from 12:00:00 UT). Here, the color coding is not absolute, but rather each panel has its own color code.

## 3.4 Results and discussion

### 3.4.1 Type III Radio Burst Detection and Characterization

Radio waves arrived at STEREO one minute before reaching Wind (Fig. 3.1). However, due to the close proximity to the Sun, the difference in arrival times is within the resolution of the observations, making it inconclusive which spacecraft detected the emission first.

The combined dynamic spectrum from LOFAR and PSP (Fig. 3.4) showed limitations in detecting type III bursts compared to LOFAR alone, possibly due to frequency drift and dispersion challenges. Nine bursts were captured from the combined spectrum, while 16 were traced in LOFAR alone (Table 3.1).

### 3.4.2 Imaging of Radio Emission Sources

Persistence imaging of the 16 type III bursts from LOFAR (Fig. 3.6) suggested a common origin in the south-east quadrant of the solar disk, despite the absence of an active region at that precise location. A 3D projection of radio source contours onto the coronal magnetic field (Fig. 3.7) revealed a south-eastward propagation relative to Earth's perspective. The radio sources aligned with closed field lines in the southern hemisphere and open field lines from the southern coronal hole. However, limitations exist due to outdated magnetic data for AR12738.

The potential origins of type III radio emissions include closed-field lines structures, electron beams from open-field active regions, or from corona acceleration due to magnetic field expansion in active regions. Furthermore, an inverse relationship between imaging quality and solar radio emission brightness was noted, attributed to calibration solution inaccuracies caused by solar emission leakage into calibrator beam side lobes.

### 3.4.3 Plasma Diagnostics and Magnetic Field Analysis

The alignment of radio sources (Fig. 3.7) with a streamer-like structure near the equator indicates elevated plasma beta, reduced coronal temperature, and diminished Alfven speed. However, the coronal plasma density appeared homogeneous with no prominent structures due to model resolution limitations. Radio sources for all bursts were found in the same quadrant from Earth's perspective, confined between the equatorial sheet and the southern coronal hole and moving along that boundary.

Variability of coronal plasma quantities at radio sources' centroids was observed (Fig. 3.9), with coronal temperature increasing with radial distance. Additionally, the behavior of coronal magnetic field, plasma total dynamic pressure, and Alfven speed decreased over distance. Plasma beta parameter sharply increased around 40 MHz, suggesting dominance of plasma pressure over magnetic pressure at that distance from the Sun.

Comparison of density profiles (Fig. 3.9) indicated significant differences between MAS and FORWARD modeling results compared to the 2.5×Newkirk density model and theoretical expectations. The discrepancy, even after accounting for enhancement factors, suggests possible scattering effects or stealth CMEs affecting density observations, highlighting limitations in current modeling and suggesting the need for additional physics to characterize density distribution accurately.

## 3.5 Summary and conclusions

In this study (Nedal et al. 2023b), a series of 16 type III bursts observed on April 3, 2019, during the PSP's near-Sun encounter, were analyzed using PSP/FIELDS and LOFAR. These bursts, spanning nearly 20 minutes, occurred amidst relative solar quietness with a dominant active region on the solar disk. A semi-automated pipeline aligned PSP and LOFAR observations, facilitating analysis of burst characteristics like frequency drift and electron beam speeds, suggesting their interrelation.

Interferometric imaging revealed a single source for these bursts in the solar corona's southeast limb. Various potential origins for the bursts were discussed, including impulsive events (Ishikawa et al. 2017; Che 2018; Chhabra et al. 2021), plasma upflows (Harra et al. 2021), and magnetic reconnection (Gopalswamy et al. 2022a). Magnetic extrapolation indicated no open potential field lines to active regions AR12737 or AR12738, consistent with prior findings.

Integration of burst source location with magnetic modeling suggested discrepancies, possibly due to scattering effects. Scattering and propagation effects were found significant, impacting burst location

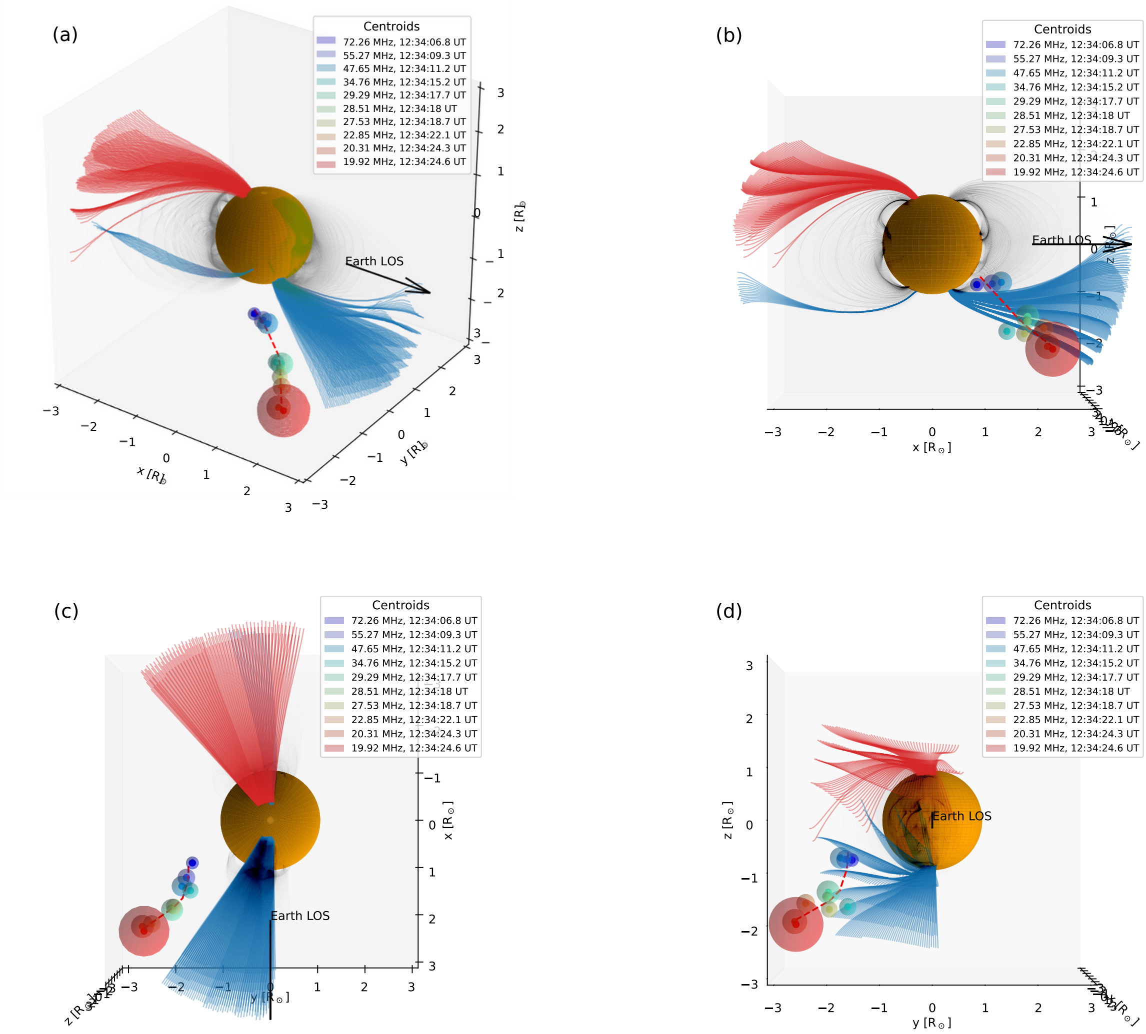


Figure 3.7: Different viewing angles for the deprojection of the radio sources of the sixth burst using the 2.5×Newkirk electron-density model on the PFSS solution. The black arrow points toward the Earth's LOS. The $yz$ plane is the POS as seen from the Earth. The red dashed line is a spline curve fit for the sources' centroids. The red, black, and blue curves are the open northern, closed, and open southern field lines, respectively. The opacity of the closed field lines is decreased for better visualization.

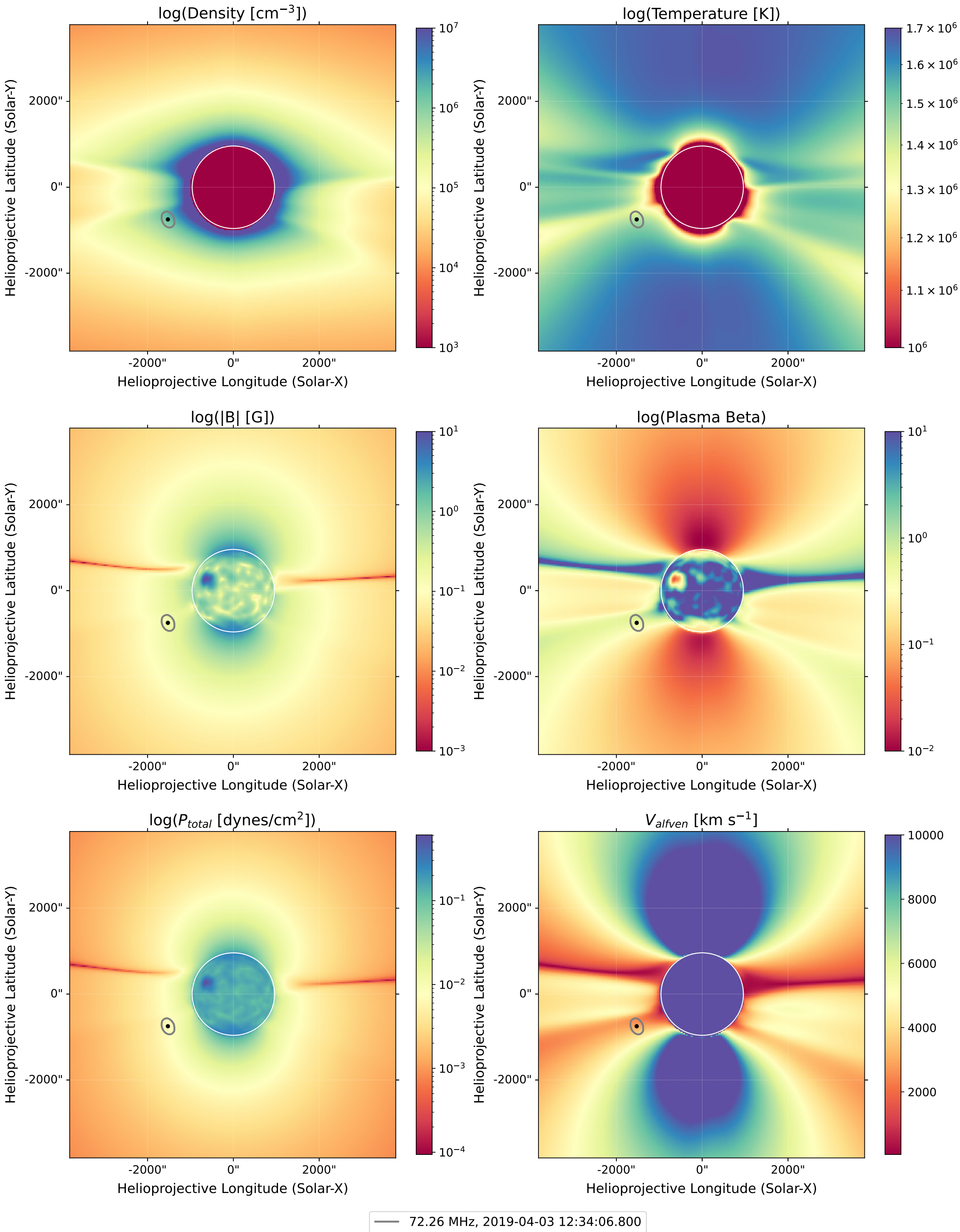


Figure 3.8: Synthesized maps of plasma parameters obtained using the FORWARD toolset, with the 70%-contour of radio emission of the sixth burst at the first timestamp (12:34:06.8 UT) at the frequency of 72.26 MHz depicted on top of the 2D POS cuts. The left column represents, from top to bottom, plasma density, magnetic field, and the total plasma dynamic pressure. The right column represents, from top to bottom, the temperature, plasma beta, and the Alfven speed.

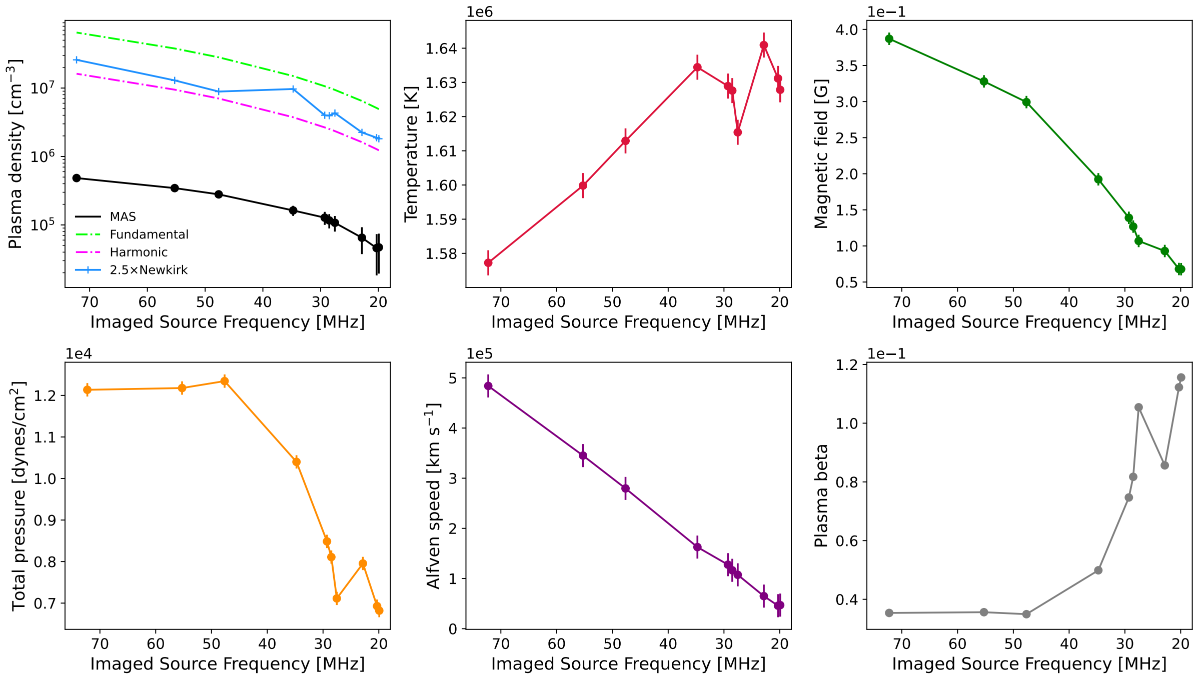


Figure 3.9: Coronal plasma parameters sampled from the 2D maps by the source centroids. The top panel shows (from left to right) the plasma density profiles from the MAS model, 2.5×Newkirk model, and the theoretical densities under the fundamental and harmonic assumptions, plasma temperature, and magnetic field. The bottom panel shows, from left to right, the total plasma dynamic pressure, Alfven speed, and plasma beta. The x-axis is inverted to demonstrate a progression of increasing radial distance from the Sun as the observer moves towards the right.

determination. Future investigations, including the TDoA technique and Solar Orbiter observations, were proposed.

The study highlighted LOFAR's efficacy in characterizing solar eruptive events and quiet periods, with implications for space weather monitoring. Future work aims to automate burst analysis and investigate their relation to solar surface activity. Additionally, analysis using LOFAR imaging and MAS modeling indicated discrepancies between observed and modeled burst trajectories, emphasizing the need for model refinements.

Overall, this study underscores the importance of considering scattering effects and refining models to enhance understanding of solar radio emissions' propagation in the corona (Kontar et al. 2019, 2023; Chen et al. 2023).

# Chapter 4

# Modeling and Forecasting of Solar Energetic Protons

This chapter has two parts. In the first part, I describe a modeling study that we conducted on energetic proton acceleration and propagation from the solar corona to 1 AU. For this modeling, we employ the physics-based approach utilized in the first chapter, including the 3D coronal models and a 3D MAS-MHD model run. With these models, we use the EPREM model to find the fluxes and spectra of energetic protons at 1 AU. We then compare the modeling results with in-situ measurements. In the second part, I describe a deep learning approach that I developed to forecast the integral flux of energetic protons in three energy channels across three different forecasting horizons.

## 4.1 Introduction

CMEs represent significant phenomena in solar physics, captivating attention due to their prominent role in solar activity. Traditionally, CMEs have been identified through white light observations, providing valuable insights into their characteristics (Vourlidas et al. 2003; Zhang & Dere 2006; Bein et al. 2011). However, a comprehensive understanding of these eruptions requires examination across multiple wavelengths, including ultraviolet and radio bands, where observations reveal additional facets of their dynamics (Bastian et al. 2001; Veronig et al. 2010). Notably, EUV observations, facilitated by instruments like the AIA on the Solar Dynamics Observatory, have become instrumental in capturing the early stages of CMEs (Lemen et al. 2012; Pesnell et al. 2012).

CMEs, in their trajectory through the solar corona, can give rise to shock waves when their propagation speeds surpass the local fast magnetosonic speed, observable as EUV waves or CBFs (Thompson et al. 1998; Long et al. 2011). These shock waves are crucial in the context of SEP acceleration. While solar flares also contribute to SEP production, recent advancements in observations and numerical modeling have reshaped the prevailing understanding. It is now recognized that, especially in their early stages (below 5–10 $R_{\odot}$ ), CMEs often drive shocks capable of accelerating SEPs to energies exceeding 100 MeV/n (Ontiveros & Vourlidas 2009; Gopalswamy & Yashiro 2011; Battarbee et al. 2013; Kozarev et al. 2013; Schwadron et al. 2014; Kong et al. 2017).

Previous research has primarily focused on characterizing the dynamics of CMEs and their associated shocks within the solar corona, utilizing advanced observations spanning white light, EUV, and radio wavelengths (Vourlidas et al. 2003; Zhang & Dere 2006; Bein et al. 2011). The relationship between CMEs and shock waves, particularly CBFs, has been a subject of in-depth investigation. Notably, Kozarev et al. (2019) conducted a comprehensive study of nine distinct western CBF events, employing the DSA model proposed by Kozarev & Schwadron (2016). Their findings revealed variations in SEP production among events, coupled with evolving patterns over the course of each event. Moreover, the acceleration efficiency demonstrated a strong dependence on the diverse coronal environments traversed by the propagating shock waves.

Building upon the groundwork laid by Kozarev et al. (2019), this present study extends its scope by modeling the dynamics of CBF-related shock/compression waves and particle acceleration up to $10\,R_{\odot}$ . This advancement involves integrating outcomes with a comprehensive numerical particle transport model, allowing for comparisons with in situ observations. This marks a significant enhancement in our methodology, representing the first validated extension of Sun-to-Earth physics-based modeling for

SEP acceleration and transport within our current understanding of solar physics (Kozarev et al. 2022).

In the quest to understand the mechanisms through which SEPs are produced by coronal shocks throughout the inner heliosphere, considerable progress has been made. Traditionally, the prevailing assumption was that SEP acceleration primarily occurred in interplanetary space, driven by in situ measurements of Energetic Storm Particle (ESP) fluxes during encounters with IP shocks by spacecraft. However, recent advancements in observations and numerical modeling have reshaped this understanding.

CMEs emerge as the principal contributors to the generation of SEPs, encompassing ions and electrons with energies several orders of magnitude beyond the thermal coronal plasma (Reames 1999). While solar flares also contribute to SEP production during solar eruptions, CMEs predominantly facilitate SEP generation within the magnetized shock waves they instigate and in plasma compressions resulting from their expansive forces. The prevailing assumption that the majority of SEP acceleration transpired in interplanetary space has been challenged by the revelation that, particularly in their initial stages (below 5–10 $R_\odot$ ), CMEs frequently induce shocks capable of accelerating SEPs to energies surpassing 100 MeV/n (Ontiveros & Vourlidas 2009; Gopalswamy & Yashiro 2011; Battarbee et al. 2013; Kozarev et al. 2013; Schwadron et al. 2014; Kong et al. 2017).

Efforts have been directed towards characterizing the dynamics of CMEs and the accompanying shocks within the solar corona, employing increasingly sophisticated observations spanning white light, EUV, and radio wavelengths. This exploration aims to deduce early-stage SEP production in the solar corona (Kozarev et al. 2013; Schwadron et al. 2015). In a notable contribution, Kozarev et al. (2019) conducted an in-depth study of nine distinct western CBF events, utilizing the Diffusive Shock Acceleration (DSA) model proposed by Kozarev & Schwadron (2016). Their findings highlighted variations in SEP production among events, along with evolving patterns over the duration of each event. Importantly, the acceleration efficiency exhibited a strong dependence on the diverse coronal environments traversed by the propagating shock waves.

This study, led by Kozarev et al. (2022), advances the work of Kozarev et al. (2019) by extending the modeling of CBF-related shock/compression wave dynamics and particle acceleration to 10 $R_\odot$ . Our approach involves coupling these results with a global numerical particle transport model and comparing the outcomes to in situ observations. This represents a significant enhancement in our methodology, marking the first validated extension of Sun-to-Earth physics-based modeling for SEP acceleration and transport within our current understanding of solar physics.

Several models are available, or under development, for forecasting SEP, which use diverse approaches and serve different objectives. These models comprise computationally complex physics-based models, quick and simple empirical models, Machine Learning (ML)-based models, and hybrid models that combine different approaches and produce different types of outputs, including deterministic, probabilistic, categorical, and binary. Deterministic models always generate the same output without any randomness or stochastic components, such as predicting the SEP flux at a specific moment or the arrival time of SEP. On the other hand, probabilistic models provide a probability value that reflects the likelihood of an SEP event occurring. However, replicating SEP fluxes at a specific time is still a significant challenge for current models.

An excellent review on SEP models and predictive efforts was recently published by Whitman et al. (2023), which summarizes the majority of the existing models. For instance, Papaioannou et al. (2022) introduced the Probabilistic Solar Particle Event Forecasting (PROSPER) model, which is incorporated into the Advanced Solar Particle Event Casting System (ASPECS)[1]. The PROSPER model utilizes a Bayesian approach and data-driven methodology to probabilistically predict SEP events for 3 integral energy channels >10, >30, and >100 MeV. The model's validation results indicate that the solar flare and CME modules have hit rates of 90% and 100%, respectively, while the combined flare and CME module has a hit rate of 100%. Bruno & Richardson (2021) developed an empirical model to predict the peak intensity and spectra of SEP at 1 AU between 10 and 130 MeV, using data from multiple spacecraft. The model is tested on 20 SEP events and shows good agreement with observed values. The spatial distribution of SEP intensities was reconstructed successfully, and they found a correlation between SEP intensities and CME speed.

Hu et al. (2017) extended the Particle Acceleration and Transport in the Heliosphere (PATH) model to study particle acceleration and transport at CME-driven shocks. They showed that the model can be used to obtain simultaneous calculations of SEP characteristics such as time-intensity profiles, instantaneous particle spectra, and particle pitch angle distributions at multiple heliospheric locations. Overall, results resemble closely those observed in situ near the Earth but also yield results at other places of interest, such as Mars, making it of particular interest to Mars missions. SPREAdFAST (Kozarev et al. 2017,

[1]ASPECS: `http://phobos-srv.space.noa.gr/`

2022) is a physics-based, data-driven framework that utilizes EUV observations and models to simulate SEP fluxes at 1 AU and to estimate energetic particle acceleration and transport to various locations in the inner heliosphere. It generates time-dependent histograms and movies distributing them through an online catalog. The accuracy and efficiency of the model were encouraging, but the highest energy fluxes showed disagreement with in situ observations by the SOHO/ERNE instrument. However, the framework has great potential for space weather science and forecasting.

In Aminalragia-Giamini et al. (2021), they used neural networks to provide probabilities for the occurrence of SEP based on soft X-rays data from 1988 to 2013. They obtained >85% for correct SEP occurrence predictions and >92% for correct no-SEP predictions. Lavasa et al. (2021) described a consistent approach to making a binary prediction of SEP events using ML and conventional statistical techniques. The study evaluated various ML models and concluded that random forests could be the best approach for an optimal sample comprising both flares and CMEs. The most important features for identifying SEP were found to be the CME speed, width, and flare soft X-ray fluence. Kasapis et al. (2022) employed ML techniques to anticipate the occurrence of a SEP event in an active region that generates flares. They utilized the Space-Weather MDI Active Region Patches (SMARP) dataset, which comprises observations of solar magnetograms between June 1996 and August 2010. The SMARP dataset had a success rate of 72% in accurately predicting whether an active region that produces a flare would result in a SEP event. Moreover, it provided a competitive lead time of 55.3 min in forecasting SEP events.

Engell et al. (2017) introduced the Space Radiation Intelligence System (SPRINTS), a technology that uses pre- and post-event data to forecast solar-driven events such as SEP. It integrates automatic detections and ML to produce forecasts. Results show that SPRINTS can predict SEP with an 56% probability of detection and 34% false alarm rate. Nevertheless, the HESPERIA REleASE tools provide real-time predictions of the proton flux at L1 by using near-relativistic electrons as a warning for the later arrival of protons and have been set to operation (Malandraki & Crosby 2018). Historical data analysis indicates high prediction accuracy, with a low false alarm rate of approximately 30% and a high probability of detection of 63% (Malandraki & Crosby 2018).

Forecasting SEP is a critical task that serves operational needs and provides insight into the broader field of space weather science and heliophysics. As emphasized in previous works, a high precision forecasting model is urgently required to predict SEP flux within a period of time, given the risks associated with these events. This highlights the critical requirement for a dependable forecasting system that can mitigate the risks associated with SEP.

Scientists have been using physics-based and empirical models for decades to forecast SEP. However, these models have certain limitations. Physics-based models require accurate input data and underlying physical assumptions. In addition, the complexity of the physics involved and incorrect parameters may introduce uncertainties that can lead to inaccurate predictions. On the other hand, empirical models rely on historical data to make predictions. While they can be accurate sometimes, they may be unable to account for changes in physical conditions related to the acceleration and propagation of SEP, which can influence prediction accuracy. ML models, however, provide a different approach to SEP forecasting. These models can analyze vast amounts of data, learning patterns from the data that are used, and connections that may not be obvious to experts. Additionally, ML models can adapt to changes in underlying physical conditions, resulting in more accurate predictions as more data is collected; they also provide relatively rapid forecasts, which allows for incorporation into a real-time forecasting workflow.

In the upcoming sections, I will explore the limitations in accuracy that arise from dealing with an imbalanced dataset and low-resolution data. Specifically, the presence of intrinsic outliers in the time series data pertaining to SEP flux poses a significant challenge in modeling. These outliers correspond to occurrences of SEP events and, consequently, have an impact on the accuracy of predictions. Notably, they often lead to an underestimation of the SEP fluxes, primarily due to the predominance of relatively low values throughout the majority of the time interval.

In the first part, we extend the work in Chapter 2 on the kinematics of CBFs and expand on previous relevant investigations by modeling CBF-related shocks and particle acceleration up to 10 $R_\odot$ Our modeling approach incorporates coupling to a numerical model of particle transport throughout the heliosphere, with validation against in-situ spacecraft measurements. Our study implements, for the first time, an extensive physics-based model linking CME-driven shock acceleration with the propagation of SEPs from the Sun to Earth. In the second part, I present advanced deep learning models to forecast the daily integral flux of SEP over a 3-day forecasting window by using bi-directional long short-term memory (BiLSTM) neural networks, for 3 energy channels (>10, >30, and >60 MeV). Our models can forecast the time-dependent development of SEP events in different energy domains, which can be used to model the space radiation profiles using frameworks such as BRYNTRN Wilson et al. (1988) and GEANT4 (Truscott et al. 2000).

## 4.2 Early-Stage SEP Acceleration by CME-Driven Shocks

### 4.2.1 Overview

CMEs stand out as one of the most prevalent expressions of solar activity, attracting considerable attention in solar physics. Traditionally defined through white light observations (Vourlidas et al. 2003; Zhang & Dere 2006; Bein et al. 2011), these eruptions reveal diverse facets when examined across ultraviolet and radio bands (Bastian et al. 2001; Veronig et al. 2010). Particularly noteworthy is their observation in EUV light, a realm where telescopes like the AIA onboard SDO (Lemen et al. 2012; Pesnell et al. 2012) excel in capturing the early stages of CMEs.

CMEs, in their dynamic journey through the solar corona, can generate shock waves if their propagation speeds surpass the local speed of information, typically the fast magnetosonic speed. These shock waves manifest prominently in EUV observations as EUV waves or, more specifically, as CBFs (Thompson et al. 1998; Long et al. 2011). The intricate relationship between CMEs and these shock waves forms a crucial aspect of solar physics.

As the primary contributors to SEPs, CMEs play a pivotal role in the energization of ions and electrons to levels significantly exceeding the thermal coronal plasma (Reames 1999). Flares also contribute to SEP production during solar eruptions. The acceleration of SEPs in CMEs predominantly occurs within the magnetized shock waves they propel, as well as in plasma compressions induced by the CMEs. While historical perspectives inferred the bulk of SEP acceleration in interplanetary space from in situ observations of energetic storm particle (ESP) fluxes during the traversal of interplanetary shocks by spacecraft, recent advancements in observations and numerical models have reshaped this understanding.

Over the past fifteen years, sophisticated observations and modeling techniques have revealed that, in their early stages (below 5–10 $R_\odot$ ), CMEs often drive shocks (Ontiveros & Vourlidas 2009; Gopalswamy & Yashiro 2011). These shocks, in turn, exhibit the capability to accelerate SEPs to energies exceeding 100 MeV/n (Battarbee et al. 2013; Kozarev et al. 2013; Schwadron et al. 2014; Kong et al. 2017). Consequently, recent research has focused on characterizing the dynamics of CMEs and the associated shocks in the solar corona, employing advanced observations spanning white light, EUV, and radio wavelengths.

Building upon this foundation, efforts have been made to estimate the early-stage SEP production in the corona (Kozarev et al. 2013; Schwadron et al. 2015). In a notable contribution, Kozarev et al. (2019) conducted an in-depth study of nine distinct western CBF events. Utilizing the diffusive shock acceleration (DSA) model proposed by Kozarev & Schwadron (2016), they simulated particle acceleration in the very early stages, while the CMEs were still below 1.5 $R_\odot$ . Their findings highlighted variations in SEP production among events, along with evolving patterns over the event's duration. Importantly, the acceleration efficiency exhibited a strong dependence on the diverse coronal environments traversed by the shock waves.

This study, led by Kozarev et al. (2022), advances the work of Kozarev et al. (2019) by extending the modeling of CBF-related shock/compression wave dynamics and particle acceleration to 10 $R_\odot$ . Our approach involves coupling these results with a global numerical particle transport model and comparing the outcomes to in situ observations. This represents a significant enhancement in our methodology, marking the first validated extension of Sun-to-Earth physics-based modeling for SEP acceleration and transport within our current understanding of solar physics. In order to analyze particle fluxes at 1 AU and compare them with observational data, we employ the SPREAdFAST framework that is explained in Chapter 2.

The purpose of the SPREAdFAST framework is to model and analyze the particle fluxes from the Sun to Earth, specifically focusing on SEP events. The project combines detailed observations of CBFs with modeling of the coronal plasma and the resulting SEP production and interplanetary transport. The SPREAdFAST framework utilizes physics-based modeling to simulate the evolution of the plasma upstream of the coronal shock associated with CBFs and the subsequent acceleration and transport of protons from the Sun to 1 AU. It incorporates various components such as EUV observations, shock dynamics, particle acceleration, and interplanetary transport. The project aims to provide a better understanding of the processes involved in SEP events and improve forecasting capabilities for these events. By modeling a large number of events and comparing the model results with in situ observations, the SPREAdFAST project contributes to the advancement of Sun-to-Earth physics-based modeling of SEP acceleration and transport. Overall, the SPREAdFAST project is a comprehensive effort to study and simulate the complex phenomena associated with SEP events, with the goal of enhancing our knowledge and predictive capabilities in this field.

The SPREAdFAST framework includes the following components:

- CBF Kinematics and Geometric Modeling: This component characterizes the kinematics of CBFs using observations from the AIA instrument. It estimates the CBF kinematics, including the front, peak, and back edge positions over time, as well as the mean intensity and thickness of the CBFs.

- Coronal Shock and Particle Acceleration Modeling: This component models the evolution of the plasma immediately upstream of the coronal shock associated with CBFs. It incorporates the physics of coronal shock waves and the process of particle acceleration through diffusive shock acceleration.

- Interplanetary Particle Transport Modeling: This component simulates the transport of accelerated particles from the corona to 1 AU, which is the distance between the Sun and Earth. It takes into account the interplanetary magnetic field and other factors that influence particle propagation.

- Comparison with Observations: The framework compares the modeled particle fluxes and fluences at 1 AU with observations from instruments like the SOHO and the Energetic and Relativistic Nuclei and Electron (ERNE) instrument. It evaluates the accuracy of the model predictions by calculating metrics such as the Mean Squared Logarithmic Error (MSLE).

Overall, the SPREAdFAST framework combines detailed observations, physics-based modeling of coronal shocks and particle acceleration, and interplanetary transport modeling to analyze and forecast SEP events from the Sun to Earth.

### 4.2.2 Event Selection

Our study focuses on a carefully selected set of solar events to ensure the robustness of our analysis. We initiated the event selection process by identifying proton events within the energy range of 17–22 MeV, as observed by the Solar and Heliospheric Observatory/Energetic and Relativistic Nuclei and Electron (SOHO/ERNE) instrument during the period spanning 2010-2017. This initial screening yielded a total of 216 events.

To refine our dataset and concentrate on events with clear solar signatures, we excluded proton events lacking associated flares,CMEs, and those devoid of EUV waves before the onset of SEP events. This step resulted in the exclusion of 39 events, leaving us with 177 events for further consideration. Further narrowing our focus, we excluded cases where EUV waves were absent or where EUV data was not available, even if flares or CMEs had been identified. This decision aligns with the requirements of the SPREAdFAST model, which necessitates the presence of an EUV wave for accurate analysis. Consequently, this step reduced the dataset to 105 events. In the interest of precision and relevance, we removed several events with uncertain EUV waves, deeming them more appropriate for investigations related to different solar eruptions. This additional refinement brought the total down to 99 events.

A meticulous examination of the remaining dataset revealed 62 events with measurable near-limb or off-limb CBFs, aligning with the capabilities of our analytical framework. These 62 events constitute our final selection for in-depth analysis and interpretation, as outlined in Table 1 in our paper (Kozarev et al. 2022). For a comprehensive reference, this table provides detailed information for each event, including the date, start and end times, and class of the associated flare. Additionally, it includes the source location on the solar disk specified in helioprojective Cartesian coordinates. These key details were sourced from the Heliophysics Events Knowledge Base, ensuring accurate and standardized information for each event in our study.

### 4.2.3 Coronal SEP Acceleration

Having established plasma parameters along individual shock-crossing field lines, our study employs the coronal DSA model (Kozarev & Schwadron 2016; Kozarev et al. 2019) to calculate proton acceleration dynamics from the low corona to $10\,R_\odot$. Specifically designed to utilize remote solar observations and data-driven model output from the CASHeW framework, this model solves for the large-scale acceleration of charged particles induced by CME-driven shocks.

The model incorporates time-dependent estimates of shock speed ($V_{shock}$), density jump ratio ($r$), magnetic field strength ($|B|$), and shock angle ($\theta_{BN}$) for multiple shock-crossing field lines. Using these parameters, the model computes the minimum shock injection momenta for particles. It takes as input a particle distribution function and produces time-dependent distribution function spectra or fluxes as output. The obtained solution (Equations 8–11 in cKozarev & Schwadron (2016)) provides both the first distribution function ($f_1$) and momentum ($p_1$) values for an initial momentum ($p_0$). The model iteratively solves for subsequent values ($f_i$ and $p_i$) at time steps separated by the observational cadence $\delta$t of the instrument (in this case, SDO/AIA). The model is executed for each individual shock-crossing field line, based on observed and calculated parameters at a single shock-crossing point along it. Flux spectra at each time step are then computed, and the model's validity has been confirmed through its application in the analysis of several SEP events.

### 4.2.4 Input Data and Spectral Fitting

The model relies on input data derived from observations-based suprathermal proton spectra obtained from 1 AU fluxes recorded by the SOHO/ERNE instrument (Torsti et al. 1995). These spectra are acquired during the 24-hour period of quiet time preceding each SEP event. Power laws are fitted to each suprathermal spectrum within the energy range of 0.056–3.0 MeV and scaled to a distance of $1.05\,R_\odot$, assuming a simple inverse square dependence on radial distance to conserve flux. While the current implementation does not consider adiabatic cooling or other particle transport effects, acknowledging their significance, a comprehensive exploration of these effects will be conducted in future studies to determine general trends for forecasting.

The time-independent power law input spectra generated for the DSA model represent the suprathermal spectrum calculated for $1.05\,R_\odot$. These spectra are injected at all shock positions and distances without modification to account for changing shock locations in the current model implementation. This approach allows for a detailed examination of proton acceleration dynamics and flux evolution under the influence of CME-driven shocks in the solar corona.

### 4.2.5 Transport of Accelerated SEPs and Comparison with ERNE Observations

The culmination of our modeling chain involves the transport of accelerated SEPs to 1 AU, followed by a comprehensive comparison with particle observations obtained through the ERNE instrument. This final phase is executed by utilizing the averaged fluxes derived from the entire event, exemplified here with the illustrative case of the May 11, 2011 event.

To achieve this, we employ a modified version of the Energetic Particle Radiation Environment Module model (Schwadron et al. 2010, EPREM). The modified EPREM model facilitates the transport of fluxes through a Parker-type static interplanetary medium. The particle injection from the DSA model into EPREM is sustained throughout the duration of the coronal shock event. This model incorporates essential effects such as pitch-angle scattering, adiabatic focusing and cooling, convection, streaming, and stochastic acceleration.

The solver demands inner boundary conditions, with no initial conditions imposed. It features a dynamic simulation grid where computational nodes are carried away from the Sun with the solar wind, naturally adopting the shape of a three-dimensional interplanetary magnetic field. EPREM employs an interplanetary magnetic field model, incorporating radial and azimuthal field components that fall off with radial distance and a constant latitudinal component—the Parker spiral model.

The spatial grid structure is organized in nested cubes, subdivided into square arrays of square cells, representing the propagation pathway of energetic particles. The inner boundary surface rotates with the solar rotation rate and is expelled outward at the solar wind speed. At each time step, a new shell of cells is created at the inner boundary, initiating its outward propagation. The inner boundary for the EPREM simulation is fixed at $1.05\,R_\odot$, while the outer boundary varies for individual field lines due to dynamic conditions, consistently exceeding 1 AU. The model's credibility has been extensively validated through its application in Solar Energetic Particle studies (Kozarev et al. 2010; Schwadron et al. 2014).

For the EPREM model runs conducted on the 62 events in this study, standardized input parameters were employed. These parameters include a mean free path ($\lambda_0$) of 0.1 AU at 1 AU and 1 GV magnetic rigidity, a constant solar wind speed ($V_{sw}$) of $500\,km\,s^{-1}$, proton number density ($n$) at 1 AU set at 5.0 cm$^{-3}$, and a magnetic field magnitude ($|B|$) at 1 AU of 5.0 $\times$ 10$^{-5}$ G. The mean free path is additionally scaled with proton rigidity and radial distance from the Sun to incorporate the magnetic turbulence spectrum and its radial dependence (Zank et al. 1998; Li et al. 2003; Sokolov et al. 2004; Verkhoglyadova et al. 2009), providing the parallel mean free path for the simulation.

An energy grid with 20 points, logarithmically spaced between 1 and 200 MeV, and a 4-point pitch-angle grid were utilized. A simulation time-step of 0.5 AU/c (approximately 4 minutes) with 30 sub-steps allowed for accurate calculation of SEP propagation among nodes. These baseline simulations encompassed all effects of diffusive transport, including adiabatic cooling/heating, adiabatic focusing, pitch-angle scattering, convection with the solar wind, and streaming. Subsequent work will incorporate the effects of perpendicular diffusion and particle drifts. The simulations were concluded at 9.6 hours from the onset of the event at the Sun for all events, focusing on modeling their initial stages.

We used a combination of telescopic observations and dynamic physical models to simulate the acceleration of SEPs in global coronal shock events. We first observed off-limb CBFs and studied their interaction with the coronal plasma using synoptic MHD simulations. Based on these observations and simulations, we then employed an analytical DSA model to simulate the SEP acceleration. The simulated fluxes obtained from the DSA model were used as time-dependent inner boundary conditions for modeling the particle transport to 1 AU. This approach allowed us to study the early-stage acceleration and transport of SEPs from the Sun to 1 AU.

The criteria used to select the events for analysis in the study of the SPREAdFAST framework were as follows:

- Proton events in the energy range of 17-22 MeV observed by the SOHO/ERNE instrument from 2010 to 2017 were initially identified.
- Events without identified flares and CMEs and without EUV waves preceding the SEP event were excluded.
- Events without EUV waves or no EUV data, even if they had identified flares/CMEs, were also excluded.
- Uncertain EUV waves that were not relevant to the specific solar eruption were dropped.
- Events with measurable near-limb or off-limb CBFs that could be analyzed with the SPREAdFAST framework were selected.

In total, 62 events met the selection criteria and were included in the analysis.

The kinematics of CBFs are characterized using the methodology of the CASHeW framework. This framework estimates the CBF kinematics by following the leading edge of the front on consecutive images. It calculates the kinematics of the front, peak, and back edge of the CBFs over time, allowing for the estimation of their time-dependent mean intensity and thickness. The kinematics are determined using time-height maps (J-maps) generated with the CASHeW code for each event. The radial and lateral wave front positions are measured in these J-maps, providing information on the radial and lateral positions, speeds, accelerations, mean wave intensities, and wave thickness of the CBFs.

The methodology used to characterize the kinematics of CBFs is based on the CASHeW framework. This framework involves analyzing observations from the AIA instrument on board the SDO. The kinematics of CBFs are determined by tracking the leading edge of the front on consecutive images. Time-height maps, also known as J-maps, are created by stacking columns of pixels in a desired direction from a solar image. The shape of the track on these J-maps depends on the direction and speed of the CBF. The CASHeW code identifies the radial and lateral wave front positions over time in the J-maps, allowing for the estimation of the CBF kinematics, including speeds, accelerations, mean wave intensities, and wave thickness. A three-dimensional geometric model, known as the Synthetic Shock Model (S2M), is then created based on the measured front positions, which describes the shock surface at regular intervals. This model is propagated through the solar corona using a synoptic coronal MHD model, providing information on the relevant parameters for coronal shock acceleration of SEPs.

In the SPREAdFAST DSA model, the shock-crossing field lines are modeled by dividing the shock surface into three regions: the *nose* of the shock model, which consists of model points on the spheroidal cap; and two flanks or zones, divided by a plane parallel to the Sun-Earth line. The plasma parameters at the points on these three surfaces are examined separately. The model calculates the proton acceleration along these shock-crossing field lines based on time-dependent estimates of shock speed, density jump ratio, magnetic field strength, and shock angle. The model solves for the coronal charged particle acceleration by large-scale CME-driven shocks and provides time-dependent distribution function spectra or fluxes as output.

The method used to compare the modeled and observed proton fluences is by analyzing scatter plots of the fitted power indices of the proton fluences from the EPREM model and the ERNE observations.

The power law indices are compared between the two sets, and the onset hours for the proton events are also compared. The comparison helps evaluate the performance of the modeling framework in predicting the proton fluxes. Additionally, histograms and Mean Squared Logarithmic Error (MSLE) are used to assess the agreement between the modeled and observed fluence spectra and onset times.

### 4.2.6 Results and Discussions

The study's findings have important implications for understanding and predicting solar particle radiation. By modeling the dynamics of shock waves and particle acceleration in the solar corona, the study provides valuable insights into the factors that influence the efficiency of particle acceleration. The results highlight the significant role of the coronal environment in shaping the acceleration and transport of SEPs from the Sun to Earth. One key implication is that the overlying coronal structure and the particle energy play a crucial role in determining where SEPs are produced during CME-driven shock and compressive waves. The study shows that the large gradients in plasma parameters between neighboring streamers, quiet-Sun areas, and coronal holes lead to continuous changes in the acceleration process. This knowledge can help improve our understanding of the spatial distribution of SEPs and their energy dependence. Furthermore, the study's findings contribute to the development of physics-based models for forecasting SEP events. The SPREAdFAST framework used in the study demonstrates the potential for accurately simulating the evolution of SEPs from the Sun to 1 AU. This framework can be further refined and utilized for early-stage forecasting of SEP events, providing valuable information for space weather prediction and mitigation efforts. Overall, the study enhances our understanding of the complex processes involved in solar particle radiation and provides a foundation for improving our ability to predict and mitigate the impacts of these events on space weather.

The main discrepancies between the modeled and observed fluxes in the study are primarily seen at higher energies. Above 15 MeV, there is a discrepancy in the time profile, with the observed proton fluxes rising approximately 1 hour before the simulation. Additionally, the fluxes at the highest energies show the most disagreement, mainly due to the slope of the increase and the onset times. These discrepancies indicate the need for further improvements and refinements in the modeling framework to better match the observations.

## 4.3 Solar Proton Flux Forecasting with Deep Learning Models

### 4.3.1 Data preparation

In this section, I describe the physical quantities, the types of inputs and their sources, as well as the outputs I are forecasting. Some of the technical terms used in this study are explained further in the appendices.

In order to capture the variability of solar activity, which modulates the SEP flux, I selected input physical quantities that describe both the interplanetary medium and solar activity. These input features can be categorized into two groups: remote signatures and in-situ measurements. The remote signatures consist of the F10.7 index, as well as the long-wavelength ($X_L$) and short-wavelength ($X_S$) x-ray fluxes. The F10.7 index represents the flux of solar radio emission at a wavelength of 10.7 cm, measured in solar flux units (sfu). To obtain the x-ray fluxes, I utilized 1- and 5-minute averaged data from the GOES database[2], specifically at long wavelengths (1 - 8 Å) and short wavelengths (0.5 - 4.0 Å).

The in-situ measurements encompass the near-Earth solar wind magnetic field and plasma parameters. These include the solar wind speed (in km $s^{-1}$), average IMF strength (in nT), and the integral SEP fluxes at three energy channels: >10, >30, and >60 MeV, which correspond to the GOES channels (in 1/$cm^2$ sec ster). These SEP fluxes were obtained from multiple spacecraft stationed at the first Lagrange point (L1) throughout the study period. In particular, the IMF and plasma data in the OMNI database are obtained from the IMP, Wind, and ACE missions, while the energetic particle fluxes are obtained from the IMP and GOES spacecraft[3].

To ensure a comprehensive dataset, I acquired hourly-averaged data covering a timeframe from December 1976 to July 2019, which spans the past four solar cycles. These data were sourced from the Space Physics Data Facility (SPDF) OMNIWeb database[4], hosted by the Goddard Space Flight Center. This database provides a wealth of information, including integral proton fluxes, as well as an extensive

[2]GOES SXR Database: `https://satdat.ngdc.noaa.gov/sem/goes/data/avg/`
[3]OMNIWeb Data Documentation: `https://omniweb.gsfc.nasa.gov/html/ow_data.html`
[4]OMNI Database: `https://omniweb.gsfc.nasa.gov`

range of solar wind plasma and magnetic field parameters. Lastly, the daily data on sunspot numbers were obtained from the Sunspot Index and Long-term Solar Observations (SILSO) archive[5], maintained by the World Data Center.

Figure 4.1 shows a plot for the timeseries data of all features. The top 3 panels are the logarithms of the SEP integral flux at the 3 energy channels (log_PF10, log_PF30, and log_PF60), then the sunspot number, the F10.7 index (F10_idx), the logarithms of the x-ray fluxes (log_Xs and log_Xl), the solar wind speed (Vsw), and the average magnitude of the IMF (avg_IMF). Throughout this chapter, I adopt the convention that "log" refers to the common logarithm with a base of 10. The gray shades refer to the timespan of solar cycles. The blue, orange, and gold colors refer to the training, validation, and test sets, respectively. The data split method will be explained shortly.

Since the input SEP data have been compiled from various spacecraft, it may have artifacts even after processing. In particular, there are occasional jumps in the background level. There are also several day-long gaps in the OMNI solar wind parameters from the early 1980s to mid-1990s where only IMP 8 data are available and this spacecraft spent part of each orbit in the magnetosphere. I are reasonably confident that these issues do not influence the overall analysis significantly.

In deep learning applications, the dataset is split into 3 sets; namely the training set, the validation set, and the test set. The training set is usually the largest chunk of data that is used to fit the model. The validation set is a smaller chunk of data used to fine-tune the model and evaluate its accuracy to ensure it is unbiased. The test set is the out-of-sample data exclusively used to assess the final model when performing on unseen data (Ripley 1996).

After inspecting the correlation between the solar wind indices and the SEP integral fluxes in the OMNIWeb database, I chose the top-correlated features with the SEP flux. The correlations were made between the SEP fluxes and the individual parameters. Hence I took only timeseries of logarithms of the protons' integral flux at 3 energy channels (>10, >30, and >60 MeV), the timeseries of logarithm of the X-ray fluxes, the F10.7 index, the sunspot number, the solar wind speed, and the average strength of the IMF as input parameters to our model. The log of the SEP flux was used across the whole study. The correlation matrices for the training, validation, and test sets are shown in Figure 4.2. The X-ray and proton fluxes were converted into the logarithmic form because it was more convenient than the original form of data since the time series data were mostly quiet and had numerous sharp spikes, which correspond to solar events. Based on a previous experience with NNs (Nedal et al. 2019), I found that training separate models for each target (output) feature can lead to better results. This is because a dedicated model for each output feature can more easily learn the interrelationships between input features and make more accurate predictions. Therefore, in our current study, I trained 3 separate models, each one targeting the logarithm of the protons integral flux at a specific energy channel.

In order to ensure consistency across all features, all durations of the time series data of the physical quantities were matched to be within the same time range. Subsequently, the dataset was resampled to obtain daily averaged data, resulting in a significant reduction of the dataset size by a factor of 24. This reduction facilitated expeditious training and yielded prompt results.

There were missing data values in the original dataset; for the $B_{avg}$ ($\sim 10.7\%$), $V_{sw}$ ($\sim 10.5\%$), F10.7-index ($\sim 0.08\%$), short-band x-ray flux ($\sim 8\%$), long-band x-ray flux ($\sim 9.8\%$), and proton fluxes ($\sim 4.3\%$). The data gaps were linearly interpolated.

In timeseries forecasting, it is a common practice to take a continuous set of data points from the main dataset to be the validation set and another smaller chunk of data to be the test set, for instance in Pala & Atici (2019); Benson et al. (2020); **?**); Zhu et al. (2022). From our experiments, I got descent results when I applied the same data split method, but the results were a bit biased toward the end of the solar cycle 24 and the testing set was biased towards a quiet period. So, I adopted the 9-2-1 strategy, that is taking from each year 9 months to be added in the training set, 2 months to be added in the validation set, and 1 month to be added in the test set. This is applied over the ~43 years of data (Fig. 4.1), which yields 74.29% of the data for the training set, 16.2% for the validation set, and 9.51% for the testing set. By doing so, I eliminated the need to do cross-validation and hence, made the training more efficient. It is worth to mention that the timeseries data must not be shuffled as that will break temporal and logical order of measurements, which must be maintained.

### 4.3.2 Method

In this section, I introduce the data analysis methods used in this work. I start with explaining the model selection phase, followed by a discussion of the bi-directional long short-term memory (BiLSTM)

[5]Sunspot Number Dataset: `https://www.sidc.be/silso/home`

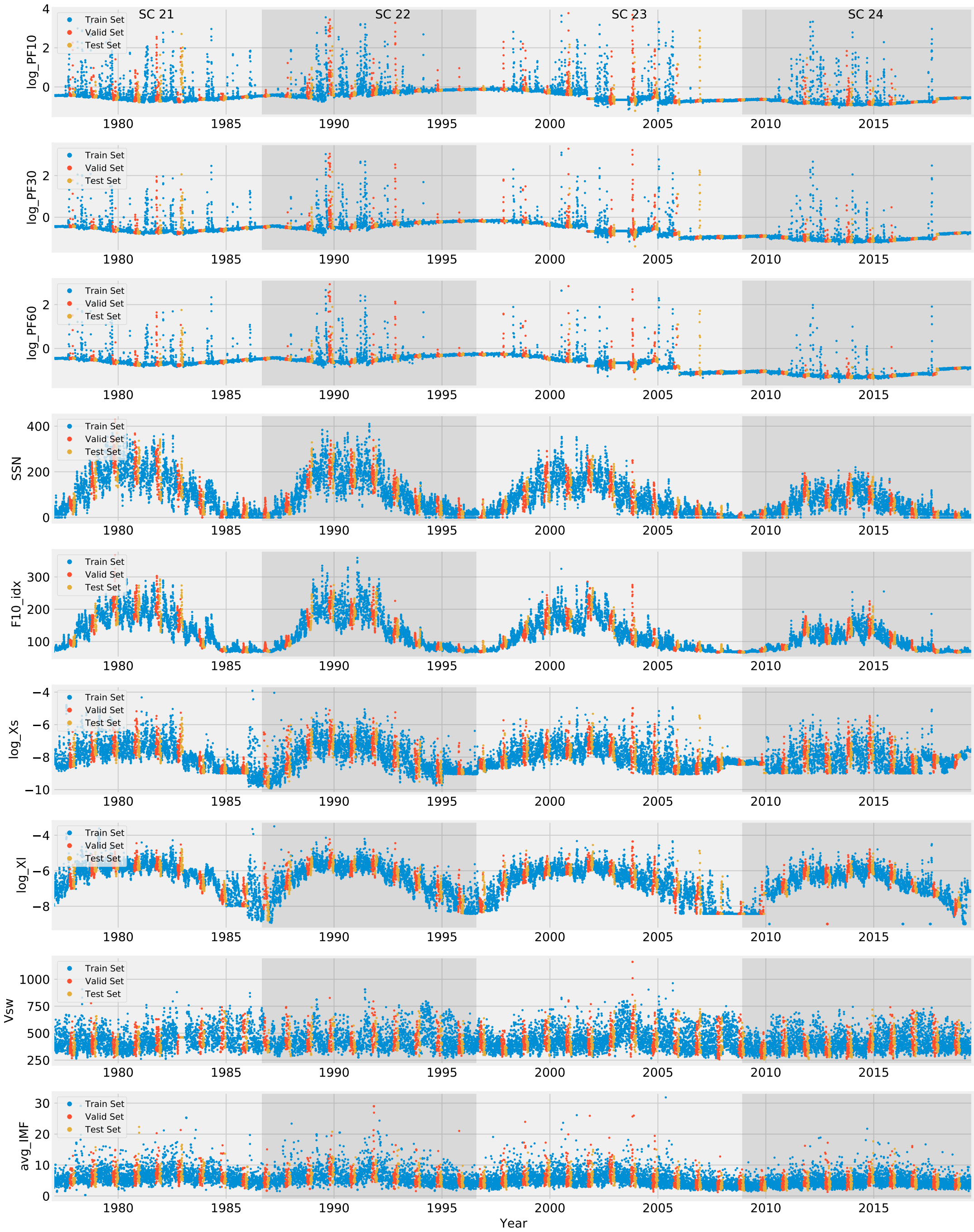


Figure 4.1: Data splitting for all input features, showing the training, validation, and testing sets. Daily data from 1976-12-25 00:00 to 2019-07-30 00:00. The gray shading labels the solar cycles from SC21 to SC24.

neural network architecture. The technical terminologies are described in the appendices.

### The Bi-LSTM Model

Recurrent neural networks (RNNs) that support processing input sequences both forward and backward are known as Bidirectional Long Short-Term Memory (BiLSTM) neural networks (Schuster & Paliwal 1997). Regular RNNs (Hochreiter & Schmidhuber 1997; Kolen & Kremer 2001) depend on the prior hidden state and the current input to determine the output at a given time. The output of a BiLSTM network, on the other hand, is dependent on the input at a given moment as well as the previous and future hidden states. As a result, the network is able to make predictions using contexts from the

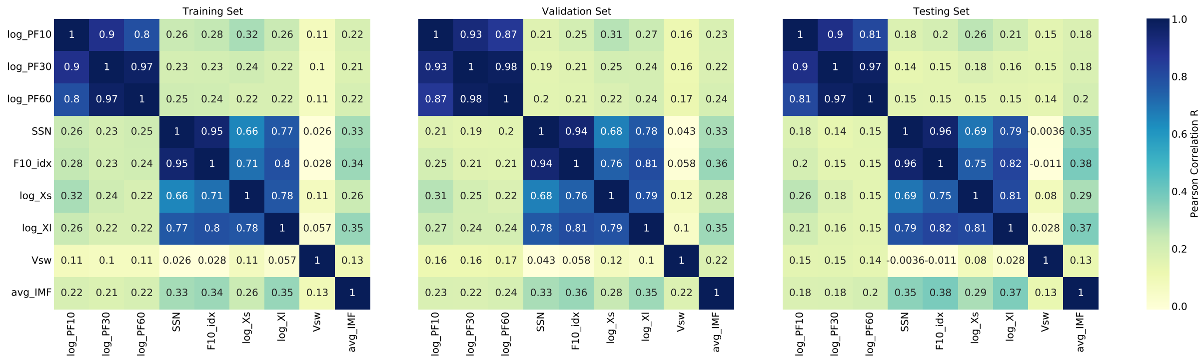


Figure 4.2: Correlation matrices show the correlation between the features in the training, validation, and test sets.

past as well as the future. Hence, accuracy is improving. Each BiLSTM layer consists of two LSTM layers; a forward layer that processes the input sequences from the past to future, and a backward layer that processes the input sequences from the future to the past, as illustrated in Figure 4.3, to capture information from both past and future contexts. The output from each layer is concatenated and fed to the next layer, which can be another BiLSTM layer or a fully connected layer for final prediction.

BiLSTM networks are advantageous than traditional LSTM networks in a variety of aspects (Graves & Schmidhuber 2005; Ihianle et al. 2020; Alharbi & Csala 2021). First, as I demonstrate in this study, they are excellent for tasks like timeseries forecasting, as well as speech recognition and language translation (Wöllmer et al. 2013; Graves & Jaitly 2014; Sundermeyer et al. 2014; Huang et al. 2018; Nammous et al. 2022) because they can capture long-term dependencies in the input sequence in both forward and backward directions. Second, unlike feedforward networks, BiLSTM networks do not demand fixed-length input sequences, thus being able to handle variable-length sequences better. Furthermore, by taking into account both past and future contexts, BiLSTM networks can handle noisy data. However, BiLSTM networks are computationally more expensive than regular LSTM networks due to the need for processing the input sequence in both directions. They also have a higher number of parameters and require more training data to achieve good performance.

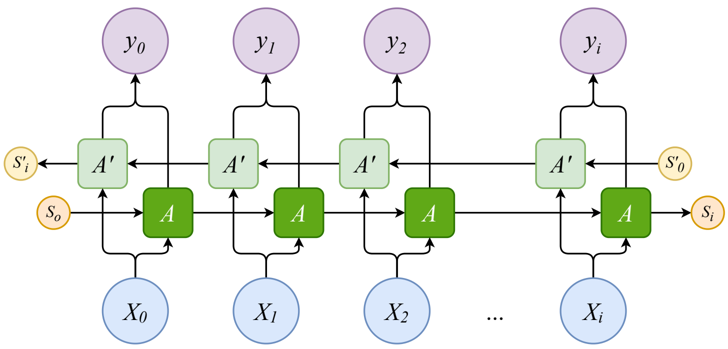


Figure 4.3: Architecture of a single BiLSTM layer. The blue circles at the bottom labeled by $(x_0, x_1, x_2, ..., x_i)$ are the input data values at multiple time steps. The purple circles, on the other hand, are the output data values at multiple time steps labeled by $(y_0, y_1, y_2, ..., y_i)$. The dark green and light green boxes are the activation units of the forward layer and the backward layer, respectively. The orange and yellow circles are the hidden states at the forward layer and the backward layer, respectively. Both the forward and backward layers composes a single hidden BiLSTM layer. The figure is adopted from Olah (2015)

The final dataset has 7 features, including the target feature, from December $25^{th}$ 1976 to July $30^{th}$ 2019, with a total of 15,558 samples (number of days). The training set has 11,558 samples, the validation set has 2,520 samples, and the test set has 1,480 samples.

The input horizon of 270 steps (30 days × 9 months) was used. A data batch size of 30 was used, which is the number of samples processed that result in one update to the model's weights (Appendix A.3.1). The model consists of 4 BiLSTM layers with 64 neurons each, and an output dense layer with 3 neurons, representing the output forecasting horizon. The total number of trainable parameters is 333,699. The number of training epochs was set to 50 because from experiments, the model stopped improving remarkably after almost 50 epochs. Thus, there was no need to waste time and computational resources to train the model for more than 50 epochs.

The *ModelCheckpoint* callback function was used to register the model version with the minimal validation loss. The *EarlyStopping* callback function was used to halt the model run when detecting overfitting, with a *patience* parameter of 7. *ReduceLROnPlateau* callback function was used to reduce the learning rate when the validation loss stops improving, with a *patience* parameter of 5, a reduction factor of 0.1 and minimal learning rate of $1e^{-6}$.

### Model Selection

To determine the most suitable model for our objective and provide justifiable reasons, I conducted the following analysis. First I examined the naive (persistence) model, which is very simplistic and assumes that the timeseries values will remain constant in the future. In other words, it assumes that the future value will be the same as the most recent historical value. That was the baseline. Next I examined the moving-average model, which calculates the future values based on the average value of historical data within a specific time widow. This gives a little bit lower error.


Figure 4.4: Illustration of the sliding window technique for a sample of 10 timesteps, where each number denotes a distinct time step. As an example here, the input horizon (blue color) length is 4 timesteps and the output horizon length is 3 timesteps. The input window slides 1 time step at a time across the entire data sequence to generate 4 distinct input and forecast horizon pairs. The purple, orange, and green colors of the output horizon represent 1-day, 2-day, and 3-day ahead forecasting, respectively. The timesteps of 1-day ahead forecasting across the data sequences are then concatenated into a single timeseries list that is called 1-day ahead prediction. The same for 2-day and 3-day ahead.

After that, I went towards the machine learning (ML)-based models. For all the ML models, I chose the Adaptive moment estimation (Adam) optimizer (Kingma & Ba 2015) as the optimization algorithm due to its minimal memory requirements and high computational efficiency as it is well-suited for applications that involve large number of parameters or large datasets. As a rule of thumb, I set the optimizer's learning rate to be 0.001 as it is usually recommended (**?**).

In order to prepare the data in a readable format to the ML models, I created a windowed dataset with an input horizon of 365 steps representing 1 year of data and an output horizon of 3 steps representing the forecast window of three days. I call this windowing method as Multi-Input Multiple Output (MIMO) strategy, in which the entire output sequence is predicted in one shot. The MIMO strategy adopts the sliding window method that was mentioned in Benson et al. (2020) in which each sequence is shifted by one step with respect to the previous sequence until reaching the end of the available data (Fig. 4.4). This approach minimized the imbalance of active days, with high SEP fluxes, and quiet days.

After experiments with different loss functions and evaluate their performance on our dataset, I chose the Huber function A.9a as the loss function and the Mean Absolute Error (MAE) is used as the metric function to monitor the model performance. I used the Huber function because it is robust and combines the advantages of both Mean Squared Error (MSE) and MAE loss functions. It is less sensitive to outliers than MSE, while still being differentiable and providing gradients, unlike MAE. Since our data is noisy and contains outliers that may negatively impact the model's performance, the Huber loss function is a good choice.

I examined various neural network models to determine the optimal architecture for our task. Initially, I started with a simple linear model comprising of a single layer with a single neuron. However, this model did not yield satisfactory results. I then explored a dense ML model consisting of two hidden layers,

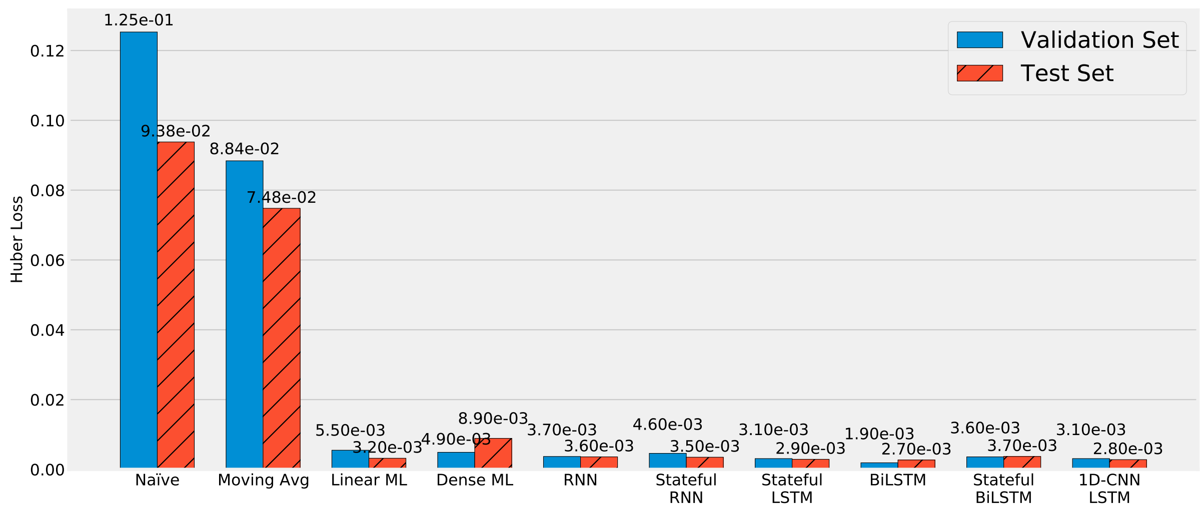


Figure 4.5: Benchmarking of 10 models, shows the Huber loss for the validation and test sets.

each with 32 neurons and a *RelU* activation function. Next, I experimented with a simple RNN model with the same number of hidden layers and neurons. To find the optimal learning rate, I utilized the *LearningRateScheduler* callback function and discovered that a rate of $1.58e^{-4}$ under the basic settings minimized the loss. I proceeded to examine stateful versions of RNN, LSTM, and BiLSTM models with three hidden layers, each with 32 neurons and a learning rate of $1.58e^{-4}$. In addition, I explored a hybrid model that consisted of a 1-dimensional convolutional layer with 32 filters, a kernel size of 5, and a *RelU* activation function. I combined this with a two-hidden layer LSTM network with 32 neurons each and a learning rate of $1.58e^{-4}$. I experimented with *Dropout* layers but did not observe any significant improvement in the results. Finally, I evaluated a BiLSTM model with five hidden layers, 64 neurons each, and a learning rate of 0.001. Based on the evaluation of all the models on both the validation and test sets (Fig. 4.5 and Table A.2), I selected the BiLSTM model for further refinement. More details on the final model architecture and hyperparameters are explained in the Appendix A.4. Figure 4.5 presents a comparative analysis of the Huber loss within the validation and testing sets across the ten aforementioned models. I used several evaluation measures to assess our models since each metric provides valuable insights into the accuracy and performance of the forecasts (Appendix A.3.2), helping to identify areas for improvement and adjust the forecasting models accordingly.

### 4.3.3 Results and discussion

**Long-term forecasting**

The benchmarking in Figure 4.5 showed that, in general, the ML-based methods were not much different. On the other hand, the persistence model and moving average model resulted in the highest errors compared with the ML-based models, and their results were close to some extent. As I see, the BiLSTM model performed the best over both the validation and test sets compared with the other models.

I developed and trained 3 BiLSTM models to forecast the integral flux of SEP, one model per energy channels. After the training was completed, I evaluated the performance of the models from the loss curve (Fig. 4.6) using the Huber loss (the left panel) and the metric MAE (the middle panel). During the training, the learning rate was reduced multiple times via the *LearningRateScheduler* callback function (the right panel). The left panel quantifies the discrepancy between the model's predictions and the true values over time. It shows how the Huber loss function changes during the training iterations (Epochs) for the training and validation sets for the three energy channels so that each channel has one color. The middle panel shows how the model's metric MAE changes with training epochs. It is used to evaluate the performance of the trained model by measuring the average absolute difference between the model's predictions and the true values, providing a single numerical value that indicates the model's error at a given epoch. The right panel shows how the learning rate of the model's optimizer changes with epochs via the *LearningRateScheduler* callback function, which changes the learning rate based on a predefined schedule to improve training efficiency and convergence. The learning rate refers to the rate at which the model's parameters are updated during the training process. I noticed that at the epochs where the learning rate has changed, there were bumps in the loss curves across all the energy channels, which is expected. This highlights the boundaries within which the learning rate yields better performance.

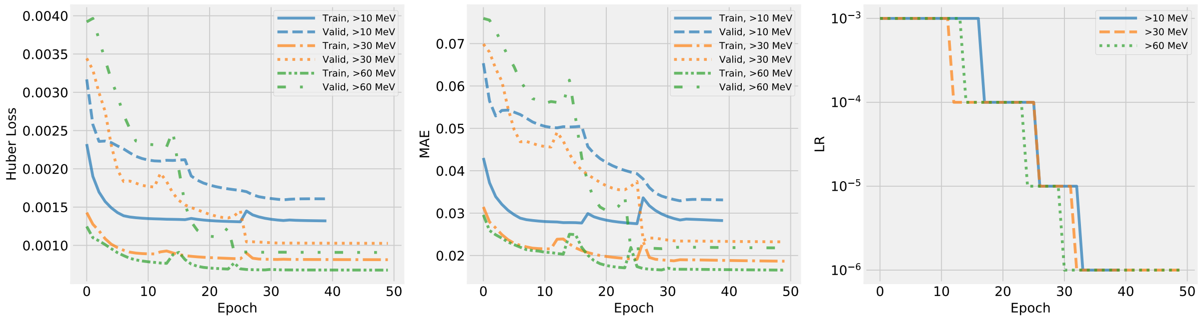


Figure 4.6: *Left Panel* - The Huber loss vs. the number of training epochs for the BiLSTM model for the validation and test sets, for the 3 energy channels. *Middle Panel* - The mean absolute error (MAE); the model's metric vs. the number of training epochs. *Right Panel* - Shows how the learning rate of the Adam optimizer changes over the number of epochs.

From experimentation, I found that the batch size and the optimizer learning rate are the most important hyperparameters that have a strong influence on the overall model's performance (Greff et al. 2016). In addition, adding *dropout* layers as well as varying the number of hidden layers and hidden neurons resulted in only marginal improvements to the final model performance, while substantially increasing training time and requiring greater computational resources.

The term *batch size* refers to the number of data sequences processed in one iteration during the training of a ML model (Goodfellow et al. 2016). Initially, a batch size of 64 was selected, however, I observed that the model produced better results when a batch size of 30 was used instead. This could be related to the Carrington rotation, which lasts for ∼27 days. There were ∼570 Carrington rotations between December $25^{th}$ 1976 and July $30^{th}$ 2019. Therefore, updating the model's weights after every Carrington rotation could be a reasonable choice for improving its performance. Figure 4.7 shows how good the model predictions are (on the y-axis) compared with the observations of the validation set (on the x-axis). The blue, orange, and gold colors refer to 1-day, 2-day, and 3-day ahead predictions, respectively. The top panel is for the >10 MeV channel, the middle panel is for the >30 MeV channel, and the bottom panel is for the >60 MeV channel. The left column is for the entire validation set, while the right column is for the observations points ≥10 proton flux units (pfu). That is the threshold value of proton flux as measured by the National Oceanic and Atmospheric Administration (NOAA) GOES spacecraft to indicate severity of space weather events caused by SEP.

I found that, overall, the models performed very well. The $R$ correlation was >0.9 for all points of the validation set across the forecasting windows for the 3 energy channels. The $R$ correlation was >0.7 for the observations points ≥10 pfu as well. However, the correlation between the modeled data and the observations exhibited a decline as the forecast horizon increased, in accordance with the anticipated result. To confirm the validity of the models, I performed the same correlation analysis between the modeled data and the observations of the out-of-sample test set (Fig. 4.8), which was not given to the model. Again, I found a high correlation across the forecasting windows for the 3 energy channels. The points were more dispersed between 1 and 1.5 on the x-axis, which reflected in a bit lower correlation. This might be a limitation in the current version of the model between that range of SEP fluxes since the models underestimated the flux values within that range across all energy channels, possibly due to the relatively smaller training samples with fluxes above 10 pfu compared with the majority of the data.

In order to see the temporal variation of the correlation between the modeled data and the observations, I applied a rolling window of 90 steps (3 months × 30 days/month = 1 season) that shows the seasonal variation of the correlation, as shown in Figure 4.9. Here, I show only the 1-day ahead predictions for the test set, for the 3 energy channels. I observe drops in the correlation factor synchronized with the transition between solar cycles (e.g., particularly between ∼1995-2000, which represents the declining phase of the solar cycle 22 and the rising phase of the solar cycle 23). This could be related to the fact that the low SEP fluxes during quiet times are more random and thus more difficult to forecast (Feynman et al. 1990; Gabriel et al. 1990; Rodriguez et al. 2010; Xapsos et al. 2012).

During periods of low solar activity, the forecasting of low SEP fluxes becomes more challenging due to their increased randomness. This difficulty arises from the reduced occurrence of conventional

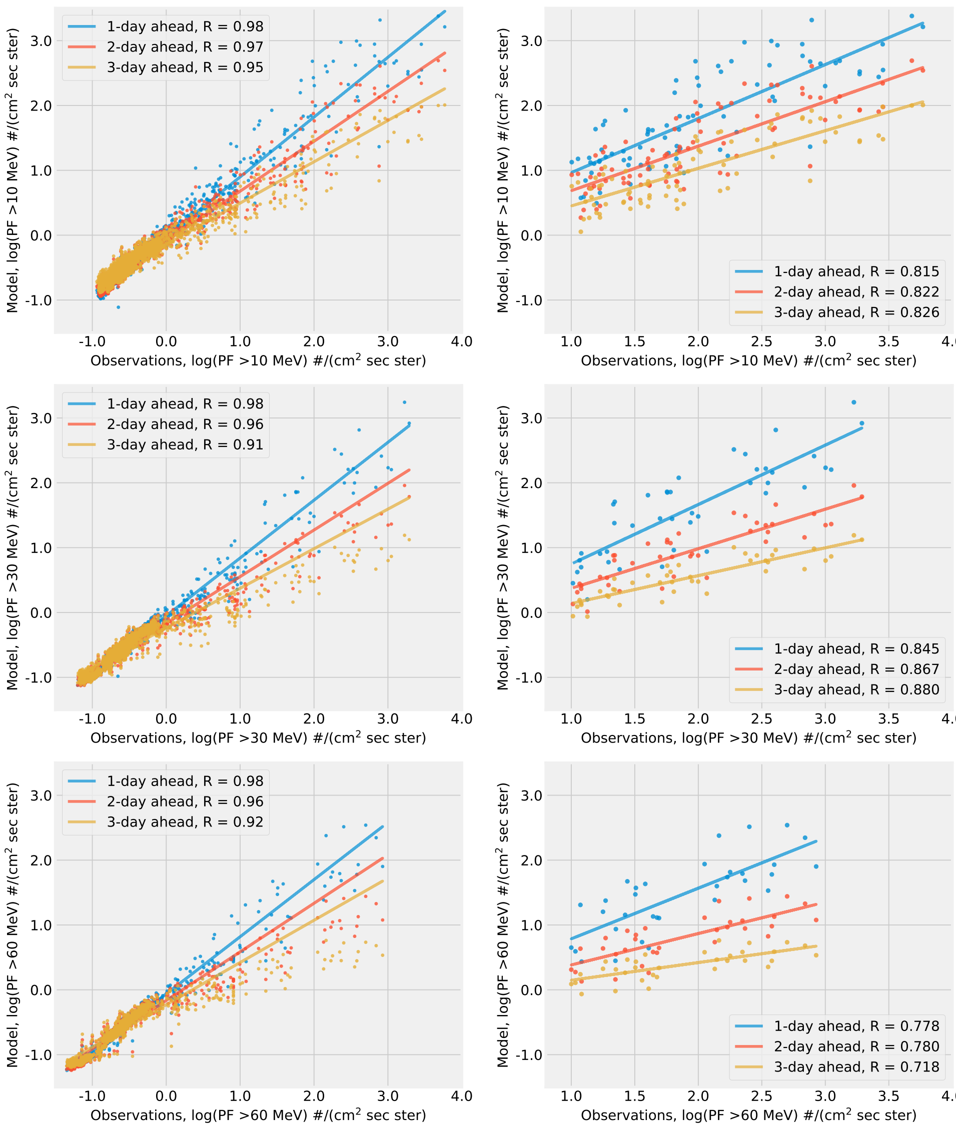


Figure 4.7: Correlation between the model predictions and observations for 1-day, 2-day, and 3-day ahead for >10 MeV (top panel), >30 MeV (middle panel), and >60 MeV (bottom panel). The panels in the left column represent all the points of the validation set, those in the right column represent all the observations points with daily mean flux ≥10 pfu.

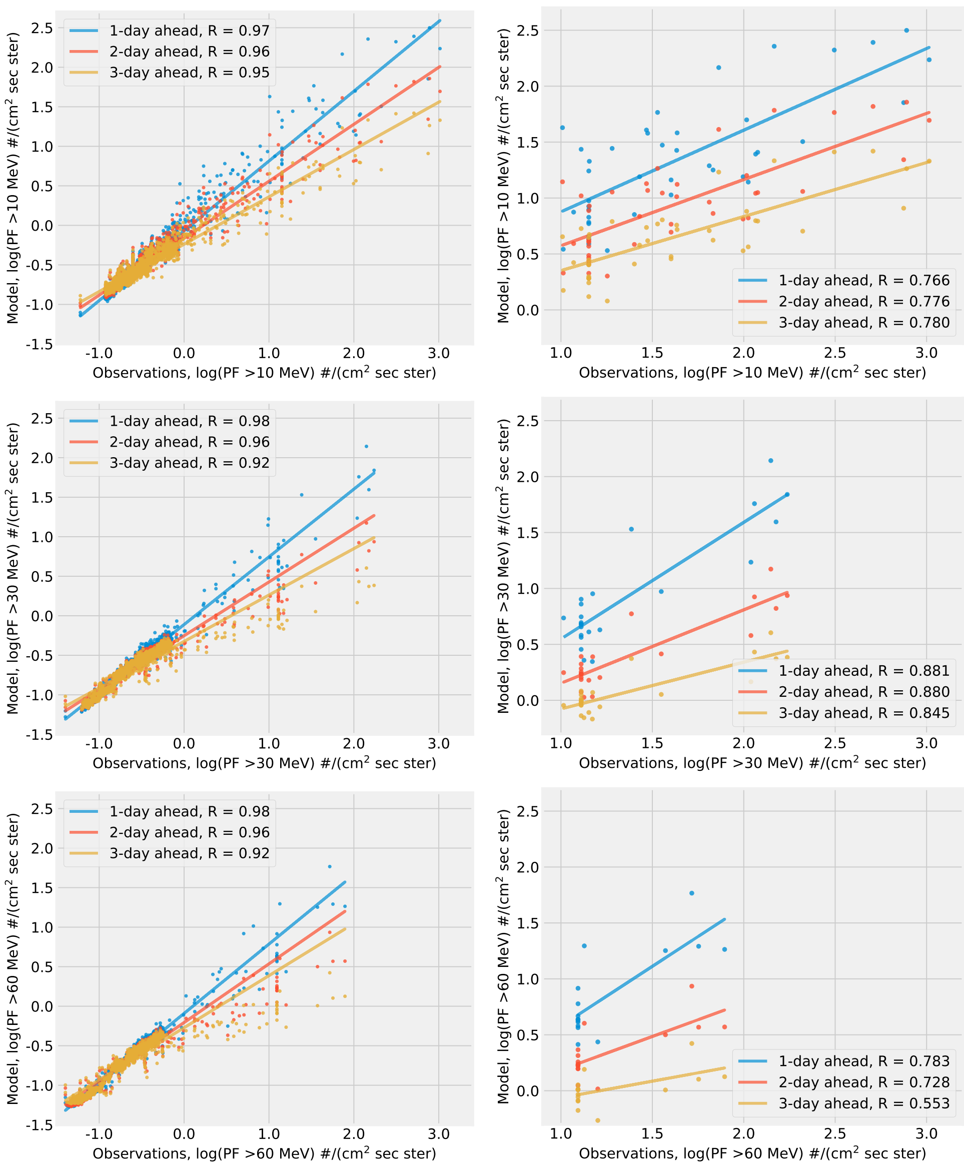


Figure 4.8: Same as Figure 4.7 but for the test set.

SEP drivers, such as solar flares and CMEs. Studies have suggested that the most significant solar eruptions tend to happen shortly before or after the solar cycle reaches its maximum (Švestka 1995). Additionally, sporadic increases in solar activity have been observed (Kane 2011), which might contribute to the diminished correlations observed in our research. There is clearly some factor that is influencing the correlation during certain periods where there are no or only weak SEP events. However, it is not obvious which physical phenomena are the cause rather than, for instance, some artifact of the data. Understanding the interplay between these factors and their influence on SEP fluxes during periods of reduced solar activity remains a critical area of research. It would be interesting to find what is reducing the correlations, thus more investigation is needed.

Overall, the modeled data was correlated the most with observations at >60 MeV, then the second rank was for the >10 MeV channel, and the third rank was for the >30 MeV channel. That could be related to the relatively larger extent of drops in correlation at the >30 MeV channel. The decline in correlation at the >30 MeV channel is consistent with the findings of Le & Zhang (2017). A summary of the performance results of the models for both the validation set and test set is presented in Table 4.1.

From the visual inspection of the test set examples (Fig. 4.10, 4.11, and 4.12), I found that the predicted onset time, the peak time, and end times of SEP events were highly correlated with those of the observations, which implies that the model captured the temporal variations, as well as the trends in SEP flux.

Table 4.1: Summary of the performance results of the models for the validation and test sets.

| | | | | | | | | | |
|---|---|---|---|---|---|---|---|---|---|
| **Validation Set** | | | | | | | | | |
| | log PF >10 MeV | | | log PF >30 MeV | | | log PF >60 MeV | | |
| Model Loss | 0.0016 | | | 0.0010 | | | 0.0009 | | |
| Model Metric | 0.0329 | | | 0.0232 | | | 0.0218 | | |
| | 1-Day | 2-Day | 3-Day | 1-Day | 2-Day | 3-Day | 1-Day | 2-Day | 3-Day |
| MAE | 0.061 | 0.091 | 0.125 | 0.053 | 0.079 | 0.098 | 0.052 | 0.069 | 0.086 |
| MSE | 0.013 | 0.028 | 0.054 | 0.010 | 0.031 | 0.055 | 0.009 | 0.027 | 0.047 |
| RMSE | 0.114 | 0.168 | 0.233 | 0.098 | 0.176 | 0.234 | 0.097 | 0.164 | 0.217 |
| MAPE | 22.156 | 28.104 | 34.721 | 13.039 | 18.590 | 22.735 | 10.036 | 13.994 | 16.731 |
| **Test Set** | | | | | | | | | |
| | log PF >10 MeV | | | log PF >30 MeV | | | log PF >60 MeV | | |
| Model Loss | 0.0014 | | | 0.0011 | | | 0.0010 | | |
| Model Metric | 0.0333 | | | 0.0283 | | | 0.0250 | | |
| | 1-Day | 2-Day | 3-Day | 1-Day | 2-Day | 3-Day | 1-Day | 2-Day | 3-Day |
| MAE | 0.072 | 0.099 | 0.125 | 0.053 | 0.088 | 0.107 | 0.045 | 0.066 | 0.081 |
| MSE | 0.015 | 0.030 | 0.050 | 0.009 | 0.029 | 0.048 | 0.007 | 0.020 | 0.034 |
| RMSE | 0.121 | 0.172 | 0.224 | 0.094 | 0.170 | 0.218 | 0.082 | 0.141 | 0.184 |
| MAPE | 30.135 | 37.498 | 48.139 | 20.599 | 34.300 | 40.803 | 12.358 | 20.504 | 25.305 |

To get further insight into the model's performance, I conducted an assessment of various skill scores, including True Positive (TP), True Negative (TN), False Positive (FP), and False Negative (FN). Additionally, skill score ratios such as Probability of Detection (POD), Probability of False Detection (POFD), False Alarm Rate (FAR), Critical Success Index (CSI), True Skill Statistic (TSS), and Heidke Skill Score (HSS). Detailed descriptions of these skill scores can be found in Appendix A.5. To extract individual SEP events from the test dataset, I implemented a threshold-based clustering algorithm. This algorithm uses the NOAA/SWPC warning threshold value of 10 pfu for the E $\geq$10 MeV channel. Upon analysis, I identified the number of detected SEP events for each output forecasting window and calculated the skill scores (Table 4.2). In the true test set, I identified 12 SEP events.

The evaluation of the model revealed notable trends as the length of the output forecasting window increased. The POD and CSI exhibited a declining pattern, indicating a reduced ability of the model to accurately detect and capture positive events (SEP occurrences) as the forecasting horizon extended further into the future. This suggests that the model's performance in identifying and capturing true positive instances diminishes with longer forecasting windows. Moreover, the POFD demonstrated an increasing trend, indicating an elevated rate of false positive predictions as the forecasting horizon lengthened. The model's propensity to generate false alarms rose with the lengthening forecasting window, leading to incorrect identification of non-events as positive events. Consequently, the TSS and HSS exhibited decreasing values, signifying a deterioration in the model's overall skill in accurately capturing

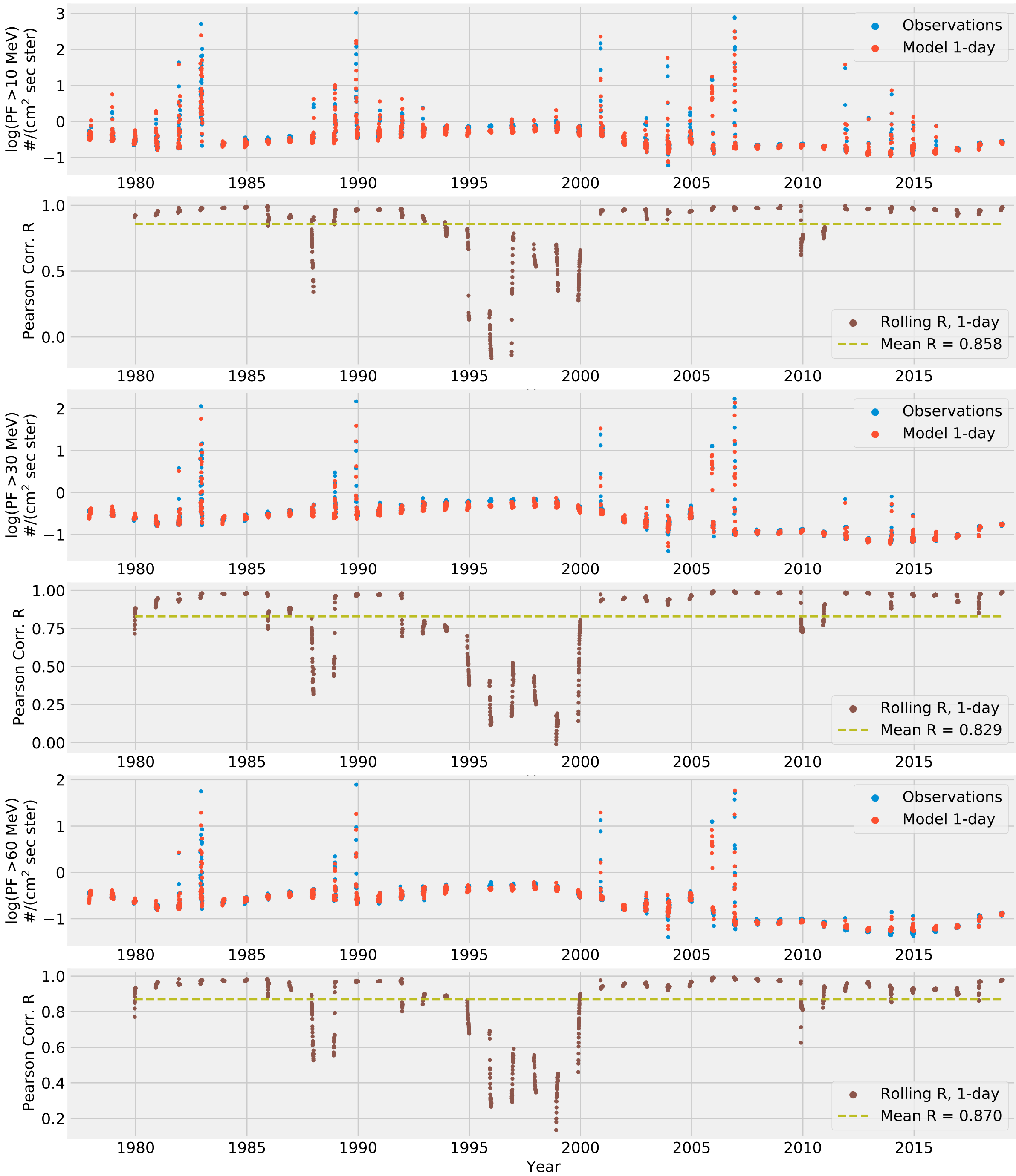


Figure 4.9: Comparison between the model outputs and observations of the test set for the 3 energy channels. In addition to the rolling-mean window correlation for 1-day ahead predictions.

and distinguishing between positive and negative instances. Overall, our skill scores are comparable with those reported by previous studies (Table 4.3). Although the UMASEP model does better than ours (i.e., has a higher POD), our FAR is much lower, thus, making fewer false alarms than the UMASEP model.

### Short-term forecasting

This work focuses on improving the prediction accuracy of the SEP integral flux, a critical aspect for mitigating the potential hazards posed by high-energy protons originating from the Sun. Expanding on previous work (Nedal et al. 2023a), the study utilizes a BiLSTM NN model, incorporating high-resolution

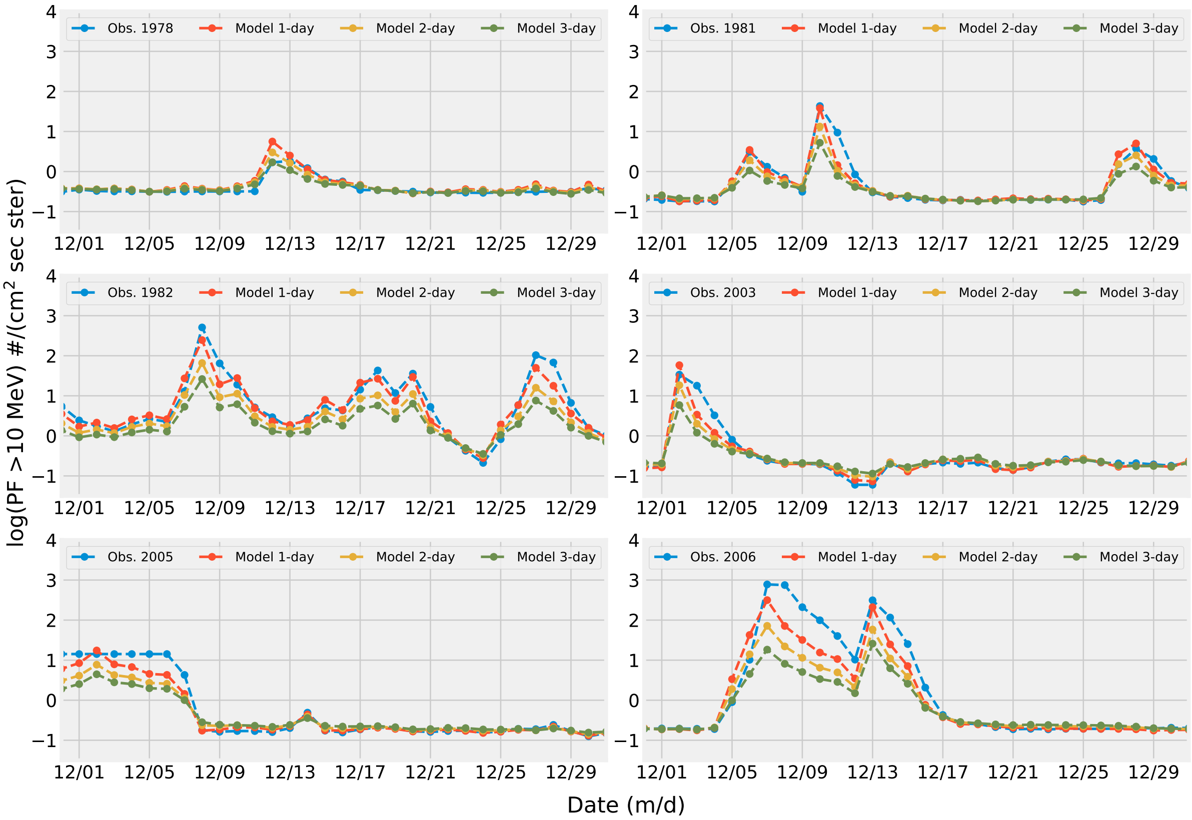


Figure 4.10: The model's forecasts for the out-of-sample testing set for the >10 MeV channel are shown at forecast horizons of 1 day, 2 days, and 3 days ahead, using samples of data from December in selected years mentioned in the top-left side of the plots.

Table 4.2: Confusion matrix for the energy channel ≥10 MeV predictions in the test set.

| E >10 MeV | No. events | TP | TN | FP | FN |
|---|---|---|---|---|---|
| 1-day ahead | 15 | 21 | 1441 | 2 | 13 |
| 2-day ahead | 13 | 14 | 1441 | 2 | 20 |
| 3-day ahead | 5 | 5 | 1443 | 0 | 29 |

Table 4.3: Comparing the skill scores with previous models. The dashed entries mean the data is unavailable (Whitman et al. (2023) for more details).

| Model | | POD | FAR | TSS | HSS | POFD | CSI | Accuracy | Precision |
|---|---|---|---|---|---|---|---|---|---|
| Our BiLSTM model | 1-Day | 0.618 | 0.087 | 0.531 | 0.732 | 0.001 | 0.583 | 0.99 | 0.913 |
| | 2-Day | 0.412 | 0.125 | 0.287 | 0.553 | 0.001 | 0.389 | 0.985 | 0.875 |
| | 3-Day | 0.147 | 0 | 0.147 | 0.252 | 0 | 0.147 | 0.980 | 1 |
| UMASEP-10 (Núñez 2011) | | 0.822 | 0.219 | — | — | — | — | — | — |
| PCA (Papaioannou et al. 2018) | | 0.587 | 0.245 | — | 0.65 | — | — | — | — |
| SPARX (Dalla et al. 2017) | | 0.5 | 0.57 | — | — | 0.32 | 0.3 | — | — |
| SPRINTS (Engell et al. 2017) | | 0.56 | 0.34 | — | 0.58 | — | — | — | — |
| REleASE (Malandraki & Crosby 2018) | | 0.63 | 0.3 | — | — | — | — | — | — |

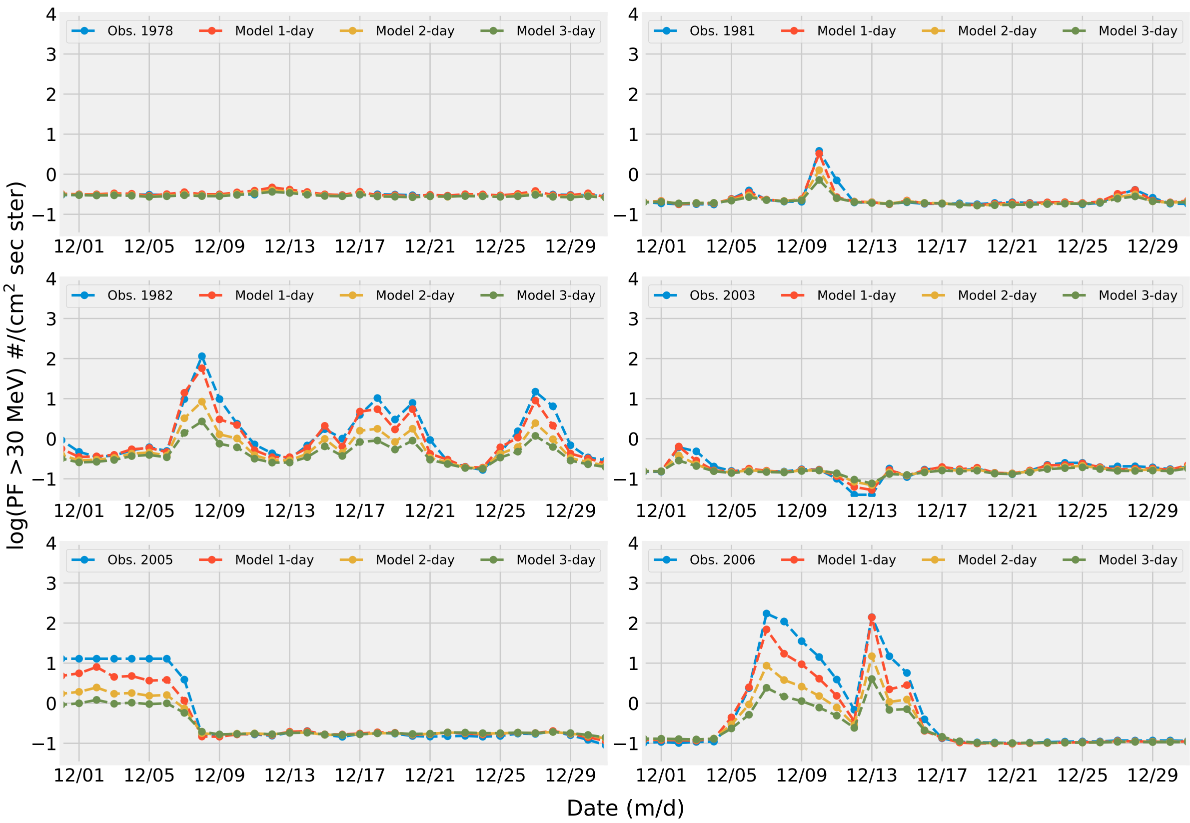


Figure 4.11: The model's forecasts for the out-of-sample testing set for the >30 MeV channel are shown at forecast horizons of 1 day, 2 days, and 3 days ahead, using samples of data from December in selected years mentioned in the top-left side of the plots.

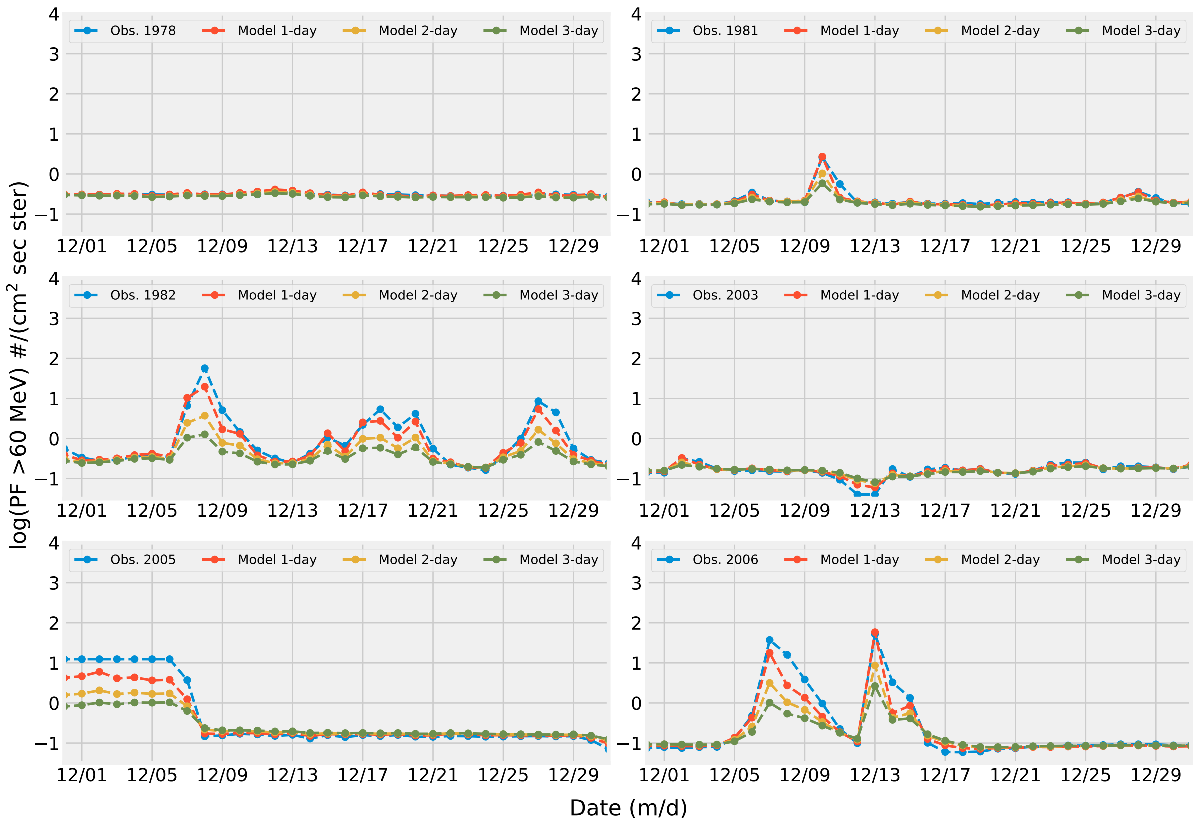


Figure 4.12: The model's forecasts for the out-of-sample testing set for the >60 MeV channel are shown at forecast horizons of 1 day, 2 days, and 3 days ahead, using samples of data from December in selected years mentioned in the top-left side of the plots.

hourly-averaged data for four standard integral GOES channels.

So far, the forecasting models, developed with 6-hour forecast window, integrate key input parameters such as the F10.7 index, sunspot number, x-ray flux, solar wind speed, and IP magnetic field strength, obtained from the OMNIWeb and GOES databases, spanning two solar cycles. Additional features, including the location of active regions obtained from the NOAA daily reports, are introduced to enhance predictive capabilities.

Rigorous evaluation involves independent out-of-sample testing, quantifying the impact of different features on prediction results, and benchmarking against existing approaches. This comprehensive approach contributes to advancing our ability to forecast SEP flux and better understand its implications for space weather.

I employed the 9-2-1 strategy to partition the data, allocating 9 months to the training set, 2 months to the validation set, and 1 month to the test set for each year. This approach spans the 23-year period from January 1996 to December 2018, resulting in 73.99% of the data for the training set, 16.44% for the validation set, and 9.57% for the testing set. To facilitate model training, we formatted the data using the MIMO strategy, predicting the entire output sequence in one iteration (Benson et al. 2020). The model forecasts the logarithm of the integral proton flux, encompassing various energy channels. However, for clarity in our poster, I specifically present results for the >10 MeV channel.

Figure 4.13 illustrates the temporal correlation across six future windows, with Figure 4.14 providing a visual representation through a scatter plot. Additionally, Figure 4.15 showcases the variation in prediction errors across these windows. For a more detailed examination, Figure 4.16 compares our model's 1-hour predictions with observations specifically for two sample SEP events in the >10 MeV channel.

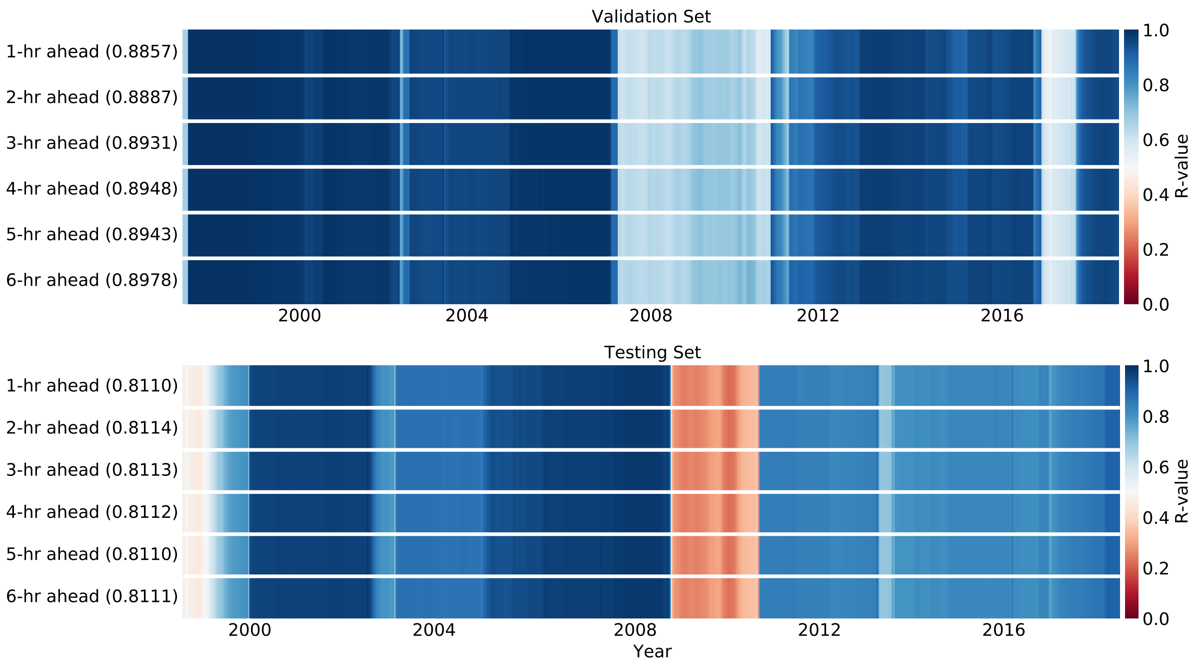


Figure 4.13: Temporal heatmap shows a comparison between the model outputs and observations for the rolling-mean window correlation of the integral >10 MeV proton flux at six predicting windows. The top panel represents the validation set and the bottom panel represents the testing set. The numbers on the y-axis are the mean R values.

Table 4.4: The MSE/MAE for the validation and test sets over six forecasting windows.

| | 1-hr | 2-hr | 3-hr | 4-hr | 5-hr | 6-hr |
|---|---|---|---|---|---|---|
| Valid. Set | 0.078/0.238 | 0.086/0.254 | 0.091/0.263 | 0.098/0.273 | 0.102/0.280 | 0.115/0.299 |
| Test Set | 0.012/0.080 | 0.012/0.079 | 0.012/0.080 | 0.011/0.079 | 0.011/0.080 | 0.011/0.079 |

Predicting SEPs remains a complex task due to their non-linear nature. This study, however, demonstrates promise by utilizing BiLSTM NNs. These models effectively captured the intricate patterns

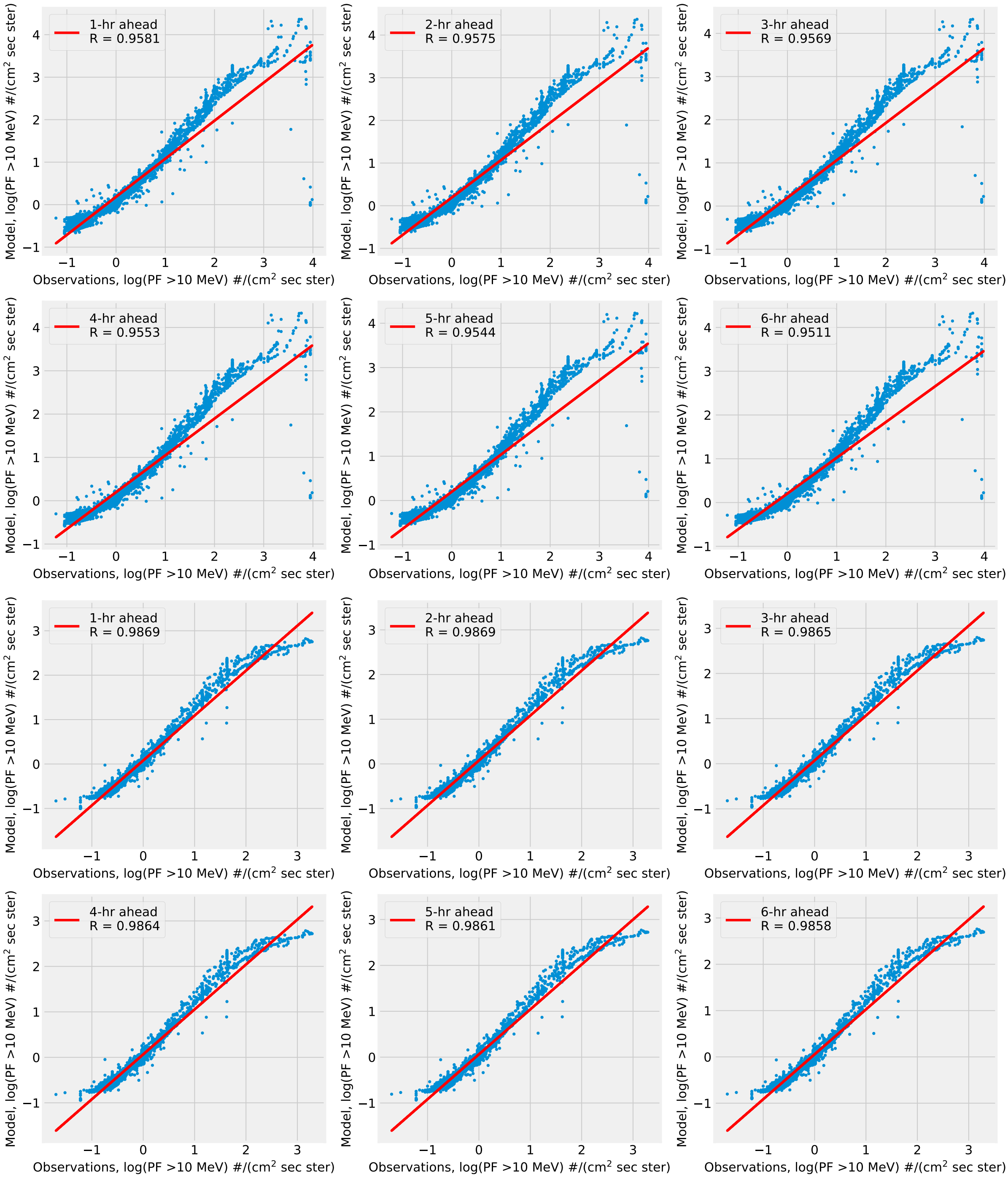


Figure 4.14: Correlation between model predictions and observations for the integral >10 MeV proton flux of the validation (top two rows) and testing (bottom two rows) sets.

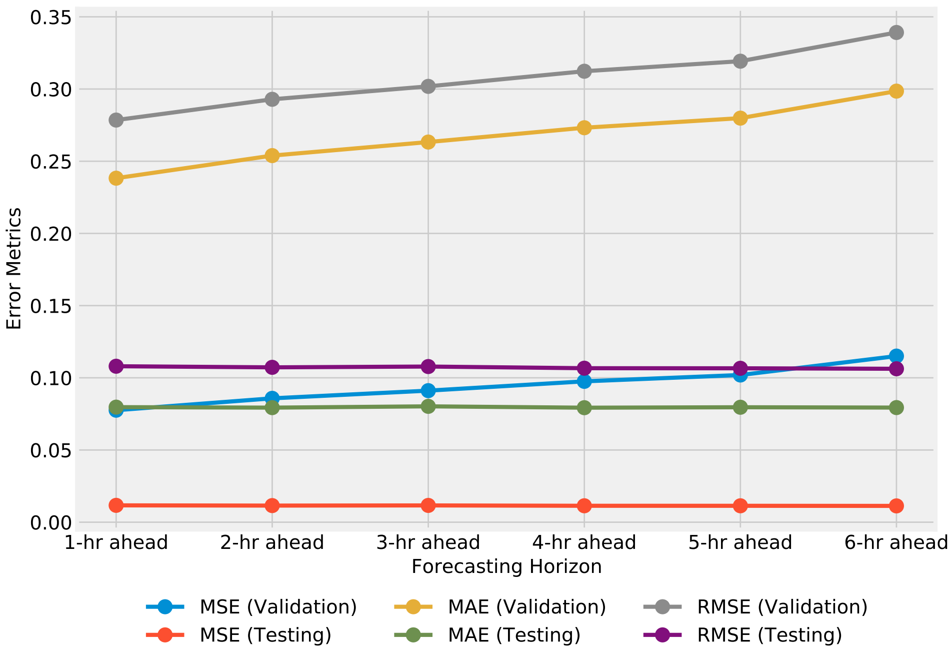


Figure 4.15: Correlation between model predictions and observations for the integral >10 MeV proton flux of the testing set.

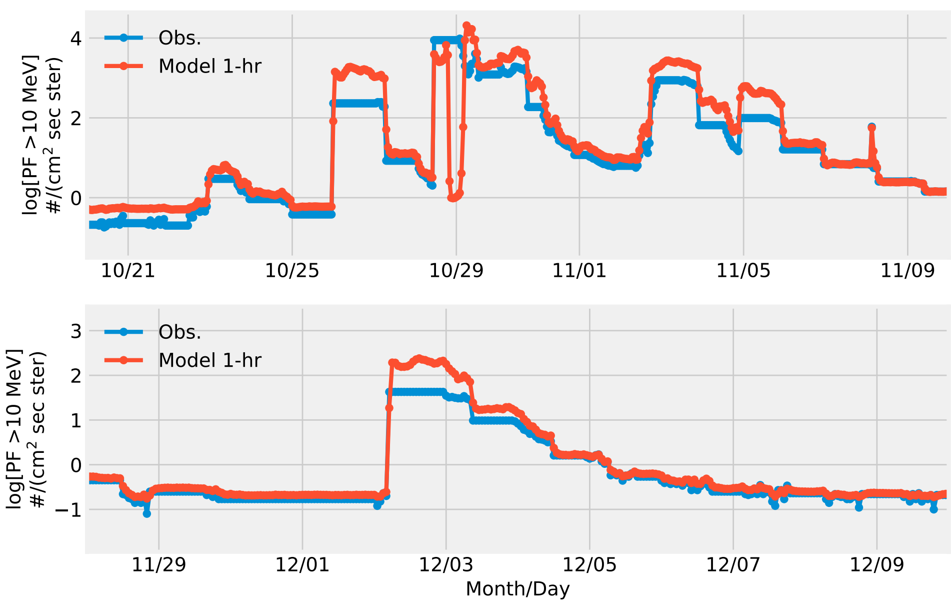


Figure 4.16: Comparison between the model's forecast and the observations for the integral >10 MeV proton flux at forecast horizon of 1 hour ahead. The top panel represents a sample of the validation set and the bottom panel represents a sample of the testing set.

within SEP data, leading to successful hourly-averaged integral flux predictions across various energy channels. The model exhibited robust performance with low MSE values ranging from 0.011 to 0.012 in the test set. However, challenges remain, particularly during solar minimum phases, highlighting the inherent complexity of SEP prediction. Despite this, BiLSTM networks showcase significant potential for time series forecasting in heliophysics, especially when considering sequential data. Moving forward, we aim to optimize the model by fine-tuning parameters and benchmarking it against established methods. Additionally, extending the forecasting window and incorporating more energy channels with differential energy forecasting will offer a more comprehensive analysis and improve model interpretability.

## 4.4 Conclusions

In Kozarev et al. (2022) we represents a pioneering multi-event exploration, presenting a comprehensive examination of Sun-to-1 AU SEP simulations grounded in detailed coronal diffusive shock acceleration and interplanetary propagation—a unique endeavor within the current body of knowledge. Investigating 62 distinct eruptive events, each characterized by an EUV CBF and notable enhancements in 1 AU proton fluxes, our approach utilized the SPREAdFAST framework. This framework, originally designed for forecasting early-stage SEP events, demonstrated its efficacy in the analysis of this extensive event set.

The input spectra for coronal proton acceleration were derived from quiet-time suprathermal spectra averaged over one to three days preceding each event. These averages were then scaled back to the Sun, assuming a simple inverse square proportionality to heliospheric distance. Utilizing an energy-independent mean free path for coronal proton acceleration in the diffusive shock acceleration model, we observed significant influences of solar corona conditions on proton acceleration. The gradients in plasma parameters among neighboring streamers, quiet-Sun regions, and coronal holes induced continuous changes in the $\theta_{BN}$ angle along the shock wave surface, as well as in density and density enhancements.

The results from the DSA model, serving as time-dependent input to the interplanetary transport EPREM model, were compared with in situ observations by the SOHO/ERNE instrument at 1 AU. The overall alignment between model predictions and observations is promising, affirming the efficiency and accuracy of the SPREAdFAST model chain. Nevertheless, discrepancies, particularly at the highest energies, were observed, mainly attributed to variations in the slope of increase and onset times.

To address these discrepancies and enhance model precision, future work will delve into more realistic modeling of events. This includes exploring time-dependent injection of source spectra at the inner boundary of the EPREM simulation to better match observed decay rates. Acknowledging the importance of three-dimensional transport effects in realistic interplanetary magnetic fields, perpendicular transport will be incorporated in subsequent investigations. Furthermore, introducing location-dependent output to accommodate varying connectivity between the source and observer will be explored.

The integration of geometric shock models with existing and novel observations of CME evolution in the middle corona is anticipated to reduce uncertainties in the results. Ongoing efforts involve comparing near-Sun in situ observations of quiet-time suprathermal populations from the Parker Solar Probe and Solar Orbiter with 1 au fluxes, aiming to refine the estimation of input spectra. This holistic approach contributes to advancing our understanding of SEP dynamics, paving the way for more accurate modeling and forecasting capabilities in the realm of solar-terrestrial physics.

Forecasting the SEP flux is a crucial task in heliophysics since it affects satellite operations, astronaut safety, and ground-based communication systems. It is a challenging task due to its non-linear, non-stationary, and complex nature. Machine learning techniques, particularly neural networks, have shown promising results in predicting SEP flux. In Nedal et al. (2023a) I developed and trained BiLSTM neural network models to predict the daily-averaged integral flux of SEP at 1-day, 2-day, and 3-day ahead, for the energy channels >10 MeV, >30 MeV, and >60 MeV. I used a combination of solar and interplanetary magnetic field indices from the OMNIWeb database for the past 4 solar cycles as input to the model. I compared the models with baseline models and evaluated them using the Huber loss and the error metrics in Appendix A.3.2.

The data windowing method I used, based on the MIMO strategy, eliminates the need to feed the output forecast as input back into the model and that allows to do forecasting relatively far into the future while maintaining decent results (e.g., the MSE is ranging between 0.007 and 0.015 for 1-day forecasting in the test set, compared to an MSE of 0.236 for a persistence model. See Table 4.1). The results show that the model can make reasonably accurate predictions given the difficulty and complexity of the problem. The MSE was ranged between 0.009 and 0.055 for the validation set, and between 0.007 and 0.05 for the test set. The correlations between the observations and predictions were >0.9 for the validation and test sets (Fig. 4.7 and Fig. 4.8). Nevertheless, the mean temporal correlation was $\sim$0.8 for the test set (Fig. 4.9). Although our models performed well, I observed a relatively large discrepancy between the predictions and the observations in the >30 MeV energy band.

The findings of this study underscore the challenges encountered by the forecasting model in accurately predicting SEP data over longer time periods. As the length of the output forecasting window increased, the model's ability to detect true positives and its overall skill in differentiating positive and negative instances diminished. Additionally, the model displayed an elevated rate of false negative predictions, indicating an increased tendency to generate misses as the forecasting horizon extended. These results highlight the importance of carefully considering the appropriate forecasting window length for SEP data to ensure the model's optimal performance. Our skill scores generally align with those from previous works (Table 4.3). There are variations in the metrics' values across different studies, highlighting the complexities and nuances associated with each study. Nevertheless, it is important to acknowledge that the statistical significance of the results in this study is limited due to data averaging. Future studies should consider incorporating hourly data, as this is likely to result in a greater number of identified events. The model can provide short-term predictions, which can be used to anticipate the behavior of the near-Earth space environment. These predictions have important implications for space weather forecasting, which is essential for protecting satellites, spacecraft, and astronauts from the adverse effects of solar storms.

Multiple techniques exist for identifying the optimal combination of hidden layers and neurons for a given task such as empirical methods, parametric methods, and the grid search cross-validation method, which I will explore in future work. The observed reduction in correlation necessitates further investigation to determine its origin, whether stemming from tangible causal factors or potential aberrations within the model or data. I plan to expand upon this work by performing short-term forecasting using hourly-averaged data. This extension will involve integrating additional relevant features such as the location and area of active regions and coronal holes on the Sun.

BiLSTM networks are particularly useful for tasks involving sequential data such as timeseries forecasting. Given their capacity to handle input sequences in both directions in time and capture long-term dependencies, they are valuable in a broad range of applications. Nonetheless, one should carefully consider their data requirements and computational complexity before adopting them. Our results emphasize that the use of deep learning models in forecasting tasks in heliophysics are promising and encouraging, as pointed out by Zhang et al. (2022b).

This work is a stepping stone towards real-time forecasting of SEP flux based on the public-available datasets. As an extension, I are currently working on developing a set of models that deliver near-real time prediction of SEP fluxes at multiple energy bands, multiple forecasting windows, with hourly-averaged data resolution, with a more sophisticated model architecture, as well as more features that address the state of solar activity more comprehensively. I plan to extend the analysis to include more recent data from solar cycle 25, in order to improve the accuracy of the models. In conclusion, our study highlights the potential of using BiLSTM neural networks for forecasting SEP integral fluxes. Our models provide a promising approach for predicting the near-Earth space environment too, which is crucial for space weather forecasting and ensuring the safety of our space assets. Our findings contribute to the growing body of literature on the applications of deep learning techniques in heliophysics and space weather forecasting.

# Chapter 5

# Summary

In this final chapter, I present a comprehensive summary of the key findings from the dissertation's chapters, providing insights into the analysis of EUV waves, solar type III bursts, and SEP modeling and forecasting. The exploration of CBFs and the introduction of the Wavetrack tool have significantly contributed to our nuanced understanding of solar dynamics. As we look towards the future, the extension of the CBF dataset promises deeper insights into their kinematics, while the utilization of multi-wavelength observations from LOFAR, PSP, and Solar Orbiter aims to unravel the origin and evolution of energetic particles in the solar corona. Furthermore, the development of interpretable deep learning models, driven by higher resolution data, holds the key to advancing SEP forecasting capabilities. These future endeavors underscore the commitment to refining models, incorporating advanced data analysis techniques, and leveraging cutting-edge observational tools to unlock new dimensions in our comprehension of space weather phenomena.

Chapter 2 centered on the analysis of base-difference images obtained from the SDO/AIA instrument to investigate EUV waves. Key kinematic parameters, including shock speed, acceleration, intensity, and thickness, were computed. SOHO/LASCO measurements up to 17 $R_\odot$ were incorporated to enhance the understanding of shock plasma parameters. Kinematic measurements played a pivotal role in generating 3D geometric models of wavefronts and informing plasma diagnostics using MHD and DEM models. The use of shock kinematic measurements facilitated the fitting of geometric spheroid surface models. Parametrized relationships between plasma parameters were explored to uncover connections and interdependencies. The study also introduced Wavetrack, an automated tool for identifying and monitoring dynamic coronal phenomena. Its application to CBF events revealed proficiency in tracking complete pixel maps, aiding in understanding CBF evolution. Limitations were acknowledged, and future work will address them for enhanced versatility. The methodology holds promise for extensive application in solar dynamic features and observational datasets.

Chapter 3 delved into the analysis of type III bursts during the second near-Sun encounter period of PSP. Sixteen separate radio bursts were observed using the PSP/FIELDS instrument and LOFAR ground-based telescope. A semi-automated pipeline facilitated data analysis, alignment, and interferometric imaging. Uniform frequency drifts among bursts suggested related origins. Interferometric observations located type III emissions off the southeast limb of the Sun, hinting at a single source of electron beams low in the corona. Magnetic extrapolation favored the active region AR12737 as the source, aligning with previous studies. However, caution was advised regarding potential deviations in magnetic field configurations near active regions. The study also explored discrepancies in observed and modeled density profiles, attributing them to scattering and propagation effects. Future work will integrate TDoA technique and Solar Orbiter observations for a more comprehensive analysis of solar radio bursts.

The pioneering multi-event exploration in Chapter 4 focused on Sun-to-Earth SEP simulations, investigating 62 eruptive events with EUV CBFs. The SPREAdFAST framework was employed to analyze coronal diffusive shock acceleration and interplanetary propagation. Input spectra for coronal proton acceleration were derived from quiet-time suprathermal spectra, exhibiting influences of solar corona conditions on proton acceleration. Comparison with in situ observations demonstrated overall alignment, validating the efficiency of the SPREAdFAST model. Discrepancies at the highest energies were noted, prompting future work to refine modeling and incorporate three-dimensional transport effects. The study also introduced a BiLSTM neural network model for forecasting SEP integral flux at 1 AU, showcasing promising results for short-term predictions with implications for space weather forecasting.

In conclusion, the dissertation contributions include a nuanced understanding of EUV waves, an automated tool for tracking coronal phenomena, insights into type III bursts and their sources, and advancements in SEP simulations and forecasting using deep learning. Future directions involve addressing limitations, refining models, and incorporating more recent data for a comprehensive understanding of solar dynamics and space weather forecasting.

## 5.1 Future Work

The quest to understand the Sun's ever-changing nature continues. Future research in heliophysics holds immense potential to expand our knowledge and improve space weather forecasting.

One crucial area lies in expanding the data pool for EUV waves. By studying EUV waves observed throughout various solar cycle phases, we can investigate how the Sun's cyclical activity influences their behavior. Similarly, incorporating a broader range of active regions with diverse magnetic configurations into the analysis of solar radio bursts will be key. This will provide a more comprehensive picture of their characteristics across different solar activity levels.

The next leap forward hinges on leveraging multi-wavelength observations. Instruments like LOFAR, Parker Solar Probe, and Solar Orbiter, each providing data at different wavelengths, will be instrumental. By combining these views, we can gain a deeper understanding of how energetic particles and radio bursts originate and evolve within the solar corona. Additionally, incorporating high-resolution data will allow for a more detailed and accurate representation of the dynamic processes at play.

Furthermore, future studies should account for the impact of scattering and propagation phenomena on both SEPs and radio burst observations. Refining models to account for these effects will significantly enhance their accuracy for forecasting purposes.

Beyond data granularity, expanding the features used in SEP prediction models is crucial. Including characteristics of active regions, for example, could provide a more nuanced forecasting capability. Additionally, the implementation of advanced interpretable deep learning architectures holds promise for enhancing model reliability and reducing forecasting errors.

The ultimate goal lies in developing real-time analysis tools for space weather forecasting. These tools will integrate data from newly commissioned instruments and spacecraft, coupled with the incorporation of advanced methodologies. By refining our understanding of solar dynamics and improving the accuracy of predictive models, we can ultimately provide early warnings and more accurate risk assessments for space weather events.

# Appendix A

## A.1 Persistent Imaging Technique

Persistent imaging is a technique used in medical imaging, particularly ultrasound imaging, to create a continuous, real-time display of the anatomy being imaged (see Pysz et al. 2011, and references within). The core idea of persistent imaging is to use persistence, or the ability of the human eye to retain an image for a brief moment after it has disappeared to create a more informative and visually clear image (Fredkin et al. 1995; Thompson & Young 2016).

At every image in a time-ordered series, the technique keeps the old pixel value if it is brighter than the current pixel value, else it takes the current pixel's value. The result is saved as the current persistence image. Then, the next image in the series is evaluated by comparing it pixel by pixel with respect to the previous persistence image. The resulting image emphasizes the changes between the current image and the previous persistent image, making them more visible to the human eye.

The persistent imaging technique can be described mathematically by a set of equations. If we let $I(t, x, y)$ be the intensity at time $t$ and pixel coordinates $(x, y)$, and let $P(t, x, y)$ be the persistence image at time $t$ and pixel coordinates $(x, y)$, then the persistence image at time $t$ is computed as:

$$P(t, x, y) = max\{I(t, x, y), P(t-1, x, y)\}, \tag{A.1}$$

where **max** represents the maximum of its two arguments. The current image at time $t$ is then evaluated with respect to the previous persistence image as follows:

$$I^{`}(t, x, y) = max\{I(t, x, y) - P(t-1, x, y), 0\}, \tag{A.2}$$

The resulting image $I'(t, x, y)$ is a modified version of the current image that emphasizes the differences from the previous persistence image.

The persistent imaging technique has been shown to improve the visual quality of ultrasound images and other medical imaging modalities, and is commonly used in clinical practice. In this work, I utilize the persistent imaging technique to improve the visualization of the solar radio sources of type III emissions (Fig. 3.6).

## A.2 Resolving the radio emission location ambiguity

In this part, we show that the -Z solution of Equation **??** is highly unlikely in our case. Figure A.1 shows the positive and negative solutions of Equation **??**. I take the innermost and outermost coronal radio sources at $R_1$ and $R_2$, respectively, as an example. $r_1$ and $r_2$ are the projections of $R_1$ and $R_2$ on the POS, respectively. Harmonic radio emission from $R_1$ will theoretically be absorbed by a region along the LOS with plasma frequency (and corresponding density) equal to or higher than the harmonic emission frequency at $R_1$. In the case of the spherically symmetric Newkirk model, the highest density location the emission from $R_1$ could pass through is $r_1$ on the POS. Thus, for harmonic radio emission from behind the POS (-Z, where Z = 0 is defined at the center of the Sun and positive Z is towards the observer) to be observed at the Earth, it must satisfy the following condition:

$$2f_{R_1} > f_{r_1}, \tag{A.3}$$

where $f_{R_1}$ is the plasma frequency of radio emission that occurred behind the POS, and $f_{r_1}$ is the plasma frequency at the projected location of $r_1$ on the POS. The relation between the local plasma frequency and the electron density is defined by the equation:

$$f[MHz] = 8.93 \times 10^{-3} \sqrt{n[cm^{-3}]}. \tag{A.4}$$

The Newkirk electron-density model (Newkirk 1961, 1967) describes the typical densities in the outer part of the corona according to the following equation:

$$n[cm^{-3}] = \alpha \, 4.2 \times 10^4 \, 10^{4.32 \frac{R_\odot}{r}}, \tag{A.5}$$

where $\alpha$ is the fold number (i.e., a multiplicative factor that accounts for the density variations based on the degree of solar activity), and $r$ is the radial distance from the Sun in solar radii. By substituting Equations A.4 and A.5 into Equation A.3, we obtain

$$\frac{n_{r_1}}{n_{R_1}} = \frac{10^{4.32 \frac{R_\odot}{r_1}}}{10^{4.32 \frac{R_\odot}{R_1}}} < 4. \tag{A.6}$$

After reduction we obtain the final formula that must be satisfied under these assumptions in order for radio emission behind the POS to pass through the corona and reach the Earth:

$$\frac{r_1}{R_\odot} < \left( \frac{log2}{2.16} + \frac{R_\odot}{R_1} \right)^{-1}. \tag{A.7}$$

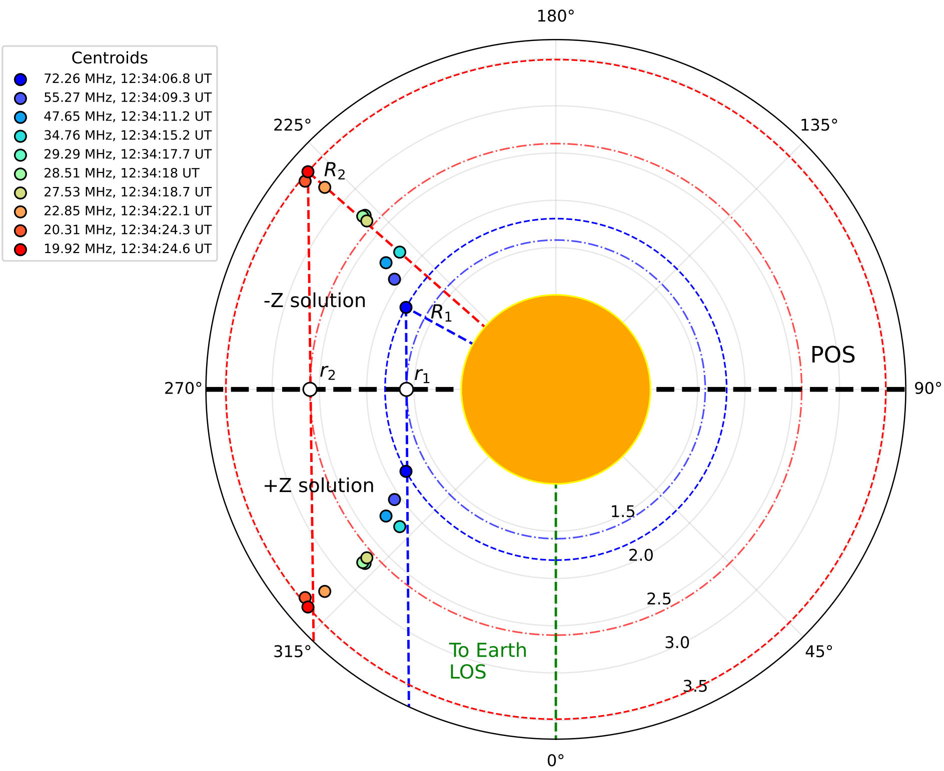


Figure A.1: Schematic shows the locations of the radio sources for the +Z and -Z solutions of Equation ??. The Sun is located in the middle as an orange circle, with a horizontal dashed black line representing the POS. The vertical dashed green line represents the Sun-Earth LOS. The dashed blue and red circles represent the plasma spheres of density equivalent to the observation frequencies of the innermost and outermost radio sources at $R_1$ and $R_2$, respectively, under the Newkirk model assumption of spherically-symmetric density distribution. The impact parameters $r_1$ and $r_2$ are the projection of $R_1$ and $R_2$ on the POS. The dot-dashed blue and red circles are the circles passing through the impact parameters $r_1$ and $r_2$, respectively.

From Figure A.1, $r_1$ and $r_2$ will always be smaller than $R_1$ and $R_2$, respectively. The Newkirk model requires that the density at $r_1$ and $r_2$ be significantly higher than the density at $R_1$ and $R_2$, respectively

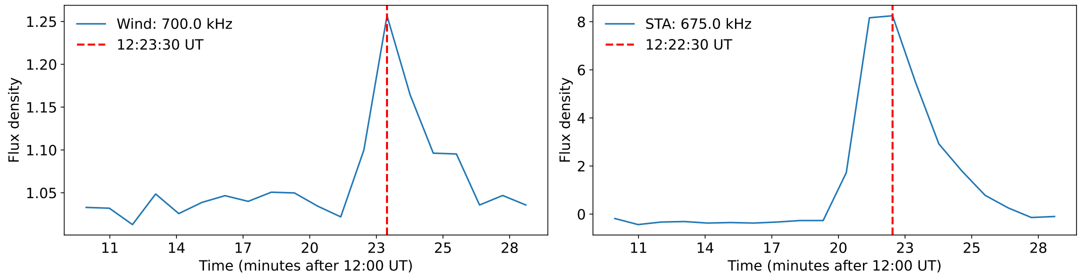


Figure A.2: Cut of the flux density at 700 kHz observed by Wind (left panel) and STEREO-A (right panel). Note: for STEREO-A, there is no exact frequency channel at 700 kHz; therefore we selected the nearest one (675 kHz).

(Table A.1). Additionally, from the geometric representation in Figure A.1, we find that the electron density at $r_1$ is higher than at $R_1$, hence the radio emission cannot reach the Earth from that point behind the POS (Mann, G. et al. 2018).

From Table A.1, the assumption of Equation A.6 is not satisfied. Thus, the -Z solution is invalid in our case. This implies that the harmonic emission from behind the POS will not reach the Earth. Thus, the +Z assumption is the valid solution.

Table A.1: Radial distances and densities at the first ($R_1$) and last ($R_2$) radio sources were obtained from the 2.5×Newkirk model, as well as their impact parameters $r_1$ and $r_2$, respectively.

| Point | Radial distance ($R_\odot$) | Density (cm$^{-3}$) | Ratio ($n_r/n_R$) |
|---|---|---|---|
| $r_1$ | 1.58 | 5.69×10$^7$ | 11.81 |
| $R_1$ | 1.81 | 4.82×10$^6$ | |
| $r_2$ | 2.6 | 2.59×10$^7$ | 14.23 |
| $R_2$ | 3.49 | 1.82×10$^6$ | |

Furthermore, I analyzed the time difference of arrival of the radio emission at interplanetary wavelengths in Figure A.2. Specifically, we compared the timing of peak signals at a low frequency between two spacecraft, Wind and STEREO. This analysis was conducted under the assumption of two possible scenarios:

- one in which the radio emission source follows a trajectory that is roughly equidistant between Wind and STEREO – if the $+Z$ assumption is true.
- the trajectory implies significantly longer travel times from the source to Wind compared to STEREO – if the $-Z$ assumption is true.

Examining the data, I selected the frequency channel 700 kHz observed by Wind and its nearest counterpart 675 kHz for STEREO. Interestingly, the difference in the arrival times of these signals was merely one minute, which is within the bounds of the time resolution of the instrument. This negligible difference in arrival times supports the $+Z$ assumption for the beam trajectory, meaning it travels approximately at an equal distance between the two spacecraft.

## A.3 Machine Learning Terminology

In this section, I introduce the main concepts related to machine learning which are presented in the dissertation.

- **Cross-validation**: A technique used to evaluate the performance of a machine learning model by dividing the data into subsets and assessing the model on different combinations of these subsets.
- **Input Horizon**: The number of previous time steps considered as input to a model for time series forecasting. It represents the length of the historical sequence used for predictions.
- **Batch Size**: The number of samples processed together in a single iteration of the training algorithm. It affects training speed and memory requirements.

- **Updating the Model's Weights**: The process of adjusting the parameters of a neural network based on training data to minimize the difference between predicted and true outputs. The model's weights represent the parameters that are learned during the training process.
- **Loss**: A function that quantifies the difference between predicted and actual outputs. It guides the optimization process during training.
- **Minimum Validation Loss**: The lowest value achieved by the loss function on a validation dataset during training. It indicates the most accurate predictions on unseen data.
- **Overfitting**: When a model performs well on training data but fails to generalize to unseen data due to memorizing training examples instead of learning underlying patterns.
- **Learning Rate**: A hyperparameter that determines the step size at each iteration of the optimization algorithm during training. It affects learning speed and convergence. A high learning rate can cause the training process to converge quickly, but it may also result in overshooting the optimal solution or getting stuck in a suboptimal solution. On the other hand, a very low learning rate can make the training process slow, and may struggle to find the optimal solution.
- **Reducing the learning rate when the validation loss stops improving**: This concept involves adjusting the learning rate dynamically during the training process. When the validation loss reaches a plateau or stops improving, it indicates a suboptimal point. By reducing the learning rate, the model can take smaller steps in weight space, potentially finding a better solution. This technique, known as learning rate scheduling or learning rate decay, is commonly used to fine-tune the model's performance.
- **Patience**: A parameter used in training to determine the number of epochs to wait for an improvement in validation loss before stopping the training process.
- **Patience Parameter of 7**: In the context of early stopping, training will be stopped if the validation loss does not improve for 7 consecutive epochs.
- **Adam Optimizer**: A popular optimization algorithm in deep learning that combines Adaptive Gradient Algorithm (AdaGrad) and Root Mean Square Propagation (RMSprop) to achieve efficient optimization.
- **Optimal Architecture**: The best configuration of a neural network, including the number of layers, neurons, and other choices, for optimal performance on a specific task.
- **Hyperparameters**: Parameters set before training a model that control the learning algorithm's behavior, such as learning rate, batch size, and activation functions.
- **Layer**: A building block of a neural network that performs specific operations on input data. Includes input, hidden, output, fully connected, convolutional, recurrent, activation, and dropout layers. Here is a description for each layer:
  - **Input Layer**: The first layer of a neural network that receives raw input data. It passes the input to subsequent layers for further processing. The number of nodes in the input layer is determined by the dimensionality of the input data.
  - **Hidden Layers**: Intermediate layers between the input and output layers. They perform computations on the input data and capture higher-level representations or abstractions. Hidden layers are not directly exposed to the input or output.
  - **Output Layer**: The final layer of a neural network that produces model predictions or outputs based on computations from preceding layers. The number of neurons in the output layer depends on the problem being solved, such as regression or classification.
  - **Fully Connected Layer (Dense Layer)**: Each neuron in this layer is connected to every neuron in the previous layer. It allows information flow between all neurons, enabling complex relationships to be learned.
  - **Convolutional Layer**: Commonly used in Convolutional Neural Networks (CNNs) for analyzing grid-like data, such as images. It applies convolution operations using filters or kernels to learn spatial patterns or features.

- **Recurrent Layer**: Used in Recurrent Neural Networks (RNNs) to process sequential data. These layers have feedback connections that allow information to be passed from one step to the next, capturing temporal dependencies and maintaining memory of past inputs.
- **Activation Layer**: Applies a non-linear function to the output of a layer, introducing non-linearity into the neural network. Activation functions like Sigmoid, Hyperbolic Tangent (tanh), or Rectified Linear Unit (ReLU) determine neuron outputs based on weighted inputs.
- **Dropout Layer**: A regularization technique commonly used in deep learning models. It randomly sets a fraction of outputs from the previous layer to zero during training, preventing overfitting and improving generalization.

Layers play a crucial role in the information processing and learning capabilities of neural networks. The arrangement and combination of different layers determine the network's architecture and ultimately its ability to solve specific tasks.

- **Stateful**: A property of Recurrent Neural Networks (RNNs) where the hidden state is preserved between consecutive inputs, allowing the network to have memory.
- **Neuron**: A computational unit in a neural network that receives input, applies weights, and passes the result through an activation function to produce an output.
- **Hidden Neuron**: A neuron in a hidden layer of a neural network that performs intermediate computations.
- **Callback Function**: A function used during model training to perform specific actions at certain points or conditions, such as saving the best model, adjusting learning rates, or early stopping.
- ***LearningRateScheduler* Callback Function**: A function used in training to dynamically adjust the learning rate at specific points based on a predefined schedule or function. It improves training efficiency and convergence by allowing the model to make finer adjustments as it approaches the optimal solution.

### A.3.1 Mathematical Representation of the LSTM NN Model

The computations inside one LSTM cell can be described by the following formulas (Ihianle et al. 2020):

$$f_t = \sigma(W_f x_t + U_f h_{t-1} + b_f) \tag{A.8a}$$
$$i_t = \sigma(W_i x_t + U_i h_{t-1} + b_i) \tag{A.8b}$$
$$\tilde{C}_t = \tanh(W_c x_t + U_c h_{t-1} + b_c) \tag{A.8c}$$
$$C_t = f_t \odot C_{t-1} + i_t \odot \tilde{C}_t \tag{A.8d}$$
$$o_t = \sigma(W_o x_t + U_o h_{t-1} + b_o) \tag{A.8e}$$
$$h_t = o_t \odot \tanh(C_t) \tag{A.8f}$$

where $x_t$ is input data at time $t$. The input gate $i_t$ determines which values from the updated cell states (candidate values) $\tilde{C}_t$ should be added to the cell state. It also takes into account the current input $x_t$ and the previous output $h_{t-1}$, and is passed through a sigmoid activation function. $\tilde{C}_t$ represent the candidate values that are added to the cell state at time $t$. The forget gate activation vector $f_t$ at time step $t$, which determines how much of the previous cell state should be retained. The cell state $C_t$ at time $t$ is updated based on the forget gate, input gate, and candidate values. The output gate $o_t$ at time $t$ determines how much of the cell state should be output. The output vector $h_t$ at time $t$ is calculated based on the cell state and the output gate values. $h_{t-1}$ is the output vector at the previous time step $t-1$. $W_f, W_i, W_c, W_o$ are the weight matrices for the input vector $x_t$. $U_f, U_i, U_c, U_o$ are the weight matrices for the output vector $h_{t-1}$. $b_f, b_i, b_c, b_o$ are the bias vectors. The symbol $\odot$ denotes a pointwise multiplication. The sigmoid function $\sigma$ is used as the activation function for the gate vectors, and the hyperbolic tangent function tanh is used for the candidate values and the output vector.

### A.3.2 Evaluation Metrics

To evaluate the model performance, we used the following equations:

$$L_\delta(y,\hat{y}) = \begin{cases} \frac{1}{2}(y-\hat{y})^2, & \text{if } |y-\hat{y}| \le \delta, \\ \delta(|y-\hat{y}| - \frac{1}{2}\delta), & \text{otherwise} \end{cases} \tag{A.9a}$$

$$MSE = \frac{1}{N}\sum_{i=1}^{N}(y_i - \hat{y}_i)^2 \tag{A.9b}$$

$$MAE = \frac{1}{N}\sum_{i=1}^{N}|y_i - \hat{y}_i| \tag{A.9c}$$

$$RMSE = \sqrt{\frac{\sum_{i=1}^{N}(y_i - \hat{y}_i)^2}{N}} \tag{A.9d}$$

$$MAPE = \frac{1}{N}\sum_{i=1}^{N}|\frac{y_i - \hat{y}_i}{\hat{y}_i}| \tag{A.9e}$$

$$R = \frac{\sum_{i=1}^{n}(y_i - \bar{y})(y_i - \bar{y})}{\sqrt{\sum_{i=1}^{n}(y_i - \bar{y})^2}\sqrt{\sum_{i=1}^{n}(y_i - \bar{y})^2}} \tag{A.9f}$$

where $y$ is the true value, $\hat{y}$ is the predicted value, and $\delta$ is a threshold in the Huber loss function that controls the trade-off between the mean squared error (MSE) and the mean absolute error (MAE). In Chapter 4, it was set to 0.1, which was selected based on several experiments.

MSE is the mean squared error, which measures the difference between predicted and actual values by calculating the average of squared differences. It provides a measure of the average squared magnitude of the errors in your forecasts, which can be useful in penalizing larger errors more heavily than smaller errors.

MAPE is the mean absolute percentage error, which measures the difference between predicted and actual values by calculating the average of absolute differences. It provides a measure of the average magnitude of the errors, allowing to evaluate the overall accuracy of your forecasts.

RMSE is the root mean squared error, which measures the difference between predicted and actual values by taking the square root of the average of squared differences. It provides a measure of the accuracy of the forecasts in the same units as the original data, allowing to evaluate the magnitude of errors in the same scale as the data.

MAPE is the mean absolute percentage error, which measures the accuracy of a forecast by calculating the average of absolute percentage errors. It provides a measure of the accuracy of the forecasts in percentage terms, allowing to evaluate the magnitude of errors relative to the actual values. MSE, MAE, RMSE, and MAPE are often used in regression analysis to assess the accuracy of the model's predictions.

Finally, $R$ is the Pearson correlation coefficient, which measures the strength and direction of the relationship between two continuous variables, and can provide an indication of the extent to which changes in one variable may be related to changes in the other.

## A.4 Deep Learning Model Configuration

The configurations for the ML models shown in Figure 4.5 and their performance on the validation set and the test set for the SEP integral flux $\geq$10 MeV are presented in Table A.2. The batch size was set to be 64 and the number of training epochs was set to be 100. The *EarlyStopping* callback function, with a *patience* of 10, is used to help prevent overfitting during the training process by stopping training when the monitored metric has stopped improving for a certain number of epochs. The *patience* parameter controls how many epochs the training will continue without improvement before it is stopped. This is useful because if the validation loss stops getting better, the model has probably overfitted the training data and is not generalizing effectively to new data. By stopping the training early, we can avoid wasting time and resources on further training that is unlikely to improve the model's performance.

I used the *ModelCheckpoint* callback function to save the best weights of the model during training so that they can be reused later. The *LearningRateScheduler* callback function allows to dynamically adjust the learning rate of the model during training using a function passed to it that will be called at the beginning of each epoch, and it should return the desired learning rate for that epoch. It can be useful when training deep neural networks, as it allows for a higher learning rate in the early stages of training when the model is still far from convergence, and a lower learning rate as the model approaches convergence, which can help it to converge more accurately. The downside might be the longer training time.

Table A.2: Configuration of the ML model. (1) refers to the error value for 1-day forecasting. Same for (2) refers to 2-day forecasting, and (3) for 3-day forecasting. *In the 1D-CNN layer, 32 filters, a kernel size of 5, and strides of 1 were used.

| Model Architecture | No. of Hidden Layers | No. of Hidden Neurons | Activation Function | Batch Size | Learning Rate | Epochs | Callbacks Functions | Validation Set | | | | Testing Set | | | |
|---|---|---|---|---|---|---|---|---|---|---|---|---|---|---|---|
| | | | | | | | | MAE | MSE | RMSE | MAPE | MAE | MSE | RMSE | MAPE |
| Linear | – | – | – | 64 | 0.001 | 100 | EarlyStopping | 0.312 | 0.141 | 0.376 | 87.883 | 0.143 | 0.045 | 0.211 | 60.689 |
| Dense ML | 2 | 32 | ReLU | 64 | 0.001 | 100 | EarlyStopping | 0.262 (1)<br>0.275 (2)<br>0.290 (3) | 0.118 (1)<br>0.138 (2)<br>0.166 (3) | 0.344 (1)<br>0.372 (2)<br>0.407 (3) | 132.580 (1)<br>132.004 (2)<br>129.288 (3) | 0.400 (1)<br>0.395 (2)<br>0.392 (3) | 0.281 (1)<br>0.286 (2)<br>0.294 (3) | 0.530 (1)<br>0.535 (2)<br>0.542 (3) | 238.898 (1)<br>234.704 (2)<br>230.896 (3) |
| Simple RNN | 2 | 32 | Tanh | 64 | 0.001 | 100 | EarlyStopping<br>ModelCheckpoint | 0.143 (1)<br>0.171 (2)<br>0.264 (3) | 0.035 (1)<br>0.063 (2)<br>0.118 (3) | 0.187 (1)<br>0.251 (2)<br>0.343 (3) | 70.990 (1)<br>68.694 (2)<br>72.505 (3) | 0.178 (1)<br>0.171 (2)<br>0.200 (3) | 0.052 (1)<br>0.071 (2)<br>0.084 (3) | 0.228 (1)<br>0.266 (2)<br>0.289 (3) | 69.624 (1)<br>78.075 (2)<br>67.416 (3) |
| Stateful RNN | 3 | 32 | Tanh | 64 | $1.58e^{-4}$ | 100 | LearningRateScheduler<br>EarlyStopping | 0.203 (1)<br>0.305 (2)<br>0.349 (3) | 0.060 (1)<br>0.131 (2)<br>0.173 (3) | 0.244 (1)<br>0.362 (2)<br>0.416 (3) | 56.390 (1)<br>81.028 (2)<br>82.819 (3) | 0.155 (1)<br>0.223 (2)<br>0.223 (3) | 0.039 (1)<br>0.079 (2)<br>0.084 (3) | 0.197 (1)<br>0.281 (2)<br>0.289 (3) | 59.988 (1)<br>71.679 (2)<br>64.159 (3) |
| Stateful LSTM | 3 | 32 | Tanh | 64 | $1.58e^{-4}$ | 100 | EarlyStopping | 0.095 (1)<br>0.151 (2)<br>0.174 (3) | 0.021 (1)<br>0.048 (2)<br>0.076 (3) | 0.146 (1)<br>0.220 (2)<br>0.275 (3) | 40.335 (1)<br>48.937 (2)<br>55.662 (3) | 0.098 (1)<br>0.134 (2)<br>0.166 (3) | 0.020 (1)<br>0.042 (2)<br>0.071 (3) | 0.141 (1)<br>0.205 (2)<br>0.267 (3) | 41.781 (1)<br>57.860 (2)<br>68.025 (3) |
| Stateful Bi-LSTM | 3 | 32 | Tanh | 64 | $1.58e^{-4}$ | 100 | EarlyStopping | 0.149 (1)<br>0.190 (2)<br>0.249 (3) | 0.043 (1)<br>0.074 (2)<br>0.120 (3) | 0.207 (1)<br>0.272 (2)<br>0.347 (3) | 58.151 (1)<br>60.154 (2)<br>67.988 (3) | 0.170 (1)<br>0.211 (2)<br>0.229 (3) | 0.049 (1)<br>0.090 (2)<br>0.108 (3) | 0.221 (1)<br>0.300 (2)<br>0.329 (3) | 71.059 (1)<br>92.727 (2)<br>87.049 (3) |
| 1D-CNN LSTM | 3 | 32 (5,1)* | ReLU<br>Tanh | 64 | $1.58e^{-4}$ | 100 | EarlyStopping | 0.108 (1)<br>0.146 (2)<br>0.177 (3) | 0.027 (1)<br>0.051 (2)<br>0.078 (3) | 0.165 (1)<br>0.226 (2)<br>0.279 (3) | 41.164 (1)<br>47.512 (2)<br>53.087 (3) | 0.098 (1)<br>0.138 (2)<br>0.156 (3) | 0.023 (1)<br>0.047 (2)<br>0.067 (3) | 0.151 (1)<br>0.217 (2)<br>0.259 (3) | 51.732 (1)<br>68.376 (2)<br>69.338 (3) |

All the calculations and model runs were implemented under the framework of TensorFlow 2.3.0 (Singh et al. 2020) in Python 3.6.13. The models were executed on Ubuntu 20.04.1 LTS OS with 4 $\times$ GPUs (NVIDIA GeForce RTX 2080 Ti, 11019 MiB, 300 MHz). According to the Keras API guide (Ketkar & Ketkar 2017), the requirements to use the cuDNN implementation are the activation function must be set to *tanh* and the recurrent activation must be set to *sigmoid*. I also set the seed number to 7 across all the model runs to maintain reproducibility.

Stateful RNNs can be difficult to work with when using callbacks in Keras because their hidden state must be manually managed across mini-batch updates. When training a stateful RNN in Keras, the hidden state is carried over from the previous epoch and can cause problems with certain callbacks, such as *EarlyStopping* or *ModelCheckpoint*. To work around this issue, one can use stateless RNNs or manually reset the hidden state at the end of each epoch, but this can be complex and prone to errors.

## A.5 Description of Skill Scores

Skill scores and ratios are commonly used in evaluating the performance of classification models, particularly in binary classification tasks. They provide insights into the model's ability to correctly predict positive and negative instances. Here is a brief description of each skill score and ratio, along with their formulas:

- **True Positive (TP)**: The number of data points or intervals correctly identified as positive by the model. It represents instances where both the model and the ground truth indicate the presence of an event.
- **True Negative (TN)**: The number of intervals correctly identified as negative by the model. It represents instances where both the model and the ground truth indicate the absence of an event.
- **False Positive (FP)**: The number of intervals incorrectly identified as positive by the model. It occurs when the model predicts an event, but the ground truth indicates its absence.
- **False Negative (FN)**: The number of intervals incorrectly identified as negative by the model. It occurs when the model fails to detect an event that the ground truth indicates its presence.
- **Accuracy**: Represents the proportion of correct predictions out of total predictions.

$$Accuracy = \frac{TP + TN}{TP + TN + FP + FN} \tag{A.10}$$

- **Precision**: Represents the proportion of positive predictions that are actually positive.

$$Precision = \frac{TP}{TP + FP} \tag{A.11}$$

- **Probability of Detection (POD) or Recall**: Represents the model's ability to correctly identify positive instances.

$$POD = \frac{TP}{TP + FN} \tag{A.12}$$

- **Probability of False Detection (POFD)**: Measures the model's tendency to falsely predict positive instances when the ground truth indicates their absence.

$$POFD = \frac{FP}{FP + TN} \tag{A.13}$$

- **False Alarm Rate (FAR)**: Indicates the ratio of false positive predictions to the total number of positive instances.

$$FAR = \frac{FP}{FP + TP} \tag{A.14}$$

- **Critical Success Index (CSI)**: Measures the model's ability to correctly predict both positive and negative instances.

$$CSI = \frac{TP}{TP + FP + FN} \tag{A.15}$$

- **True Skill Statistic (TSS)**: Takes into account both the model's ability to detect positive instances and its ability to avoid false alarms.

$$TSS = POD - FAR \tag{A.16}$$

- **Heidke Skill Score (HSS)**: Evaluates the model's performance by comparing it with random chance. It takes into account the agreement between the model's predictions and the observed data, considering both true positive and true negative predictions.

$$HSS = \frac{TP + TN - C}{T - C} \tag{A.17}$$

where

$$T = TP + TN + FP + FN$$
$$C = \frac{(TP + FP)(TP + FN) + (TN + FP)(TN + FN)}{T}$$

# Bibliography


Abe, O., Fakomiti, M., Igboama, W., et al. 2023, Advances in Space Research, 71, 2240

Akansu, A. N. 1991, Optical Engineering, 30, 912

Akasofu, S. I. 1981, Space Science Reviews, 28, 121

Alharbi, F. R. & Csala, D. 2021, in 2021 International Conference on Electrical, Communication, and Computer Engineering (ICECCE), IEEE, 1–6

Altschuler, M. D. & Newkirk, G. 1969, Solar Physics, 9, 131

Amari, T., Canou, A., & Aly, J.-J. 2014, Nature, 514, 465

Aminalragia-Giamini, S., Raptis, S., Anastasiadis, A., et al. 2021, Journal of Space Weather and Space Climate, 11, 59

Aschwanden, M. J. 2002, Space Science Reviews, 101, 1

Aschwanden, M. J. 2010, Solar Physics, 262, 235

Badman, S. T., Carley, E., Cañizares, L. A., et al. 2022, The Astrophysical Journal, 938, 95

Bale, S., Goetz, K., Harvey, P., et al. 2016, Space science reviews, 204, 49

Bastian, T., Pick, M., Kerdraon, A., Maia, D., & Vourlidas, A. 2001, The Astrophysical Journal, 558, L65

Battarbee, M., Vainio, R., Laitinen, T., & Hietala, H. 2013, Astronomy & Astrophysics, 558, A110

Bein, B. M., Berkebile-Stoiser, S., Veronig, A. M., et al. 2011, apj, 738, 191

Benson, B., Pan, W. D., Prasad, A., Gary, G. A., & Hu, Q. 2020, Solar Physics, 295, 65

Berghmans, D., Auchère, F., Long, D. M., et al. 2021, Astronomy & Astrophysics, 656, L4

Besliu-Ionescu, D., Maris Muntean, G., & Dobrica, V. 2022, Solar Physics, 297, 65

Biesecker, D., Myers, D., Thompson, B., Hammer, D., & Vourlidas, A. 2002, The Astrophysical Journal, 569, 1009

Bonnin, X., Hoang, S., & Maksimovic, M. 2008, Astron. Astrophys., 489, 419

Borovsky, J. E. & Denton, M. H. 2006, Journal of Geophysical Research: Space Physics, 111

Boudjada, M. Y., Abou el Fadl, A., Galopeau, P. H., Al-Haddad, E., & Lammer, H. 2020, Advances in Radio Science, 18, 83

Brewer, D. A., Barth, J. L., Label, K. A., Kauffman, W. J., & Giffin, G. 2002, Acta Astronautica, 51, 609

Bruno, A. & Richardson, I. G. 2021, Solar Physics, 296, 36

Byrne, J., Long, D., Gallagher, P., et al. 2013, Astronomy & Astrophysics, 557, A96

Camporeale, E. 2019, Space weather, 17, 1166

Cane, H. V., Erickson, W., & Prestage, N. 2002, Journal of Geophysical Research: Space Physics, 107, SSH

Cattell, C., Glesener, L., Leiran, B., et al. 2021, Astron. Astrophys., 650, A6

Che, H. 2018, Journal of Physics: Conference Series, 1100, 012005

Chen, N., Ip, W.-H., & Innes, D. 2013, Astrophys. J., 769, 96

Chen, P. 2016, Low-Frequency Waves in Space Plasmas, 379

Chen, P. F., Wu, S. T., Shibata, K., & Fang, C. 2002, The Astrophysical Journal, 572, L99

Chen, X., Kontar, E. P., Chrysaphi, N., et al. 2023, arXiv e-prints, arXiv:2306.09160

Cheung, M. C., Boerner, P., Schrijver, C., et al. 2015, The Astrophysical Journal, 807, 143

Chhabra, S., Klimchuk, J. A., & Gary, D. E. 2021, The Astrophysical Journal, 922, 128

Dalla, S., Swalwell, B., Battarbee, M., et al. 2017in (Cambridge University Press), 268–271

Debrunner, H., Flückiger, E., Grädel, H., Lockwood, J., & McGuire, R. 1988, Journal of Geophysical Research: Space Physics, 93, 7206

Delannée, C. & Aulanier, G. 1999, Solar Physics, 190, 107

Dierckxsens, M., Tziotziou, K., Dalla, S., et al. 2015, Solar Physics, 290, 841

Domingo, V., Fleck, B., & Poland, A. I. 1995, Solar Physics, 162, 1

Dulk, G., Steinberg, J.-L., Lecacheux, A., Hoang, S., & MacDowall, R. J. 1985, Astronomy and Astrophysics, 150, L28

Dungey, J. 1961, Journal of Geophysical Research, 66, 1043

Eastwood, J., Nakamura, R., Turc, L., Mejnertsen, L., & Hesse, M. 2017, Space Science Reviews, 212, 1221

Echer, E. & Gonzalez, W. 2022, Advances in Space Research, 70, 2830

Echer, E., Tsurutani, B., & Gonzalez, W. 2013, Journal of Geophysical Research: Space Physics, 118, 385

Efron, B. 1979, The Annals of Statistics, 7, 1

Engell, A., Falconer, D., Schuh, M., Loomis, J., & Bissett, D. 2017, Space Weather, 15, 1321

Ergun, R., Larson, D., Lin, R., et al. 1998, The Astrophysical Journal, 503, 435

Feynman, J., Armstrong, T., Dao-Gibner, L., & Silverman, S. 1990, Solar Physics, 126, 385

Fletcher, L., Dennis, B. R., Hudson, H. S., et al. 2011, Space science reviews, 159, 19

Florios, K., Kontogiannis, I., Park, S.-H., et al. 2018, Solar Physics, 293, 28

Fox, N., Velli, M., Bale, S., et al. 2016, Space Science Reviews, 204, 7

Fredkin, D. R., Rice, J. A., Colquhoun, D., & Gibb, A. 1995, Philosophical Transactions of the Royal Society of London. Series B: Biological Sciences, 350, 353

Gabriel, S., Evans, R., & Feynman, J. 1990, Solar physics, 128, 415

Gallagher, P. T., Lawrence, G. R., & Dennis, B. R. 2003, The Astrophysical Journal Letters, 588, L53

Gieseler, J., Dresing, N., Palmroos, C., et al. 2023, Frontiers in Astronomy and Space Sciences, 9, 384

Gonzalez, W., Joselyn, J.-A., Kamide, Y., et al. 1994, Journal of Geophysical Research: Space Physics, 99, 5771

González, W. D., Echer, E., Clua-Gonzalez, A., & Tsurutani, B. T. 2007, Geophysical research letters, 34

Goodfellow, I., Bengio, Y., & Courville, A. 2016, Deep learning (MIT press)

Gopalswamy, N. 2022, Atmosphere, 13, 1781

Gopalswamy, N., Akiyama, S., Yashiro, S., Michalek, G., & Lepping, R. 2008, Journal of Atmospheric and Solar-Terrestrial Physics, 70, 245

Gopalswamy, N., Mäkelä, P., & Yashiro, S. 2019, Sun and Geosphere, 14, 111

Gopalswamy, N., Mäkelä, P., Yashiro, S., et al. 2017in , IOP Publishing, 012009

Gopalswamy, N., Mäkelä, P., Yashiro, S., Akiyama, S., & Xie, H. 2022a, in 2022 3rd URSI Atlantic and Asia Pacific Radio Science Meeting (AT-AP-RASC), 1–4

Gopalswamy, N. & Yashiro, S. 2011, apjl, 736, L17

Gopalswamy, N., Yashiro, S., Akiyama, S., et al. 2022b, Journal of Geophysical Research: Space Physics, 127, e2022JA030404

Graves, A. & Jaitly, N. 2014in (Bejing, China: PMLR), 1764–1772

Graves, A. & Schmidhuber, J. 2005, Neural networks, 18, 602

Greff, K., Srivastava, R. K., Koutník, J., Steunebrink, B. R., & Schmidhuber, J. 2016, IEEE transactions on neural networks and learning systems, 28, 2222

Guo, F. & Giacalone, J. 2013, The Astrophysical Journal, 773, 158

Gurnett, D. A. & Anderson, R. R. 1976, Science, 194, 1159

Gurnett, D. A. & Anderson, R. R. 1977, Journal of Geophysical Research, 82, 632

Hale, G. E., Ellerman, F., Nicholson, S. B., & Joy, A. H. 1919, Astrophys. J., 49, 153

Harra, L., Brooks, D. H., Bale, S. D., et al. 2021, Astronomy & Astrophysics, 650, A7

Hochreiter, S. & Schmidhuber, J. 1997, Neural computation, 9, 1735

Holman, G. D., Aschwanden, M. J., Aurass, H., et al. 2011, Space science reviews, 159, 107

Holschneider, M., Kronland-Martinet, R., Morlet, J., & Tchamitchian, P. 1989, in Wavelets. Time-Frequency Methods and Phase Space, ed. J.-M. Combes, A. Grossmann, & P. Tchamitchian (Springer-Verlag), 286

Hu, J., Li, G., Ao, X., Zank, G. P., & Verkhoglyadova, O. 2017, Journal of Geophysical Research: Space Physics, 122, 10

Huang, X., Tan, H., Lin, G., & Tian, Y. 2018, 2018 International Conference on Artificial Intelligence and Big Data (ICAIBD), 185

Ihianle, I. K., Nwajana, A. O., Ebenuwa, S. H., et al. 2020, IEEE Access, 8, 179028

Ireland, J., Inglis, A. R., Shih, A. Y., et al. 2019, Solar Physics, 294, 158

Ishikawa, S.-n., Glesener, L., Krucker, S., et al. 2017, Nature Astronomy, 1, 771

Jackson, B., Hick, P., Buffington, A., et al. 2010in , American Institute of Physics, 659–662

Jang, S., Moon, Y.-J., Kim, R.-S., Lee, H., & Cho, K.-S. 2016, The Astrophysical Journal, 821, 95

Kahler, S., Cliver, E., Cane, H., et al. 1987, in Proceedings of the $20^{th}$ International Cosmic Ray Conference Moscow, Volume 3, p. 121

Kahler, S., Sheeley Jr, N., Howard, R., et al. 1984, Journal of Geophysical Research: Space Physics, 89, 9683

Kahler, S. W., Cliver, E. W., & Ling, A. G. 2007, Journal of Atmospheric and Solar-Terrestrial Physics, 69, 43

Kane, R. 2011, Indian Journal of Radio & Space Physics, 40, 7

Kasapis, S., Zhao, L., Chen, Y., et al. 2022, Space Weather, 20, e2021SW002842

Kay, C. & Gopalswamy, N. 2018, Journal of Geophysical Research: Space Physics, 123, 7220

Ketkar, N. & Ketkar, N. 2017, Deep learning with python: a hands-on introduction, 97

Kingma, D. P. & Ba, J. 2015, International Conference on Learning Representations (ICLR), San Diego

Klassen, A., Karlickỳ, M., & Mann, G. 2003a, Astronomy & Astrophysics, 410, 307

Klassen, A., Pohjolainen, S., & Klein, K.-L. 2003b, Solar Physics, 218, 197

Klein, K.-L. & Dalla, S. 2017, Space Science Reviews, 212, 1107

Kolen, J. F. & Kremer, S. C. 2001, Gradient Flow in Recurrent Nets: The Difficulty of Learning LongTerm Dependencies (IEEE), 237–243

Kong, X., Guo, F., Giacalone, J., Li, H., & Chen, Y. 2017, The Astrophysical Journal, 851, 38

Kontar, E. P., Chen, X., Chrysaphi, N., et al. 2019, The Astrophysical Journal, 884, 122

Kontar, E. P., Emslie, A. G., Clarkson, D. L., et al. 2023, arXiv preprint arXiv:2308.05839

Kontar, E. P., Yu, S., Kuznetsov, A., et al. 2017, Nature communications, 8, 1515

Kouloumvakos, A., Rodríguez-García, L., Gieseler, J., et al. 2022, Frontiers in Astronomy and Space Sciences, 9, 974137

Kozarev, K., Nedal, M., Miteva, R., Dechev, M., & Zucca, P. 2022, Frontiers in Astronomy and Space Sciences, 9, 34

Kozarev, K., Schwadron, N., Dayeh, M., et al. 2010, Space Weather, 8

Kozarev, K. A., Davey, A., Kendrick, A., Hammer, M., & Keith, C. 2017, Journal of Space Weather and Space Climate, 7, A32

Kozarev, K. A., Dayeh, M. A., & Farahat, A. 2019, The Astrophysical Journal, 871, 65

Kozarev, K. A., Evans, R. M., Schwadron, N. A., et al. 2013, The Astrophysical Journal, 778, 43

Kozarev, K. A., Korreck, K. E., Lobzin, V. V., Weber, M. A., & Schwadron, N. A. 2011, The Astrophysical Journal, 733, L25

Kozarev, K. A., Raymond, J. C., Lobzin, V. V., & Hammer, M. 2015, The Astrophysical Journal, 799, 167

Kozarev, K. A. & Schwadron, N. A. 2016, apj, 831, 120

Krucker, S., Hudson, H. S., Jeffrey, N. L. S., et al. 2011, The Astrophysical Journal, 739, 96

Krupar, V., Szabo, A., Maksimovic, M., et al. 2020, Astrophys. J. Suppl., 246, 57

Kwon, R.-Y., Zhang, J., & Olmedo, O. 2014, The Astrophysical Journal, 794, 148

Laitinen, T. & Dalla, S. 2017, The Astrophysical Journal, 834, 127

Lakhina, G. S. & Tsurutani, B. T. 2016, Geoscience Letters, 3, 1

Lanzerotti, L. J. 2001, Washington DC American Geophysical Union Geophysical Monograph Series, 125, 11

Lavasa, E., Giannopoulos, G., Papaioannou, A., et al. 2021, Solar Physics, 296, 107

Le, G.-M. & Zhang, X.-F. 2017, Research in Astronomy and Astrophysics, 17, 123

Lecacheux, A., Steinberg, J. L., Hoang, S., & Dulk, G. A. 1989, Astron. Astrophys., 217, 237

Lemen, J. R., Akin, D. J., Boerner, P. F., et al. 2011, in The solar dynamics observatory (Springer), 17–40

Lemen, J. R., Title, A. M., Akin, D. J., et al. 2012, Solar Physics, 275, 17

Li, B. & Cairns, I. H. 2012, The Astrophysical Journal, 753, 124

Li, G., Zank, G., & Rice, W. 2003, Journal of Geophysical Research: Space Physics, 108

Lilensten, J., Coates, A. J., Dehant, V., et al. 2014, The Astronomy and Astrophysics Review, 22, 1

Lin, R. 2005, Advances in Space Research, 35, 1857

Liu, W. & Ofman, L. 2014, Solar Physics, 289, 3233

Long, D. M., Bloomfield, D. S., Chen, P.-F., et al. 2017, Solar physics, 292, 1

Long, D. M., Bloomfield, D. S., Gallagher, P. T., & Pérez-Suárez, D. 2014, Solar Physics, 289, 3279

Long, D. M., DeLuca, E. E., & Gallagher, P. T. 2011, apjl, 741, L21

Ma, S., Raymond, J. C., Golub, L., et al. 2011, The Astrophysical Journal, 738, 160

MacDowall, R., Lara, A., Manoharan, P., et al. 2003, Geophysical research letters, 30

Madjarska, M. S. 2019, Living Reviews in Solar Physics, 16, 2

Magdalenić, J., Marqué, C., Zhukov, A. N., Vršnak, B., & Žic, T. 2010a, Astrophys. J., 718, 266

Magdalenić, J., Marqué, C., Zhukov, A. N., Vršnak, B., & Žic, T. 2010b, Astrophys. J., 718, 266

Malandraki, O. E. & Crosby, N. B. 2018, Solar particle radiation storms forecasting and analysis: the HESPERIA HORIZON 2020 project and beyond

Mann, G., Klassen, A., Aurass, H., & Classen, H.-T. 2003, Astronomy & Astrophysics, 400, 329

Mann, G., Breitling, F., Vocks, C., et al. 2018, A&A, 611, A57

Manu, V., Balan, N., Zhang, Q.-H., & Xing, Z.-Y. 2022, Journal of Geophysical Research: Space Physics, 127, e2022JA030747

Markwardt, C. B. 2009, in Astronomical Society of the Pacific Conference Series, Vol. 411, Astronomical Data Analysis Software and Systems XVIII, ed. D. A. Bohlender, D. Durand, & P. Dowler, 251

Melrose, D. 1980, Space Science Reviews, 26, 3

Melrose, D. 2017, Reviews of Modern Plasma Physics, 1, 1

Mierla, M., Inhester, B., Antunes, A., et al. 2010in , Copernicus GmbH, 203–215

Mikić, Z., Linker, J. A., Schnack, D. D., Lionello, R., & Tarditi, A. 1999, Physics of Plasmas, 6, 2217

Miteva, R., Klein, K.-L., Malandraki, O., & Dorrian, G. 2013, Solar Physics, 282, 579

Miteva, R., Nedal, M., Samwel, S. W., & Temmer, M. 2023, Universe, 9, 179

Miteva, R., Samwel, S., Costa-Duarte, M., & Danov, D. 2016, in Proceedings of the Eighth Workshop" Solar Influences on the Magnetosphere, Ionosphere and Atmosphere, Vol. 30, 27–30

Miteva, R., Samwel, S., Costa-Duarte, M., & Malandraki, O. 2017, Sun Geosph, 12

Moore, R. L., Sterling, A. C., Hudson, H. S., & Lemen, J. R. 2001, The Astrophysical Journal, 552, 833

Morosan, D. E. & Gallagher, P. T. 2017, in Planetary Radio Emissions VIII, ed. G. Fischer, G. Mann, M. Panchenko, & P. Zarka, 357–368

Nammous, M. K., Saeed, K., & Kobojek, P. 2022, Journal of King Saud University - Computer and Information Sciences, 34, 764

Nedal, M., Kozarev, K., Arsenov, N., & Zhang, P. 2023a, J. Space Weather Space Clim., 13, 26

Nedal, M., Kozarev, K., Zhang, P., & Zucca, P. 2023b, A&A, 680, A106

Nedal, M., Mahrous, A., & Youssef, M. 2019, Astrophysics and Space Science, 364, 161

Newkirk, G. 1967, Annual Review of Astronomy and Astrophysics, 5, 213

Newkirk, Gordon, J. 1961, Astrophys. J., 133, 983

Nindos, A., Alissandrakis, C. E., Hillaris, A., & Preka-Papadema, P. 2011, Astron. Astrophys., 531, A31

Nindos, A., Aurass, H., Klein, K. L., & Trottet, G. 2008, Sol. Phys., 253, 3

Nitta, N. V., Mason, G. M., Wang, L., Cohen, C. M. S., & Wiedenbeck, M. E. 2015, The Astrophysical Journal, 806, 235

Nitta, N. V., Schrijver, C. J., Liu, W., et al. 2013, The Astrophysical Journal, 776, 58

Nymmik, R. 2007, Advances in Space Research, 40, 321

Núñez, M. 2011, Space Weather, 9

Odstrcil, D., Riley, P., & Zhao, X. 2004, Journal of Geophysical Research: Space Physics, 109

Offringa, A. R., McKinley, B., Hurley-Walker, N., et al. 2014, Mon. Not. R. Astron. Soc., 444, 606

Ofman, L. & Thompson, B. 2002, The Astrophysical Journal, 574, 440

Olah, C. 2015, Neural Networks, Types, and Functional Programming, [Blog post]

Olmedo, O., Vourlidas, A., Zhang, J., & Cheng, X. 2012, The Astrophysical Journal, 756, 143

Ontiveros, V. & Vourlidas, A. 2009, The Astrophysical Journal, 693, 267

Ontiveros, V. & Vourlidas, A. 2009, apj, 693, 267

Pala, Z. & Atici, R. 2019, Solar Physics, 294, 50

Paouris, E., Vourlidas, A., Papaioannou, A., & Anastasiadis, A. 2021, Space Weather, 19, e2020SW002617

Papaioannou, A., Anastasiadis, A., Kouloumvakos, A., et al. 2018, Solar Physics, 293, 1

Papaioannou, A., Vainio, R., Raukunen, O., et al. 2022, Journal of Space Weather and Space Climate, 12, 24

Park, J., Innes, D. E., Bucik, R., & Moon, Y.-J. 2013, The Astrophysical Journal, 779, 184

Parker, E. N. 1960, Astrophysical Journal, 132, 821

Patsourakos, S. & Vourlidas, A. 2009, The Astrophysical Journal, 700, L182

Patsourakos, S. & Vourlidas, A. 2012, Solar Physics, 281, 187

Patsourakos, S., Vourlidas, A., & Stenborg, G. 2010, Astrophys. J. Lett., 724, L188

Pérez-Suárez, D., Higgins, P. A., Bloomfield, D. S., et al. 2011, Automated Solar Feature Detection for Space Weather Applications, 207–225

Pesnell, W. D., Thompson, B. J., & Chamberlin, P. C. 2012, solphys, 275, 3

Piantschitsch, I., Vršnak, B., Hanslmeier, A., et al. 2018, The Astrophysical Journal, 860, 24

Pick, M. 2006, in Solar and Heliospheric Origins of Space Weather Phenomena, ed. J.-P. Rozelot, Vol. 699, 119

Pick, M., Forbes, T. G., Mann, G., et al. 2006, Multi-Wavelength Observations of CMEs and Associated Phenomena, Vol. 21, 341

Podladchikova, O. & Berghmans, D. 2005, Solar Physics, 228, 265

Pomoell, J. & Poedts, S. 2018, Journal of Space Weather and Space Climate, 8, A35

Priest, E. & Forbes, T. 2007, Magnetic Reconnection

Pulkkinen, T. 2007, Living Reviews in Solar Physics, 4, 1

Pulupa, M., Bale, S., Bonnell, J., et al. 2017, Journal of Geophysical Research: Space Physics, 122, 2836

Pulupa, M., Bale, S. D., Badman, S. T., et al. 2020, Astrophys. J. Suppl., 246, 49

Pysz, M. A., Foygel, K., Panje, C. M., et al. 2011, Investigative radiology, 46, 187

Qiu, S., Zhang, Z., Yousof, H., et al. 2022, Advances in Space Research, 70, 2047

Ramstad, R., Holmström, M., Futaana, Y., et al. 2018, Geophysical Research Letters, 45, 7306

Reames, D. V. 1999, Space Science Reviews, 90, 413

Reames, D. V. 2013, Space Science Reviews, 175, 53

Reames, D. V. 2021

Reid, H. A. 2020, Frontiers in Astronomy and Space Sciences, 7, 56

Reid, H. A. & Kontar, E. P. 2018a, Astronomy & Astrophysics, 614, A69

Reid, H. A. & Kontar, E. P. 2018b, The Astrophysical Journal, 867, 158

Reid, H. A. S. & Ratcliffe, H. 2014, Research in Astronomy and Astrophysics, 14, 773

Reiner, M. J., Goetz, K., Fainberg, J., et al. 2009, Solar Physics, 259, 255

Ripley, B. D. 1996, Pattern Recognition and Neural Networks (Cambridge University Press)

Rodriguez, J., Onsager, T., & Mazur, J. 2010, Geophysical Research Letters, 37

Rouillard, A. P., Plotnikov, I., Pinto, R. F., et al. 2016, The Astrophysical Journal, 833, 45

Rouillard, A. P., Sheeley, N. R., Tylka, A., et al. 2012, The Astrophysical Journal, 752, 44

Saint-Hilaire, P., Vilmer, N., & Kerdraon, A. 2012, The Astrophysical Journal, 762, 60

Saiz, E., Cerrato, Y., Cid, C., et al. 2013, Journal of Space Weather and Space Climate, 3, A26

Samwel, S. & Miteva, R. 2023, Advances in Space Research, 72, 3440

Savitzky, A. & Golay, M. J. 1964, Analytical chemistry, 36, 1627

Schatten, K. H., Wilcox, J. M., & Ness, N. F. 1969, Solar Physics, 6, 442

Schrijver, C. J. 2015, Space Weather, 13, 524

Schrijver, C. J., Kauristie, K., Aylward, A. D., et al. 2015, Advances in Space Research, 55, 2745

Schrijver, C. J. & Siscoe, G. L. 2010a, Heliophysics: Evolving solar activity and the climates of space and Earth (Cambridge University Press)

Schrijver, C. J. & Siscoe, G. L. 2010b, Heliophysics: Evolving solar activity and the climates of space and Earth (Cambridge University Press)

Schuster, M. & Paliwal, K. K. 1997, IEEE transactions on Signal Processing, 45, 2673

Schwadron, N. A., Gorby, M., Török, T., et al. 2014, Space Weather, 12, 323

Schwadron, N. A., Lee, M., Gorby, M., et al. 2015, The Astrophysical Journal, 810, 97

Schwadron, N. A., Townsend, L., Kozarev, K., et al. 2010, Space Weather, 8

Schwenn, R. 2006, Living reviews in solar physics, 3, 1

Selvakumaran, R., Veenadhari, B., Akiyama, S., et al. 2016, Journal of Geophysical Research: Space Physics, 121, 8188

Singh, P., Manure, A., Singh, P., & Manure, A. 2020, Learn TensorFlow 2.0: Implement Machine Learning and Deep Learning Models with Python, 1

Sokolov, I., Roussev, I., Gombosi, T., et al. 2004, The Astrophysical Journal, 616, L171

Sokolov, I. V., Roussev, I. I., Skender, M., Gombosi, T. I., & Usmanov, A. V. 2009, The Astrophysical Journal, 696, 261

Stansby, D., Yeates, A., & Badman, S. T. 2020, Journal of Open Source Software, 5, 2732

Starck, J.-L. & Murtagh, F. 2002, Astronomical image and data analysis (Springer Netherlands)

Stepanyuk, O., Kozarev, K., & Nedal, M. 2022, Journal of Space Weather and Space Climate, 12, 20

Sundermeyer, M., Alkhouli, T., Wuebker, J., & Ney, H. 2014, in Proceedings of the 2014 conference on empirical methods in natural language processing (EMNLP) (Association for Computational Linguistics), 14–25

Suzuki, S. & Dulk, G. 1985, Cambridge: Cambridge University Press, 289

Švestka, Z. 1995, Advances in Space Research, 16, 27

Temmer, M. 2021, Living Reviews in Solar Physics, 18, 4

Thernisien, A. 2011, The Astrophysical Journal Supplement Series, 194, 33

Thernisien, A., Vourlidas, A., & Howard, R. 2009, Solar Physics, 256, 111

Thompson, B. & Young, C. 2016, The Astrophysical Journal, 825, 27

Thompson, B. c., Gurman, J., Neupert, W., et al. 1999, The Astrophysical Journal, 517, L151

Thompson, B. J. & Myers, D. C. 2009, Astrophys. J. Suppl., 183, 225

Thompson, B. J., Plunkett, S. P., Gurman, J. B., et al. 1998, grl, 25, 2465

Torsti, J., Valtonen, E., Lumme, M., et al. 1995, Sol. Phys., 162, 505

Trottet, G., Samwel, S., Klein, K.-L., Dudok de Wit, T., & Miteva, R. 2015, Solar Physics, 290, 819

Truscott, P., Lei, F., Dyer, C., et al. 2000, in 2000 IEEE Radiation Effects Data Workshop. Workshop Record. Held in conjunction with IEEE Nuclear and Space Radiation Effects Conference (Cat. No. 00TH8527), IEEE, 147–152

Tsurutani, B. T. 1985

Tsurutani, B. T., Gonzalez, W. D., & Kamide, Y. 1997, Surveys in geophysics, 18, 363

Vainio, R. & Laitinen, T. 2008, Journal of Atmospheric and Solar-Terrestrial Physics, 70, 467

van Haarlem, M. P., Wise, M. W., Gunst, A., et al. 2013, Astronomy & astrophysics, 556, A2

Verbeeck, C., Delouille, V., Mampaey, B., & De Visscher, R. 2014, Astronomy and Astrophysics, 561, A29

Verbeke, C., Mays, M. L., Kay, C., et al. 2022, Advances in Space Research

Verkhoglyadova, O., Li, G., Zank, G., Hu, Q., & Mewaldt, R. 2009, The Astrophysical Journal, 693, 894

Veronig, A., Muhr, N., Kienreich, I., Temmer, M., & Vršnak, B. 2010, The Astrophysical Journal Letters, 716, L57

Vourlidas, A., Lynch, B. J., Howard, R. A., & Li, Y. 2013, Solar Physics, 284, 179

Vourlidas, A., Syntelis, P., & Tsinganos, K. 2012, Solar Physics, 280, 509

Vourlidas, A., Wu, S. T., Wang, A. H., Subramanian, P., & Howard, R. A. 2003, apj, 598, 1392

Vršnak, B. & Cliver, E. W. 2008, Solar Physics, 253, 215

Vršnak, B., Žic, T., Vrbanec, D., et al. 2013, Solar physics, 285, 295

Warmuth, A. 2015, Living Reviews in Solar Physics, 12, 1

Webb, D. F. & Howard, T. A. 2012, Living Reviews in Solar Physics, 9, 1

Whitman, K., Egeland, R., Richardson, I. G., et al. 2023, Advances in Space Research, 72, 5161, cOSPAR Space Weather Roadmap 2022: Scientific Research and Applications

Wild, J. & McCready, L. 1950, Australian Journal of Chemistry, 3, 387

Wild, J., Smerd, S., & Weiss, A. 1963, Annual Review of Astronomy and Astrophysics, 1, 291

Wills-Davey, M., DeForest, C., & Stenflo, J. O. 2007, The Astrophysical Journal, 664, 556

Wilson, J. W., Townsend, L. W., Chun, S. Y., et al. 1988, BRYNTRN: A baryon transport computer code, computation procedures and data base, Tech. rep.

Wöllmer, M., Zhang, Z., Weninger, F., Schuller, B., & Rigoll, G. 2013, in 2013 IEEE International Conference on Acoustics, Speech and Signal Processing, IEEE, 6822–6826

Wood, B., Howard, R., & Socker, D. 2010, The Astrophysical Journal, 715, 1524

Wu, C.-C. & Lepping, R. P. 2016, Solar Physics, 291, 265

Wuelser, J.-P., Lemen, J. R., Tarbell, T. D., et al. 2004, in Society of Photo-Optical Instrumentation Engineers (SPIE) Conference Series, Vol. 5171, Telescopes and Instrumentation for Solar Astrophysics, ed. S. Fineschi & M. A. Gummin, 111–122

Xapsos, M. A., Stauffer, C. A., Jordan, T. M., Adams, J. H., & Dietrich, W. F. 2012, IEEE Transactions on Nuclear Science, 59, 1054

Xie, H., Ofman, L., & Lawrence, G. 2004, Journal of Geophysical Research: Space Physics, 109

Young, P. R., Tian, H., Peter, H., et al. 2018, Space Science Reviews, 214, 1

Zank, G., Matthaeus, W., Bieber, J., & Moraal, H. 1998, Journal of Geophysical Research: Space Physics, 103, 2085

Zhang, J., Cheng, X., & Ding, M.-d. 2012, Nature communications, 3, 747

Zhang, J. & Dere, K. P. 2006, apj, 649, 1100

Zhang, J., Richardson, I., Webb, D., et al. 2007, Journal of Geophysical Research: Space Physics, 112

Zhang, P., Wang, C. B., & Ye, L. 2018, Astronomy & Astrophysics, 618, A165

Zhang, P., Zucca, P., Kozarev, K., et al. 2022a, The Astrophysical Journal, 932, 17

Zhang, W., Zhao, X., Feng, X., et al. 2022b, Universe, 8, 30

Zhu, H., Zhu, W., & He, M. 2022, Solar Physics, 297, 157